ADAPTIVE AND ORBITAL ELEMENT METHODS FOR CONJUNCTION ANALYSIS

A Dissertation

by

CHRISTOPHER TODD SHELTON

Submitted to the Office of Graduate and Professional Studies of
Texas A&M University
in partial fulfillment of the requirements for the degree of

DOCTOR OF PHILOSOPHY

Chair of Committee,	John Junkins
Committee Members,	Raktim Bhattacharya
	Manoranjan Majji
	Shankar Bhattacharyya
Head of Department,	Rodney Bowersox

May 2020

Major Subject: Aerospace Engineering

ABSTRACT

Collisions between Earth orbiting satellites and debris have been a topic of growing concern among satellite operators and governments for many years. At the heart of preventing collisions, which have been observed to have terrible consequences for the health of the space environment, is the timely identification of potential collisions and the accurate quantification of the probability of collision. This work will introduce novel methods for uncertainty propagation that take into account the collision geometry and adaptively respond to nonlinearity measures taken along the eigenvectors of the satellite state distributions in order to ensure proper conjunction algorithm selection and enhance computational efficiency. Local linear probability density function approximations are demonstrated to be appropriate for a wide class of collision scenarios and provide immense computational advantages over traditional conjunction analysis.

Next, the effects of coordinate choice are explored. New formulations of the collision risk measure in spherical coordinates and orbital elements are derived and shown to provide increased accuracy over traditional conjunction analysis methods in Cartesian coordinates. These new formulations are made possible through the novel use of relative orbital elements, which are also instrumental in providing new insights into methods for identifying potential collisions and collision windows.

Finally, new avenues for collision probability are explored through investigation of the steady state behavior of the collision risk measure. This analysis gives insight into the steady state distributions of orbiting objects and is used to develop upper bounds for the probability of collision between two satellites. These developments are then brought together in a single software tool called CRATER and compared against other contemporary approaches for conjunction analysis on a number of test cases.

DEDICATION

This dissertation is dedicated to my wonderful wife Katie, who has supported me from beginning

to end, to my son Russell, who thinks his dad commutes to space everyday to work on satellites,

and to my dear daughter Sarah Rose, who runs to hug me as I walk in the door.

ACKNOWLEDGMENTS

CONTRIBUTORS AND FUNDING SOURCES

TABLE OF CONTENTS

LIST OF FIGURES

LIST OF TABLES

1. INTRODUCTION AND LITERATURE REVIEW *

1.1 The Space Environment

The launch of the very first satellite Sputnik on October 4th 1957 marked the beginning of a new era in world history, the space age. This great achievement of the Soviet Union sparked the fears and imaginations of Americans everywhere. Soon the public mind was a buzz and consumed in the great space race. While Sputnik reentered the Earth's atmosphere after about three months, it would soon be replaced by a myriad of other artificial satellites, payloads, rocket boosters, and other mission related debris. Since the launch of Sputnik, the number of debris objects in orbit has been greater than the number of operational satellites [1]. In these early days of both peaceful and strategic space exploration it would have been hard to imagine the number of man made objects that would be launched into orbit and how dependent the common person, and indeed, global commerce would become on satellites and other space based capabilities.

The number of objects in orbit has been increasing steadily since 1957. These objects are typically lumped into two categories. Identified objects are those which are of known origin and purpose (usually), while unidentified objects cannot be traced back to their genesis. Identified objects typically originate from either payloads or rockets. For identified objects the European Space Agency (ESA) has created the following taxonomy [1].

- Payloads, space object designed to perform a specific function in space excluding launch functionality. This includes operational satellites as well as calibration objects.

- Payload mission related objects, space objects released as space debris which served a purpose for the functioning of a payload. Common examples include covers for optical instruments or astronaut tools.

- Payload fragmentation debris, space objects fragmented or unintentionally released from a

---

*Parts of this chapter are reprinted with permission from "ESA ' s Annual Space Environment Report," Tech. Rep. GEN-DB-LOG-00271-OPS-SD, European Space Operations Centre, Robert-Bosch-Strasse 5, D-64293 Darmstadt, Germany, 2019. Revision 3.2, by ESA

payload as space debris for which their genesis can be traced back to a unique event. This class includes objects created when a payload explodes or when it collides with another object.

- Payload debris, space objects fragmented or unintentionally released from a payload as space debris for which the genesis is unclear but orbital or physical properties enable a correlation with a source.

- Rocket body, space object designed to perform launch related functionality; this includes the various orbital stages of launch vehicles, but not payloads which release smaller payloads themselves.

- Rocket mission related objects, space objects intentionally released as space debris which served a purpose for the function of a rocket body. Common examples include shrouds and engines.

- Rocket fragmentation debris, space objects fragmented or unintentionally released from a rocket body as space debris for which their genesis can be traced back to a unique event. This class includes objects created when a launch vehicle explodes.

- Rocket debris, space objects fragmented or unintentionally released from a rocket body as space debris for which the genesis is unclear but orbital or physical properties enable a correlation with a source.

This list makes it obvious that there are intentional and unintentional means of generating debris in space. The distribution of these objects in space is not uniform, but varies by region and evolves over time. The space environment is typically broken into regions based on altitude, inclination, and orbit eccentricity. There are many ways to subdivide space; The vast majority of our space assets and debris reside in either Low Earth Orbits (LEO) or Geostationary Orbits (GEO). LEO orbits are those with a maximum orbital altitude of less than $2000km$, while GEO orbits are those found between altitudes of $35,586km$ and $35,986km$ and inclinations of less than

$15°$. These regions of space are so important that they have been designated as protected under international agreement [2] and are shown in Figure 1.1.
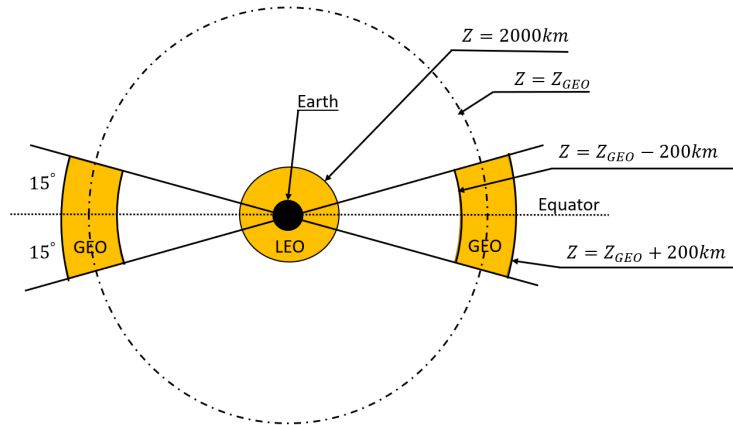
Figure 1.1: Inter-Agency Space Debris Coordination Committee Protected Orbital Regions.

The protection status of these regions is an agreement by space faring nations to respect the unique nature and importance of these two regions when planning and conducting space operations, to protect them from debris, and to ensure their safe and sustainable use in the future. The "safe and sustainable use", statement is a reference to the threat that debris poses to the health of the space environment. The risks of operating in space are several fold, but one of the risk factors comes from possible collisions with other objects. While these events are rare, the likelihood of a collision increases with the number of resident space objects (RSO). The consequences of a collision event far exceed the loss of one or two space assets. The collision itself generates a large amount of new debris, which can increase the likelihood of subsequent collisions. This can be seen by looking at the number of observable objects in Earth orbit over time shown in Figure 1.2 taken from ESA's 2019 annual space environment report [1].

The growth in the number of objects is fairly linear (increasing by about 200 objects per year) except for two notable jumps in the years 2007 and 2009. The first of these jumps is the result of the intentional break up of the Fengyun 1c satellite which was destroyed in an anti-satellite
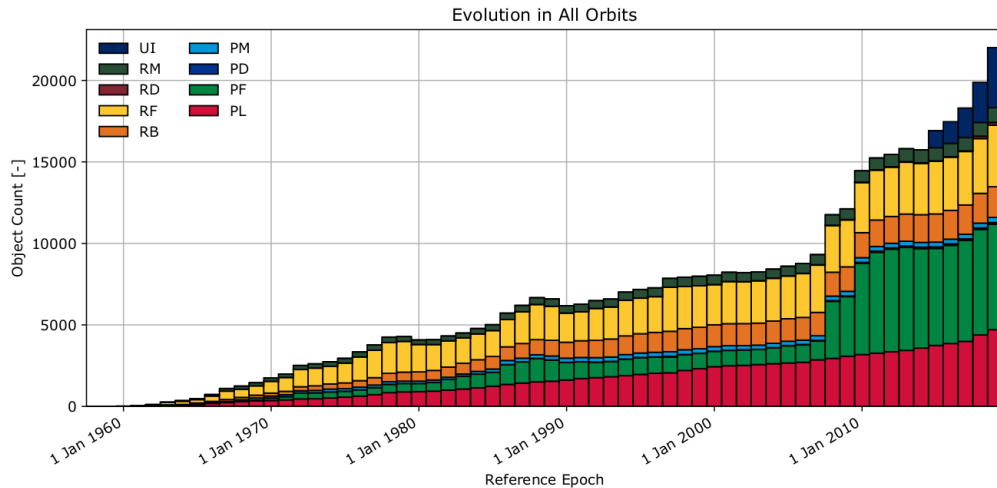
Figure 1.2: Number of Observable Objects by Type in Earth Orbit Through Time. Reprinted with permission from [1].

missile test. The sudden increase of debris from this event challenged existing methods for tasking sensors and updating the space catalogue. The jump in 2009 was the result of an unintentional collision between the Iridium 33 and Kosmos 2251 satellites. Both of these events occurred in the LEO orbital region and had a large impact on the number of objects in this region as shown in Figure 1.3 taken from ESA's 2019 space environment report [1]. LEO is by far the most populated orbital region around Earth and is particularly vulnerable to violent collisions because of the wide variation in satellite inclinations and right ascensions used at LEO altitudes.

Collisions do not just increase the number of objects in orbit, but also their distribution. Due to slight variations in orbital parameters between debris objects, each will have slightly different orbital periods and precession rates. This causes the debris to spread out, primarily along the right ascension of the ascending node and the orientation of the perigee vector, sweeping over a shell of different orbits over time. This was seen in studies following both the Fengyun incident and the Iridium Kosmos collision [3, 4]. This phenomenon, caused primarily by Earths non-spherical gravity field, amplifies the impact of the collision upon the surrounding space environment making future collisions in the shell swept out by the debris more likely. This effect was first studied by Donald Kessler in 1978 [5]. He showed that under the right conditions, just like neutrons in a
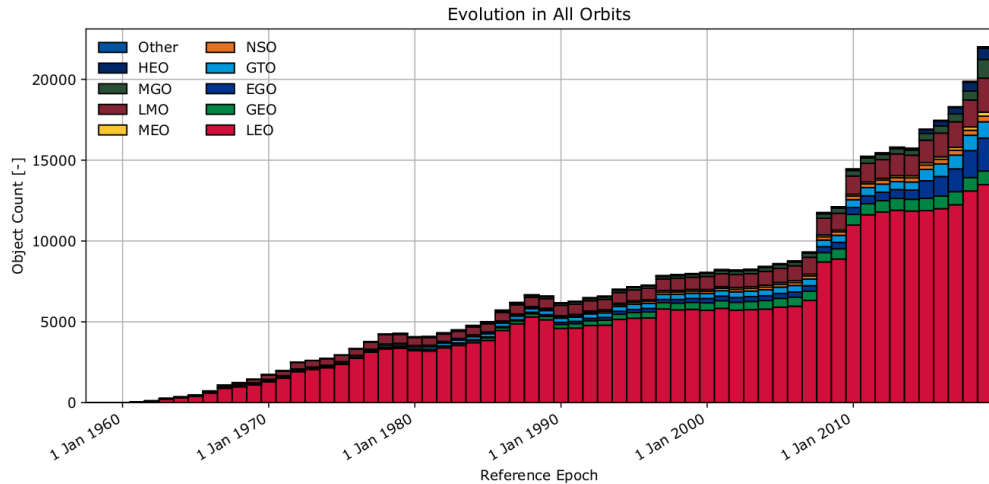
Figure 1.3: Number of Observable Objects by Orbital Regime Through Time. Reprinted with permission from [1].

nuclear fission reaction, debris produced from a single collision event could cause a chain reaction of additional collisions, conceivably rendering the space environment unusable for future missions.

The health of the space environment is largely a function of how responsible we are in its use. This fact has been recognized by all major space faring nations and led to the formation of the Inter-Agency Space Debris Coordination Committee in the early nineties and has also been a regular topic for the United Nations' Committee on the Peaceful Uses of Outer Space since 1994. These international bodies have been key in the drafting and adoption agreements on liability due to debris and debris mitigation standards [1].

Mitigation is one of the best courses of action for preventing future satellite collisions. However, despite all efforts to reduce irresponsible behavior, the space environment will likely continue to become more crowded. In the absence of future large collisions of the 2007 and 2009 class, the current orbit debris does not impose an immediate threat that inhibits most space operations. However, looking forward, with the evident long term secular growth of catalogued objects, the problem is and will become increasingly concerning. This dissertation is aimed at developing improved tools to analyze this important class of problem. The current situation is evident when examining the accelerated growth in the number of objects in orbit over the last five years in Figures 1.2 and

5

1.3. During this time frame, the growth rate in number of objects is seen to accelerate steeply. This trend is largely due to the advent of modern commercial utilization, constellations, and small satellites. These revolutions in the industry have opened the doorway to cheaper space missions and mega constellations [6, 7, 8]. As utilization increases it is anticipated that passive mitigation practices will not be enough to ensure the sustainable use of the space environment. This has led to a large number of works studying active mitigation techniques such as debris removal [9, 10, 11, 12] and collisions avoidance [13, 14].

It is clear that collisions have adverse and lasting effects on the space environment and that these effects will only be exacerbated by increased utilization. Passive mitigation practices are a necessary component of a healthy space environment, but are not sufficient on their own to prevent future collisions. Collision avoidance, when necessary, is only effective if collisions can be predicted ahead of time with some acceptable level of certainty and at least one of the space craft is maneuverable. These constraints on predicting collisions are the driving forces behind conjunction analysis, which will be discussed in greater detail in Section 1.5.

1.2 Space Situational Awareness

Since the beginning of the space age, there has been a need to update an maintain a catalogue of Earth orbiting objects. This was done early on as a matter of practicality to keep track of space assets as well as a matter of public safety, since, as seen by radar, a satellite reentering the atmosphere can closely resemble a missile attack. Early efforts to maintain the space catalogue were headed by the National Space Surveillance Control Center and have since been taken up by multiple national and international entities including NASA, NORAD, USSTRATCOM, USAFSPC, NSC, ESA and other international partnering space agencies. A history detailing the evolution from satellite tracking to SSA and the various agencies involved can be found in [15].

The space catalog today is the culmination of a massive international effort to identify, track and update satellite orbits. These orbits and their uncertainty are updated using various models until new observations are available [16, 17]. Even stillm, there is widespread concern about the accuracy of orbit uncertainty in the catalogue. The effort to maintain a complete and accurate

catalogue is further complicated by the presence of uncorrelated tracks, or observations that do not correlate to a cataloged orbit [18]. As seen in the previous section, current technology has allowed the catalog to grow to a size of over $20,000$ objects 10 cm in size or larger [1]. It is important to remember that these only represent the observable and cataloged objects. It is estimated that there are many more objects than are currently visible [19] and the number of cataloged objects is expected to increase by nearly a factor of 10 within then next year as a result of new, higher precision, radar observation sites being built as part of the United States space fence [20, 21]. This increase in the number of cataloged objects is expected to strain current collision analysis efforts. Processing this larger volume of tracking data will require additional investment in computing resources or the development of more efficient conjunction algorithms.

Modern SSA goes beyond catalog maintenance. While the exact definition and scope of SSA changes from country to country, at its heart it embodies the idea of knowing the time varying population of objects in the space environment, the risks, and being able to dynamically respond. Catalog maintenance is an important subcategory of this effort and is often associated with other space surveillance and tracking efforts. Once satellites are cataloged, they can be checked against other cataloged objects for possible conjunctions. The screening horizon is typically 7 days for a LEO object and 10 days for GEO orbits. In the United states collision screening is typically handled by the Combined Space Operations Center (CSpOC formerly JSpOC). Operators will provide data to an intermediate agency such as NASA's conjunction assessment and risk analysis (CARA) group who will send the ephemeris to CSpOC to be screened against other objects for close approaches in a higher accuracy catalog that is not available to the public. CARA will then analyze possible close approaches to determine the probability of collision and then issue a conjunction report to the operator [22]. This analysis can be done on a per maneuver basis for high interest assets. Accurate quantification of the collision risk is an important part of this process, that can be thwarted by untimely analysis, unknown maneuvers, or inaccurate results. This highlights the importance of conjunction analysis as part of an overall SSA strategy.

1.3 The Collision Problem

As discussed earlier, collision avoidance is an active measure taken to protect space assets, the space environment, and is a realization of SSA by allowing satellites to actively respond to threats. These discussions addressed the underlying motivation for considering the collision problem in the first place. This problem was seen to have several constituent parts that begin with measurement and orbit determination, then maintaining and updating the space catalogue, identifying potential collision candidates from the catalogue, locating these collisions in time and space, and then finally, quantifying the risk of collision for these satellite pairs through accurate computation of the probability of collision (P_c). The work of this dissertation will give focus to the last three parts of this problem with heavy emphasis on computing P_c.

This decidedly probabilistic approach to satellite collision avoidance is contrasted by other more deterministic approaches to collision avoidance employed in other applications such as ellipsoidal threat volumes or keep out zones. This probabilistic strategy is used primarily in response to the strong desire not to maneuver the satellites more than necessary for collision avoidance purposes.

The satellite probability of collision problem, as it has been treated in the literature, is as follows. Two satellites S_1 and S_2 are considered with known initial state uncertainty distributions. At some future time, we consider the case that these satellites will experience a close approach (see Figure 1.4). The question then is what is the P_c between S_1 and S_2 during this close approach.

To address this problem, we will break it down into two parts: The *propagation stage* will deal with the problem of taking the initial probability density function and propagating it through the nonlinear equations of motion so that it will be available for use when it comes time to compute the P_c. The next part will be the actual *computation of P_c* during the collision event. To define the collision event, we begin by defining a closed level set on the initial distribution, for each satellite, such that only negligible probability mass exists outside of each of the level sets. For an initial Gaussian distribution this level set might be the 6σ ellipsoid. The collision event begins when
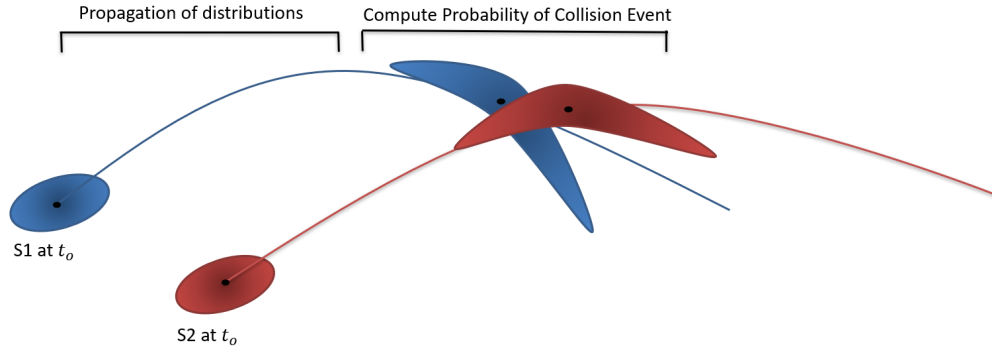
Figure 1.4: Computing the Probability of Collision.

these level sets first begin to intersect and ends when they have completely passed through each other. Both parts of this problem have already received extensive attention. To better understand the context and significance of the developments in later chapters, the next two sections will discuss the bodies of literature that address uncertainty propagation in orbital mechanics and computation of the probability of collision.

1.4 Uncertainty Propagation

The first part of the problem deals with uncertainty propagation in a nonlinear system. The uncertainty in the collision problem is a direct result of our inability to perfectly observe the position and velocity vectors of a given satellite or debris object. Some objects, such as low earth orbiting (LEO) satellites equipped with global positioning systems (GPS), will have much smaller state uncertainty compared to other objects such passive debris and especially objects with a high area to mass ratio [23, 24, 25]. This initial uncertainty is usually reported in terms of its first two statistical moments (mean and covariance), leading to the widely used approximation that the initial uncertainty in the satellites' states will be distributed according to a Gaussian probability density function (PDF).

In addition to initial state uncertainty, there is also likely uncertainty in the dynamics of the system. This type of uncertainty is typically classified as either parametric or unstructured. In a spring mass damper system, parametric uncertainty might manifest itself as uncertainty in the

spring constant and damping constant of the system, while the unstructured uncertainty is typically modelled as a random stochastic process that imparts random accelerations to the mass at any given time. In the orbital mechanics, satellite drag parameters are the most significant source of model uncertainty for LEO satellites, because of the large uncertainties in atmospheric density at these orbital altitudes as well as attitude dependent drag parameters [26, 27, 28]. This uncertainty can be modelled as either parametric or unstructured or as a combination of the two. The choice of how to model uncertainty has a significant effect on the problem in that it determines the appropriate governing equations.

The time evolution of the PDF of an object state in a system with both parametric and unstructured uncertainty is governed by the Fokker-Planck equation also known as the Kolmogorov forward equation [29, 30]. When propagating uncertainty using this governing equation, the state and parametric uncertainty serve as an initial condition while unstructured uncertainty is a source term driving a diffusion process. In many large physical systems, such as orbiting satellites, it is often permissible to consider only structured model uncertainty for some applications. When only structured uncertainty is considered, the generalized Fokker Planck Kolmogorov (FPK) equation reduces to the Liouville equation [31] which then describes the time evolution of the PDF. The Liouville equation is simply a statement on the conservation of mass, stating that probability mass is constant along a given trajectory. This is an important principle since it allows states to be mapped onto the PDF at t_0 to evaluate their probability density.

Whether the FPK equation is used, or the Liouville equation depends on the presence of a stochastic forcing term. In general either equation is difficult to solve exactly, particularly as the dimension of the system under consideration increases. In the collision problem, the dimension of the state space is at least 12 and can be higher when uncertain force model parameters are appended to the state vector. In response to this so called curse of dimensionality, a number of different techniques have been developed to find approximate solutions [32]. The accuracy of some of these approximate solutions can be unacceptably low while others can approach the exact solution to within an arbitrary degree.

One of the first and mostly widely used techniques is linear uncertainty propagation. This approximate technique is computationally attractive in that it only requires integration of the gradient of the system dynamics along a nominal trajectory to obtain what is known as the state transition matrix (STM) [33]. Implicitly this approach requires that the dynamics be differentiable, as is the cases with the classical dynamical models for orbital mechanics. The computational efficiency was an especially important factor in early spaceflight because computers were still in the early stages of development. Perhaps the most important factor influencing the popularity of this technique was the advent of the Kalman and Bucy linear filter [34, 35]. While these filters were derived for linear systems, they were quickly extended to nonlinear systems through local linearization of departure motion about the current best estimate of the trajectory, and adopted by the National Aeronautics and Space Administration (NASA) to tackle spacecraft estimation problems [36, 37]. The practical consequences of these techniques proved to be revolutionary and played an important role in the guidance, navigation, and control algorithms for the Apollo missions [38, 39]. Linear covariance techniques are still widely used today [40, 41] and are considered the industry standard for on-board uncertainty propagation and estimation.

Despite its overwhelming popularity, linear uncertainty propagation does have one major failing. The resulting approximation errors are unsuitable for long propagation arcs in nonlinear systems. For linear dynamical systems the STM is a globally valid model for state dispersion and can be used to obtain an analytical solution to the corresponding Liouville equation. In nonlinear systems however, the STM is only locally valid. The domain of validity is tied strongly to the nonlinearity of the mapping, which has led researchers to quantify nonlinear and non Gaussian developments in the state mappings and PDF respectively for nonlinear systems [42, 43]. One important insight gained from investigating the linearity of mappings was to discover the importance of coordinate choice when propagating uncertainty.

For a given nonlinear dynamical system, an infinity of coordinate choices are possible. The nonlinearty of the differential equations are highly dependent on the coordinates chosen. Some coordinate systems produce highly nonlinear mappings such that the equations of motion, as derived

in that system have high variability both temporally and spatially, while other coordinate choices can exhibit large domains of quasi linear behavior. Thoughtful choice of coordinates can dramatically enlarge the domain over which the departure dynamics are approximately linear as shown in [44, 45, 46, 47].

This idea of local linearity is an important concept when using linear uncertainty propagation in nonlinear systems. If one knows the location of the posterior mean one can use local linearization to improve the accuracy of linear covariance mappings as will be demonstrated in Chapter 3. Even when the best linearization point is not known, it can be estimated iteratively until it converges as is done in the iterated Kalman Filter [48].

There are many instances however, when linear uncertainty propagation will simply be inadequate to describe a propagated PDF, regardless of coordinate choice or reference trajectory. If the dynamics are differentiable, this challenge can sometimes be remedied by the use of higher order state transition tensors (STT). The STM represents a first order Taylor series approximation of a dynamic system. Obviously for a linear system this is sufficient, but in nonlinear systems one can consider the higher order terms of the series to capture the nonlinear behavior of the system. This approach can be used to obtain a better approximation of the solution of the Liouville equation as demonstrated in [49, 50] and has been used to improve accuracy in the related estimation problem [51]. The STT approach is more computationally expensive than the STM approach but, can used to obtain high fidelity solutions to many uncertainty propagation problems. One drawback is its reliance on higher order analytical derivatives, which in many cases are tedious and time consuming to derive, program, and compute. Similar results can be obtained with out needing to compute the analytical derivatives by using differential algebra techniques[52]. The differential algebra techniques automate the derivation and coding of the higher order derivatives and, while computationally expensive, it greatly reduces the derivation and programming effort. This provides a numerical implementation of the STT and has been used in both orbital mechanics uncertainty propagation [53] and for analyzing close approaches [54].

In problems where one does not wish to compute the analytical derivatives associated with

STT's, or in cases where the dynamics are not differentiable, uncertainty can still be propagated using moment matching techniques. These approaches minimize the number of sample trajectories that must be propagated from the initial PDF and require a much less extensive analytical and programming effort. They have been popularized into the mainstream of orbital mechanics research through the development of the the unscented Kalman Filter (UKF) and related developments [55, 56, 57]. The central idea behind this technique is to map the moments of the PDF using a discreet set of points chosen from the state space (called sigma point) such that they satisfy expectation integrals with respect to the PDF up to some order. For the unscented transform, these satisfy expectation integrals up to third order, and have been recently extended to satisfy up to eighth order constraints [58]. Unscented transforms provide an excellent way to map the mean and covariance of a PDF in nonlinear systems and has even been used, to limited extent, to improve P_c estimates in the collision probability problem [59].

The final set of relevant uncertainty propagation techniques that will be discussed here involve projecting uncertainty onto a set of either orthogonal functions or radial basis functions. Here, the propagated PDF is projected onto the basis functions such that the weighted sum of the functions satisfies the governing stochastic partial differential equation. In terms of orthogonal basis functions, the concept was introduced by Norbert Wiener [60] who used Hermite polynomials which are orthogonal with respect to the normal distribution. Wiener or Polynomial chaos expansions are used for uncertainty propagation in many fields [61, 62] and have been applied recently to orbit uncertainty propagation with some limited applications to the collision problem [63, 64]. Polynomial expansions can be carried out, in principle, to any order to satisfy the governing stochastic differential equations, but become computationally expensive in higher dimensions. Projection onto radial basis functions is usually done using a Gaussian mixture model (GMM). The GMM represents a given PDF as a weighted sum of Gaussian PDFs and has long been popular in the machine learning and pattern recognition communities [65, 66].

Radial basis functions using local Gaussians is widely used in input/ output approximation and has been given various names such as *support vector machines* [67, 68, 69]. This approach has been

demonstrated to be particularly important for uncertainty propagation in orbital mechanics [70], since it allows one to exploit all of the properties of local Gaussian distributions while being able to model non-Gaussian PDFs to high fidelity. Its use is straight-forward, if not too computationally expensive for the particular application.

Uncertainty propagation using GMMs begins by resolving the initial Gaussian distribution into mixture components with a unique mean, covariance and importance weighting. Each of these components are then in turn propagated, using any appropriate technique from above, to obtain the propagated means and covariances of the mixture components. These are then used to form weighted normal distributions whose sum gives a high fidelity approximation of the PDF. One problem is in knowing how many mixture components will be necessary to model the PDF. This has been solved by developing entropy-based splitting techniques to adaptively resolve mixture components into sub-components [71]. This technique has been used to great success in a number of P_c algorithms [72, 73, 74].

For a more comprehensive discussion of these techniques and their application to the broader range of topics within orbital mechanics please see [75]. One noticeable omission from this discussion of uncertainty propagation techniques is the Monte Carlo (MC). This frequently applied technique is covered in Chapter 2.

One important concept concerning uncertainty propagation is that it is not independent of the end use of the PDF. In other words, it is important to remember that the uncertainty, in the problem under consideration, is being propagated so that it may be used to compute the P_c at some future time. In general the computation of P_c requires numerical integration over $12+$ dimensions. Numerical integration can be reduced down to just 2 dimensions if certain approximation assumptions hold and the right uncertainty propagation techniques are used. In particular, due to the many desirable analytical properties of normal distributions, propagation techniques that make use of Gaussians or sums of Gaussians can lead to a significant reduction in the complexity of the P_c integral. That is why they are at the base of the foremost P_c algorithms in use today.

One concept that has been overlooked in uncertainty propagation for collision analysis is the

14

importance of local PDF approximations. Collisions are an inherently local event and under the right conditions are amenable to local linear approximations. The importance of considering the collision geometry and its coupling with coordinate choice and local approximation techniques will be demonstrated in the coming chapters along with the significant effect this can have on algorithm performance.

1.5 Probability of Collision Computation

This section presents the current literature on computing probability of collision (P_c) in a topical format. For a more chronological discussion please see the introduction section in Chapter 3. As with the discussion on uncertainty propagation, P_c computations involving Monte Carlo techniques will be reserved for Chapter 2. This section considers mainly semi-analytical methods for computing P_c. Within this subset of methods are two predominant paradigms underlying the computation of P_c. These are the *short encounter paradigm* and the *long encounter paradigm*.

The short encounter family of P_c solutions began in 1992 with the work of James Foster [76]. Remember from our previous discussion that this was around the time that space debris was beginning to receive serious attention from members of the international space community. In any case, this family of solutions is characterized by its emphasis on making approximations centered on the time of closest approach (T_{CA}). The time of close approach was an important concept in early conjunction analysis and was used to determine close approach miss distances [77]. The time of close approach and the associated miss distance continue to be important quantities today and are often used for collision prefiltering [78, 79, 80, 81, 82, 63, 54, 83]. The time of closest approach for a distribution, however, is not deterministic, so short encounter methods compute this quantity for the means of the two satellite distributions under consideration. At T_{CA} a plane is defined whose normal $(\boldsymbol{n})$ is the relative velocity vector between the two mean or nominal trajectories such that $\boldsymbol{n} = (\bar{\boldsymbol{v}}_1 - \bar{\boldsymbol{v}}_2)$. Short encounter methods make the assumption that the duration of this close approach is so short that rectilinear relative motion along $\boldsymbol{n}$ can be assumed. In other words, the direction of $\boldsymbol{n}$ remains constant for times near T_{CA}. This means that the distributions approach each other along the constant relative velocity vector and can therefore be projected onto the plane

with normal n. This process is visualized in Figure 1.5.
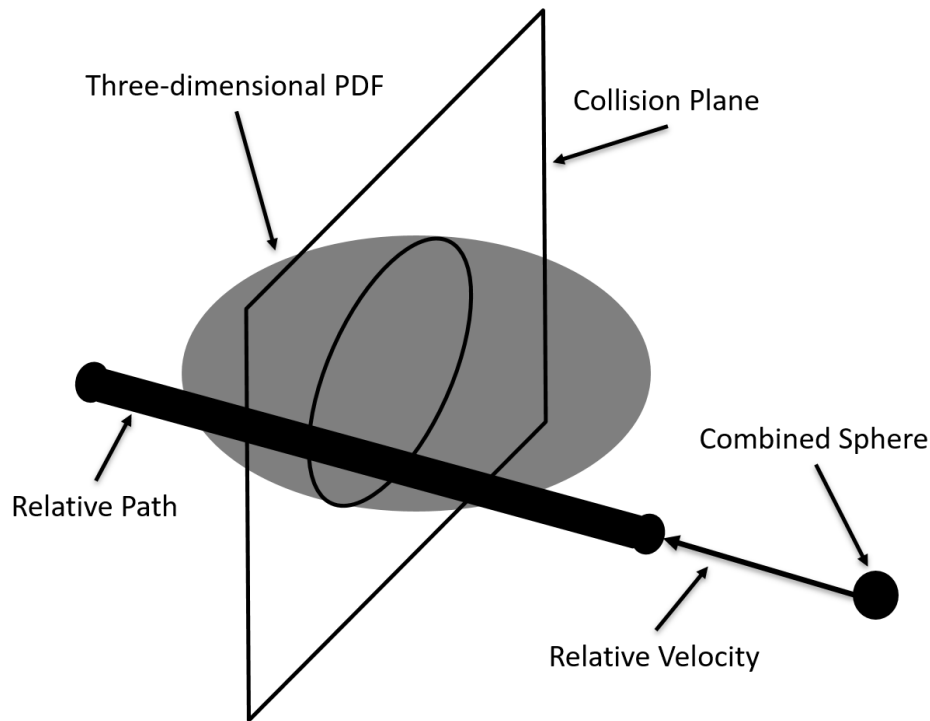
Figure 1.5: Short Encounter Projection onto the Collision Plane.

To facilitate computation, the PDFs that are projected onto the collision plane are often assumed to be Gaussian in Cartesian space. Furthermore, the colliding satellites are usually assumed to be spheres, such that if they come within a certain distance of each other, called the radius of collisions (R_c), the satellites are said to be colliding. Under these assumptions, the P_c integral reduces to a two dimensional integral over the PDF of the relative distance projected onto the plane of collision. Slight variations in the approach and effort to establish the best method for computing this integral on the plane of collision have led to numerous works which make up the short encounter subset of the probability of collision literature [76, 84, 85, 86, 87, 88, 89, 90].

In order to amend some of the errors introduced into the P_c computations by these methods, several researchers have looked into ways to account for nonlinear motion [91, 92, 89], non-spherical space craft [93, 94], and non-Gaussian distributions [95]. These additions help extend

short term collision analysis to a wider array of collision scenarios.

The next subset of literature for computing P_c follows the *long term encounter paradigm* and are all derivatives or extensions of [96]. Following this much more general viewpoint, the evolution of the PDF during the collision event is significant and must be accounted for. The effects of the true nonlinear motion of the system also become significant on these time scales and are included in the formulation. Formulating the P_c integral in this fashion addresses many of the difficulties and approximation errors created by the rectilinear motion assumptions used in the derivation of the short encounter formulation. The long encounter method for computing P_c is derived by considering the probability mass flux into the sphere defined by R_c. Thus, unlike the short encounter method, no planar projection takes place, so one must evaluate the P_c integral over a sphere. This results in a more complex formulation of the P_c integral that is not as readily computed as the short encounter formulations.

In general, the P_c integral in this technique would require numerical integration over all 12 dimensions of the joint PDF. This was addressed in the original derivation by making the assumption that again the PDFs in Cartesian space are Gaussian. Under this assumption the P_c integral reduces to 4 dimensions, an analytical integral over relative velocities entering the sphere of collision, integrating these densities over the surface of the sphere and then integrating over all times for which a collision may occur. Inherent in this formulation is the assumption that probability mass only enters the sphere once, which may be problematic if the satellites undergo oscillatory motion with respect to one another or have multiple close approaches in the same window of analysis. To extend the method to allow for non-Gaussian behavior the basic formulation has been cast in terms of Gaussian mixture models, which have been used to great success to achieve both accurate and computationally attractive results [72, 74, 97, 73, 98].

1.6 Scope and Contributions

The scope of the present work is to build upon and contribute to the existing 28+ years of literature on conjunction analysis in novel and meaningful ways. This requires developing new algorithms that go beyond the current state of the art, as well as making new theoretical contri-

butions that expand our understanding of collisions in space. I propose to achieve this goal by accomplishing the following major tasks.

1. Identify and exploit quasi linear sub-spaces in algebraic and differential equation mappings of the probability density function associated with the orbital state uncertainty to improve algorithm performance

2. Take into account collision geometry and demonstrate its importance

3. Use the eigenvectors of the distribution in orbital element space to build efficient PDF approximations in Cartesian space

4. Allow for parametric model uncertainty

5. Use the Liouville equation to quantify the error in approximations

6. Combine these techniques and insights into single software tool

7. Explore the consequences of coordinate choice

8. Explore collisions in the orbital element space

9. Develop new formulations for computing the probability of collision that can be evaluated in orbital element space

10. Explore the validity, accuracy, and computational merit of the algorithms and compare to the best available pre-existing approaches

In the course of pursuing these first ten goals certain pleasant surprises and new insights of broader significance resulted, these will be discussed broadly and in the context of the above ten tasks.

2. VALIDATION

2.1 Introduction

Accurately and efficiently quantifying the probability of collision P_c between orbiting objects is a problem of fundamental and great practical interest to the space situational awareness community. Methods for addressing this problem fall primarily into two categories: Monte Carlo (MC) methods [99, 100, 101, 102], and semi-analytical methods [76, 88, 87, 84, 85, 96]. In general semi-analytical techniques are orders of magnitude faster than a Monte Carlo analysis when computing the P_c on a given problem. However, these semi-analytical methods often rely heavily on linearizing assumptions and local Gaussian distributions. Several newer approaches and algorithms have used adaptive algorithm selection and tuning of Gaussian mixture methods to minimize dependence on these assumptions, but still often require Gaussian initial conditions or that the propagated PDF be Gaussian in orbital element space [72, 74, 98, 103]. For many collision scenarios these assumptions are justified, but it can be hard to quantify the error induced by these assumptions in the P_c estimate without additional MC analysis.

While Monte Carlo is often vilified for its slow convergence, its ease of implementation, physical model independence, and lack of assumptions cannot be denied as important and distinguishing strengths. As such, nearly every study ever conducted on the probability of collision between satellites, the current work included, uses Monte Carlo simulations to validate or check solutions computed by more efficient semi analytical methods. This allows researchers to compare their methods against a pseudo model which is mathematically guaranteed to approach the truth as the number of Monte Carlo samples becomes sufficiently large. What qualifies as sufficiently large is dependent on the probability of the event being analyzed and the desired confidence in the computed solution. As such, one never computes an exact solution using a Monte Carlo method, but one that is within $\pm\epsilon$, $(\epsilon > 0)$ of the reported value with a confidence of $(1 - \alpha)$, $\alpha \in [0, 1]$. However, the number of samples needed to achieve a given ϵ, α is an area still being researched

and has led to the development of several methods for bounding the number of samples required [104, 105, 106]. The uncertainty in the computed MC result can make it extremely difficult to validate semi-analytical results beyond one or possibly two significant figures using Monte Carlo techniques. However, this may be instructive too in that the pursuit of more accuracy than this is often of little pragmatic value, since engineers and algorithms usually only need the exponent and the first one or two digits of a probability to make an informed decision. Additionally, since the Monte Carlo is a discrete method, it can sometimes prove difficult to use exactly the same definition of a collision event as the semi analytical method does. This issue can be significant when one wants to isolate errors due to assumptions made in defining the collision event from other errors such as local Gaussian assumptions.

Monte Carlo analysis is easily performed using parallel computation and can benefit from modern CPU and GPU architectures. There are numerous studies quantifying this benefit [107, 108, 100]. In the satellite P_c problem, there is another benefit that can be achieved using the modified Chebyshev Picard iteration orbit propagation (MCPI) technique [109, 110, 111, 112, 113, 114]. MCPI works by projecting an initial estimate of the trajectory onto a set of orthogonal Chebyshev polynomials [115, 116] and then iteratively integrating and updating this trajectory through Picard fixed point iteration [117]. The Picard iteration technique allows all local force model evaluations to be done simultaneously on each iteration, allowing for highly efficient implementation in parallel algorithms (this is part of an ongoing study being conducted by Ahmed Ismail and John Junkins). The MCPI method has been shown to offer tremendous computational advantages (over one order of magnitude) when propagating a single trajectory [118]. This speed advantage is amplified in the Monte Carlo setting where neighboring sample trajectories will be able to benefit from a hot start of the Picard iterations.

A hot start is where the solution path of one trajectory is used as the initial estimate for a neighboring trajectory. Since sample trajectories of the Monte Carlo are all sampled from the same initial distribution, they tend to form a bundle of separate yet similar trajectories. Hence, the orthogonal polynomial fit of the mean trajectory typically provide a good initial guess for other

sample trajectories in the distribution. This speeds up the overall Monte Carlo since a good initial guess when using MCPI decreases the number of Picard iterations until the solution converges.

Another benefit of the MCPI solution for the satellite collision problem is in locating the point of closest approach. Typically for Monte Carlo methods, trajectories from both initial distributions are propagated and then compared to find which trajectory pairs result in a collision. The collision event being defined for satellites coming within a certain distance of each other, usually called the radius of collision R_c. Typical numerical integrators return discrete states along the trajectory at either uniform or non uniform time intervals. If the time interval between states returned from the integrator is long, then it is likely that a close approach between two trajectories happened sometime between reported states and times. This results in an interpolation problem to find if there was a time when two trajectories were within R_c of each other since often $R_c << 1km$. To get around this difficulty many researchers and practitioners fit a cubic or quartic polynomial to the two trajectories in the window of the collision event and then use a root finding method to locate the time of closest approach. This is simplified when using the MCPI integrator since what is returned from the integrator is not just the states at discrete times, but the coefficients of the continuous orthogonal polynomial fit of the state space trajectories, so a highly precise trajectory interpolation is built into the MCPI solution. This permits rapid, machine precision root solving for T_{CA}.

Theoretically, the exact solution to the P_c problem can be obtained if the probability density function (PDF), from which the P_c is computed, satisfies the governing Fokker Planck equation. For the work at hand, we consider a system that is not acted upon by a random forcing function. In the absence of such a noise term, the Fokker Planck equation reduces to the Liouville equation; which governs the evolution of the PDF in time. While an exact solution to the Liouville equation is readily obtainable in terms of the initial distribution, it is often desirable to have an expression that does not require back propagating states through the dynamical differential equations or computation of high order state transition tensors. This is done by projecting the logarithm of the solution to the Liouville equation onto a set of orthogonal polynomials. This rigorous approxima-

tion of the PDF is then used to compute P_c. Computing the P_c in this manner carries with it the computational burden of needing to perform numerical integration in a high number of dimensions and will likely take as long or longer than the Monte Carlo. However, computing a nearly exact P_c, for the given assumptions, allows for different advantages compared to the Monte Carlo. It will be easier, for instance to use the same definition of the collision event as other semi analytical techniques, therefore we will be able to separate error due to the collision definition from errors due to Gaussian assumptions.

2.2 Methods

2.2.1 Monte Carlo using MCPI

Let us consider satellites S_1, S_2 with initial distributions $N_1(\bar{q}_1, Q_1)$ and $N_2(\bar{q}_2, Q_2)$ where N is the normal distribution. Suppose that m samples are drawn from each distribution. To perform our Monte Carlo analysis we will propagate these $2m$ samples forward in time and then determine the number of pairs n that result in a collision. Note that from $2m$ samples we are able to generate m^2 pairs. It is important to note that $m^2 - m$ of these pairs are not strictly independent. However, given the efficiency of generating trajectory pairs this way many authors use this all on all pairing for their conjunction Monte Carlo analysis. Once the n colliding pairs have been identified the probability of collision is simply $P_c = \frac{n}{m^2}$. The major computational considerations for this problem are propagating the $2m$ trajectories and finding the subset of n trajectory pairs that result in a collision from m^2 candidates. Let us now consider how MCPI can enhance the efficiency of these two steps.

To see why MCPI is particularly well suited to Monte Carlo analysis it is helpful to recall how the method works. The following discussion will briefly discuss the derivation of MCPI on a first order system and assumes the reader is familiar with the Chebyshev polynomials. Relevant properties of the Chebyshev polynomials can be found in Appendix A. A more in depth discussion of the derivation and current enhancements of the MCPI method can be found in [113, 118]

2.2.2 MCPI Polynomial Fitting

Consider the first order differential equation $\dot{X} = f(t, X(t))$, $X(t_0) = x_0$. In general $a < t \leq b$ is not the interval $[-1, 1]$. This is taken care of by the following change of variables. $t = w_1 + w_2 \tau$ where $w_1 = (b+a)/2$, $w_2 = (b-a)/2$ and $-1 < \tau \leq 1$.

Now

$$\frac{dx}{dt} = \frac{dx}{d\tau}\frac{d\tau}{dt} \implies \frac{dx}{d\tau} = \frac{dx}{dt}\frac{dt}{d\tau} \tag{2.1}$$

hence

$$\dot{X} = w_2 f\big(t(\tau), X(t(\tau))\big), \quad X(t(-1)) = x_0 \tag{2.2}$$

or

$$\dot{X} = g\big(\tau, X(\tau)\big), \quad X(-1) = x_0 \tag{2.3}$$

Now in terms of Chebyshev polynomials

$$g(\tau, X(\tau)) = \sum_{k=0}^{N-1} \alpha_k T_k(\tau) \tag{2.4}$$

If τ is taken at the Chebyshev nodes $\tau_k = \cos\left(\frac{k\pi}{M}\right)$, $k = 0, 1, \ldots, M$, we can later exploit the discrete orthogonality property

$$g(\tau_k, X(\tau_k)) = \sum_{i=0}^{N-1} \alpha_i T_i(\tau_k), \tau \in \mathbb{R}^{M+1} \tag{2.5}$$

Or more conveniently in vector matrix notation

$$\underline{g} = \Phi\underline{\alpha} \tag{2.6}$$

where the vectors $\underline{g}, \underline{\alpha}$, and matrix $[\Phi]$ have the following form.

$$
\begin{bmatrix} g_0 \\ g_1 \\ g_2 \\ \vdots \\ g_M \end{bmatrix} = \begin{bmatrix} T_0(\tau_0) & T_1(\tau_0) & T_2(\tau_0) & \dots & T_{N-1}(\tau_0) \\ T_0(\tau_1) & T_1(\tau_1) & T_2(\tau_1) & \dots & T_{N-1}(\tau_1) \\ \dots\dots\dots\dots\dots\dots\dots\dots\dots\dots\dots\dots\dots\dots \\ T_0(\tau_M) & T_1(\tau_M) & T_2(\tau_M) & \dots & T_{N-1}(\tau_M) \end{bmatrix} \begin{bmatrix} \alpha_0 \\ \alpha_1 \\ \alpha_2 \\ \vdots \\ \alpha_{N-1} \end{bmatrix} \tag{2.7}
$$

Using a least squares curve-fitting mentality, it behooves us at this time to find the coefficients α such that we obtain a least squares fit. If the residuals of the fit are given by $\underline{r} = \underline{g} - \Phi\underline{\alpha}$, then the α that minimizes $\|\underline{r}\|_2$ is given by:

$$
\min_{\forall \alpha \in \Re} J = \frac{1}{2}\underline{r}^T\underline{r} \tag{2.8a}
$$

$$
0 = \frac{d}{d\alpha}\left[\frac{1}{2}(\underline{g} - \Phi\underline{\alpha})^T(\underline{g} - \Phi\underline{\alpha})\right] \tag{2.8b}
$$

$$
0 = \frac{d}{d\alpha}\left(\frac{1}{2}\underline{g}^T\underline{g} - \underline{g}^T\Phi\alpha + \frac{1}{2}\underline{\alpha}^T\Phi^T\Phi\underline{\alpha}\right) \tag{2.8c}
$$

$$
0 = 0 - \Phi^T\underline{g} + \Phi^T\Phi\underline{\alpha} \tag{2.8d}
$$

$$
\underline{\alpha} = (\Phi^T\Phi)^{-1}\Phi^T\underline{g} \tag{2.8e}
$$

For non-orthogonal basis functions, the matrix $\Phi^T\Phi$ quickly becomes ill-conditioned as the order of T_n increases, making the matrix difficult to invert. If τ is taken at the Chebyshev nodes however, and a weighting matrix W is introduced such that $\Phi^T W \Phi$ is a diagonal matrix due to discrete orthogonality, then the inverse is simply the inverse of the diagonal elements. For $\tau_k = cos(\frac{\pi k}{M}), k = 0, 1, \dots, M$ W is simply $\text{diag}([\frac{1}{2}, 1, 1, \dots, 1, 1, \frac{1}{2}])$. See [109] for more detail. With W the least squares fit is now given by the following.

$$
J = \frac{1}{2}(\underline{g} - \Phi\underline{\alpha})^T W(\underline{g} - \Phi\underline{\alpha}) \tag{2.9}
$$

where

$$\underline{\alpha} = (\Phi^T W \Phi)^{-1} \Phi^T W \underline{g} \tag{2.10}$$

Since $(\Phi^T W \Phi)$ is diagonal with the diagonal elements

$$(\Phi^T W \Phi)_{ii} = m_{ii} = \sum_{j=0}^{M} W_{jj} T_i^2(\tau_j) \tag{2.11}$$

, the coefficients are computed independently from the inner products.

$$\alpha_i = \frac{1}{m_{ii}} \sum_{j=0}^{M} W_{jj} T_i(\tau_j) g_j \tag{2.12}$$

2.2.3 MCPI Integration Via Picard Iteration

Now that we have obtained a least squares approximation of $g(\tau, X(\tau))$ in terms of the Chebyshev polynomials for the case that $M = N - 1$. Hence, $\dot{X} = g(\tau, X(\tau)) = \sum_{k=0}^{N-1} \alpha_k T_k(\tau) = \underline{\alpha}^T T(\tau)$, $X(-1) = x_0$ Where $\underline{\alpha}$ was found in the previous section. We will now integrate this expression to obtain the solution to the differential equation $\dot{X} = g(\tau, X(\tau))$.

$$
\begin{aligned}
X(\tau) - X(-1) &= \int_{-1}^{\tau} g(s, X(s)) ds \\
\implies X(\tau) &= x_0 + \int_{-1}^{\tau} g(s, X(s)) ds
\end{aligned}
\tag{2.13}
$$

Since we are solving for X, the expression on the right cannot be evaluated analytically. Given an initial guess for $X(\tau)$ the solution can be found via Picard Iteration (2.14).

$$X^i(\tau) = x_0 + \int_{-1}^{\tau} g(s, X^{i-1}(s)) ds \tag{2.14}$$

Plugging in our approximation for $g(\tau, X(\tau))$

$$X(\tau) = x_0 + \int_{-1}^{\tau} \underline{\alpha}^T T(s) ds X(\tau) = x_0 + \underline{\alpha}^T \int_{-1}^{\tau} T(s) ds \tag{2.15}$$

Recall the recursive integration relationship $\int T_n \, dx = \frac{1}{2}\left(\frac{T_{n+1}}{n+1} - \frac{T_{n-1}}{n-1}\right)$ plugging this in to the expression above we obtain

$$X(\tau) = x_0 + \frac{\underline{\alpha}^T}{2} \begin{bmatrix} 2T_1(\tau) \\ \frac{T_2(\tau)+T_0(\tau)}{2} \\ \frac{T_3(\tau)}{3} - \frac{T_1(\tau)}{1} \\ \frac{T_4(\tau)}{4} - \frac{T_2(\tau)}{2} \\ \vdots \\ \frac{T_N(\tau)}{N} - \frac{T_{N-2}(\tau)}{N-2} \end{bmatrix} - \frac{\underline{\alpha}^T}{2} \begin{bmatrix} 2T_1(-1) \\ \frac{T_2(-1)+T_0(-1)}{2} \\ \frac{T_3(-1)}{3} - \frac{T_1(-1)}{1} \\ \frac{T_4(-1)}{4} - \frac{T_2(-1)}{2} \\ \vdots \\ \frac{T_N(-1)}{N} - \frac{T_{N-2}(-1)}{N-2} \end{bmatrix} \tag{2.16}$$

Now suppose that $X(\tau)$ is also approximated using a Chebyshev series and note that the 3rd term on the right is just a column of constants.

$$X(\tau) = \underline{\beta}^t \begin{bmatrix} T_0(\tau) \\ T_1(\tau) \\ T_2(\tau) \\ \vdots \\ T_N(\tau) \end{bmatrix} = x_0 + \frac{\underline{\alpha}^T}{2} \begin{bmatrix} 2T_1(\tau)) \\ \frac{T_2(\tau)+T_0(\tau)}{2} \\ \frac{T_3(\tau)}{3} - \frac{T_1(\tau)}{1} \\ \frac{T_4(\tau)}{4} - \frac{T_2(\tau)}{2} \\ \vdots \\ \frac{T_N(\tau)}{N} - \frac{T_{N-2}(\tau)}{N-2} \end{bmatrix} - \frac{\underline{\alpha}^T}{2} \begin{bmatrix} C_0 \\ C_1 \\ C_2 \\ C_3 \\ \vdots \\ C_{N-1} \end{bmatrix} \tag{2.17}$$

By equating like orders of T_n we find the equations for the coefficients β in terms of α

$$\beta_0 = x_0 + \frac{\alpha_1}{4} - \frac{\underline{\alpha}^T}{2}\underline{C} \tag{2.18a}$$

$$\beta_1 = \frac{2\alpha_0}{2} - \frac{\alpha_2}{2} \tag{2.18b}$$

26

$$\beta_n = \frac{\alpha_{n-1}}{2(n-1)} - \frac{\alpha_{n+1}}{2(n+1)} \tag{2.18c}$$

$$\beta_{N-1} = \frac{\alpha_{N-2}}{2(N-2)} \tag{2.18d}$$

$$\beta_N = \frac{\alpha_{N-1}}{2(N-1)} \tag{2.18e}$$

Note that α appears linearly in the equations for β, thus β is conveniently written in matrix form $\underline{\beta} = x_0 + [S]\underline{\alpha}$. $[S]$ is given in [118], but can be easily derived and is presented in Appendix A. Expanding the expression for α we see...

$$\underline{\beta} = \begin{bmatrix} x_0 \\ 0_1 \\ \vdots \\ 0_N \end{bmatrix} + [S](\Phi^T W \Phi)^{-1} \Phi^T W \underline{g} \tag{2.19}$$

Recall that $X(\tau) = \underline{\beta}^T \underline{T}(\tau)$. If we discretize the domain $\tau = \tau_k$, $k = 0, 1, 2, 3, \ldots, M$, the expression becomes $X(\tau_k) = \underline{\beta}^T \underline{T}(\tau_k)$, or in vector matrix notation.

$$\begin{bmatrix} X(\tau_0) \\ X(\tau_1) \\ X(\tau_2) \\ \vdots \\ X(\tau_N) \end{bmatrix} = \begin{bmatrix} T_0(\tau_0) & T_1(\tau_0) & T_2(\tau_0) & \ldots & T_N(\tau_0) \\ T_0(\tau_1) & T_1(\tau_1) & T_2(\tau_1) & \ldots & T_N(\tau_1) \\ \cdots\cdots\cdots\cdots\cdots\cdots\cdots\cdots\cdots\cdots\cdots \\ T_0(\tau_M) & T_1(\tau_M) & T_2(\tau_M) & \ldots & T_N(\tau_M) \end{bmatrix} \begin{bmatrix} \beta_0 \\ \beta_1 \\ \beta_2 \\ \vdots \\ \beta_N \end{bmatrix} \tag{2.20}$$

Note that the matrix of Chebyshev polynomials used here is not the same dimensions as Φ. The difference will be noted by calling this matrix Ψ. By expanding the expression the final form of the MCPI integrator is obtained for the case where $M > N$.

$$\underline{X}^i = [\Psi] \begin{bmatrix} x_0 \\ 0_1 \\ \vdots \\ 0_N \end{bmatrix} + [\Psi][S][(\Phi^T W \Phi)^{-1} \Phi^T W] g(\underline{\tau}, \underline{X}^{i-1}) \tag{2.21}$$

For convenience we rewrite the expression as

$$\underline{X}^i = [\Psi][\Theta_{x_0}] + [\Psi][C_\alpha] g(\underline{\tau}, \underline{X}^{i-1}) \tag{2.22}$$

Where all bracketed terms are constant and can be pre-computed beforehand. This expression is iterated until a desired tolerance is reached. If a hot start is employed the number of iterations untill convergence is reduced.

2.2.4 MCPI and Monte Carlo for Conjunction Analysis

Suppose now that we have used the MCPI method propagate the mean of the initial distribution for S_1 to get $\bar{\boldsymbol{q}}_1(\tau_k)$. It is now desired to propagate a sample trajectory from the distribution of S_1 with initial conditions $\boldsymbol{q}_j(0)$. To get an initial guess for $\boldsymbol{q}_j(\tau_k)$ it is written in terms of the mean trajectory as.

$$\boldsymbol{q}_j(\tau_k) = \bar{\boldsymbol{q}}_1(\tau_k) + \Delta\boldsymbol{q}_j(\tau_k), \quad k = 0, 1, 2, \ldots, M \tag{2.23}$$

If $\boldsymbol{q}$ is in orbital elements then

$$\Delta\boldsymbol{q}_j(\tau_k) \approx \Delta\boldsymbol{q}_j(\tau_0) \tag{2.24}$$

will provide a good estimate of the trajectory to use in equation (2.22) for all but the time varying anomaly variable. For the last element we look at the partial of the true anomaly with respect to the initial semi-major axis.

$$\frac{\partial f}{\partial a_0} = \frac{\partial f}{\partial E}\frac{\partial E}{\partial M_e}\frac{\partial M_e}{\partial a_0} = \frac{-3\sqrt{\frac{\mu}{a^5}}\Delta t_k}{4\left(\lambda^2 \sin^2\left(\frac{E}{2}\right) + \cos^2\left(\frac{E}{2}\right)\right)(1 - e\cos E)} \tag{2.25}$$

28

Where E is the eccentric anomaly, M_e is the mean anomaly, and λ is $\sqrt{\frac{1+e}{1-e}}$. If the dynamics are instead expressed in terms of modified equinoctial elements, then we note that $\frac{\partial L}{\partial a_0} \approx \frac{\partial f}{\partial a_0}$ since $L = f + \omega + \Omega$. This partial derivative need only be evaluated once for each τ_k and can then be used to update our initial estimate of the true anomaly for any sample trajectory $\boldsymbol{q}_j(\tau_k)$. Now that an initial estimate of the sample trajectory has been made it is iterated upon in equation (2.22) until it has converged.

MCPI is unique in this aspect. The solution of one trajectory can be used to as a hot start for a neighboring trajectory to speed up convergence. The effects of this hot start will be quantified on some sample Monte Carlos in the results section of this chapter. It is also important to note that these results extend to the case where the dynamics are being evaluated in Cartesian coordinates since the mean trajectory and initial condition of the sample trajectory can be mapped to the orbital elements space, where an estimate for the sample trajectory is made. The estimate for the sample trajectory can then be mapped back into Cartesian coordinates, if needed.

2.2.5 Monte Carlo Convergence

It is important whenever performing Monte Carlo analysis to ensure that the Monte Carlo has converged. The number of samples needed to achieve satisfactory convergence is a function of the probability P_e of the event, the confidence level α, and the confidence interval ϵ, and most importantly, the level of independence between subsequent samples.

There are many different ways to predict if a Monte Carlo has converged. Most commonly these are the *Chebyshev inequality*, the *Chernoff-Hoeffding bound* [104, 105], and more recently the *Dagum bound* [106]). Let us examine these bounds and see when they apply to our proposed Monte Carlo.

An experiment is designed in which a trajectory pair $\boldsymbol{p}_i = (\boldsymbol{q}_{1_i}(t), \boldsymbol{q}_{2_i}(t))$ is independently sampled from the joint probability density function $f_p(\boldsymbol{p}(t_0))$. We then consider the sum of random variable Z, which equals one when the selected trajectory pair results in a collision, and zero otherwise. Since we do not expect an equal number of zeros and ones we define the mean and

variance of Z as

$$\mu = E[Z] = \frac{1}{n} \sum_{i=1}^{n} Z_i \tag{2.26}$$

$$\sigma^2 = E[(Z - E[Z])^2)] = \frac{1}{n-1} \sum_{i=1}^{n} (Z_i - \mu)^2 \tag{2.27}$$

The Chebyshev inequality applied to the sum of Z gives.

$$\mathbb{P}\left(\left| \sum_{i=1}^{n} Z_i - \sum_{i=1}^{n} \mu_i \right| \geq n\epsilon \right) \leq \frac{Var\left(\sum_{i=1}^{n} Z_i \right)}{n^2 \epsilon^2} \tag{2.28}$$

When designing our experiment, it was stated that q_i were independently sampled. In practice, q_i are usually only pairwise independent as a result of the all on all pairing scheme discussed earlier. Even in the case of pairwise independence, the variance operator can be taken inside the summation and since all Z_i are identically distributed (i.e have the same mean and variance) the following is obtained.

$$\mathbb{P}\left(\left| \frac{\sum_{i=1}^{n} Z_i}{n} - \mu \right| \geq \epsilon \right) \leq \frac{\sigma^2}{n\epsilon^2} \tag{2.29}$$

Let the probability that our estimate of the mean is within $\pm\epsilon$ of the actual mean be called α. Then, the number of monte carlo samples needed then to ensure convergence within $\pm\epsilon$ of the true value with a confidence of $1 - \alpha$ is

$$n \leq \frac{\sigma^2}{\alpha\epsilon^2} \tag{2.30}$$

While known to be conservative, the classical Chebyshev bound is very fundamental and does not assume any prior knowledge of the distribution of the random variable. Since Z_i can only take values zero and one we can compute the variance of Z in terms of its mean using equation (2.27). This is useful since there is often an a priori estimate of the mean $\tilde{\mu}$ that we are trying to verify with the Monte Carlo.

$$\sigma^2 = \mu(1 - \mu) \tag{2.31}$$

Improvement over the Chebyhev bound can be achieved if Z_i are independent. For the summation of independent identically distributed (iid) random variables Chernoff used the Hoeffding

inequality to achieve the following.

$$\mathbb{P}\left(\left|\frac{\sum_{i=1}^{n} Z_i}{n} - \mu\right| \geq \epsilon\right) \leq e^{-nD(\mu+\epsilon||\mu)} \qquad (2.32)$$

Where $D(x||y) = x \ln \frac{x}{y} - (1-x) \ln \frac{1-x}{1-y}$. Even though it results in a looser bound, this result is often simplified by recognizing

$$D(\mu + \epsilon||\mu) \geq 2\epsilon^2 \qquad (2.33)$$

This results in the familiar expression.

$$n \leq \frac{1}{2\epsilon^2} \ln\left(\frac{2}{\alpha}\right) \qquad (2.34)$$

The Chernoff - Hoeffding bound represents a significant improvement over the Chebyshev bound for the case of independent Z_i. In a generalization of the zero-one estimator theorem [119, 120, 121], Dagum developed sophisticated sequential Monte Carlo algorithms designed to converge using a near minimum number of samples. These algorithms are based on a simple stopping rule, which has come to be called the Dagum bound in several papers [74, 89]. If $\epsilon\mu \leq \mu(1-\mu)$ the bound is written as

$$n \leq \frac{4(e-2)(1-\mu)}{\mu\epsilon^2} \ln\left(\frac{2}{\alpha}\right) \qquad (2.35)$$

This gives a near minimum number of samples needed to achieve a certain (ϵ, α) for our case where Z_i is limited to values of zero and one, but can overestimate the number of samples needed by a factor of $1/\epsilon$ in cases where $\sigma^2 << \mu$.

2.2.6 Exact Solutions

Another method for validating P_c results is to numerically compute the exact P_c using the PDF that satisfies the governing Fokker Planck Equation. Consider a general dynamical system with no

process noise:

$$\dot{\mathbf{x}}_t = \mathbf{f}(\mathbf{x}_t) \tag{2.36}$$

When the initial condition $\mathbf{x}_0$ are uncertain, modeled by the distribution $\mathbf{x}_0 \sim p(\mathbf{x}_0)$, the state $\mathbf{x}_t$ over time becomes uncertain. As a result, it is then required to compute the the evolution of the state probability density function (pdf) $p(\mathbf{x}_t)$. The exact solution to the evolution of the state pdf is governed by the Fokker Planck Kolmogorov equation (FPKE) or here just Liouville equation when there is no process noise:

$$\frac{\partial p(\mathbf{x}, t)}{\partial t} = -\sum_{i=1}^{n} \frac{\partial \left[f_i(\mathbf{x}) p(\mathbf{x}, t) \right]}{\partial \mathbf{x}_i} \tag{2.37}$$

Upon inspection the Liouville equation is simply a statement the conservation of probability mass along trajectories. Since this is the case, one can obtain a pointwise solution to the Liouville equation by mapping a state at some time t back onto the initial distribution as t_0. If the mapping of states forward in time is written as

$$\boldsymbol{x}(t) = g(\boldsymbol{x}(t_0); t, t_0) \tag{2.38}$$

then the probability density function at time t which satisfies the Lioville equation, can be written as

$$p(\boldsymbol{x}, t) = p\big(g^{-1}(\boldsymbol{x}(t); t_0, t), t_0\big) \left| \frac{\partial g^{-1}(\boldsymbol{x}(t); t_0, t)}{\partial \boldsymbol{x}(t)} \right| \tag{2.39}$$

As has been done before, the mapping $g(\boldsymbol{x}(t_0); t, t_0)$ will be expanded in terms of state transistion tensors (STT) [49, 51]. If the initial distribution was Gaussian this will naturally lead to a PDF of the form.

$$p(x, t) \approx e^{(c^T \phi(x))} \tag{2.40}$$

where c is a vector of coefficients and $\phi(x)$ is a vector of polynomials. The number of polynomials

is adjusted so that the approximation in equation (2.40) is sufficiently accurate over the domain of interest.

If we then consider the joint PDF of two objects, whose motion is independent of each other, and with distributions satisfying the Liouville equation at time $t \in [t_0, t_f]$, we obtain

$$p\big(x_a, x_b\big) = e^{\left(c^T \phi(x_a) + c^T \phi(x_b)\right)} \tag{2.41}$$

Given this distribution in x_a and x_b we should like to know the distribution of the random vector $x_r = x_b - x_a$. This is immediately obtainable by noting that $x_b = x_r + x_a$ and substituting into the previous expression.

$$p\big(x_a, x_r\big) = e^{\left(c^T \phi(x_a) + d^T \phi(x_a + x_r)\right)} \tag{2.42}$$

At this point we would like to define a collision in terms of x_r . The two objects shall be said to be colliding if the relative distance between them $r(t) \leq R_c$. In general, R_c is a function of the attitude of the two spacecraft. For the current discussion let us assume $R_c = $ constant. From a probability standpoint there are some difficulties with our definition of a collision. Since the time of collision is not deterministic, the condition $r(t) \leq R_c$ will generally be satisfied for a finite amount of time or even multiple times by the same two trajectories during the analysis window. To avoid this, we must either (1) define the collision in such a way such that we can assume that the collision criteria will only be satisfied at a unique time by each trajectory, or (2) we must account for the correlation in probability of collision along trajectories in time. Approach 1 is by far the predominant method for addressing this problem and has been implemented in either a 2D or 3D approach.

2D methods project the joint PDF onto a plane at a deterministic time of closest approach [76, 122, 87, 88, 85]. Recent 2D methods [103] evaluate the planar P_c as each cross section of the PDF passes through a plane of collision and then integrates over time.

The 3D method is accredited to Coppola [96]. He defines a set

$$\Lambda_\tau = \{(x_a, x_b) \in X(t) | r(t) = R_c \text{ and } (\boldsymbol{v} \cdot \hat{\boldsymbol{r}}) \leq 0\} \tag{2.43}$$

and then assumes that trajectory pairs only belong to the set for a unique $t = \tau \in (t_0, t_f]$. Obviously both the 2D and the 3D methods make assumptions that will not be justifiable over all collision scenarios. Despite their limitations however they are applicable to the majority of collisions that come under analysis. Approach 2 has not yet been implemented in a semi analytical technique, but is easily carried out using Monte Carlo techniques.

Whether approach 1 or 2 is taken, let Λ_r be the set of conditions on x_r that define a collision It is then clear that

$$P_c = \int_{x_a} \int_{\Lambda_r} p(x_a, x_r) d\Lambda_r dx_a \tag{2.44}$$

If no further assumptions are made the integral in equation (2.44) must be numerically evaluated over all twelve dimensions. This is done by taking quadrature points from the distribution of x_a and evaluating the inner integral in equation (2.44) at each quadrature point and then numerically evaluating the outer integral. Fortunately, these computations may be carried out in parallel. The locations of these quadrature points will be determined by the quadrature rule used as well as techniques developed in Chapters 3 and 4 for identifying the region of interest. Computing P_c in this fashion is believed to be more computationally burdensome than solving the problem via Monte Carlo, but gives an exact solution for P_c with respect to our definition of a collision.

2.3 Results

The first set of results is the comparison of the different Monte Carlo bounds. In Figures 2.1 and 2.2, the number of Monte Carlo runs needed to verify a given P_c within 5% with either a 99% or 95% confidence respectively are plotted using the Chebyshev bound, the Chernoff-Hoeffding bound using equation (2.32), the Dagum bound, and the relaxed Chernoff-Hoeffding bound from equation (2.34).

There is a common misconception in the conjunction analysis community that the Dagum
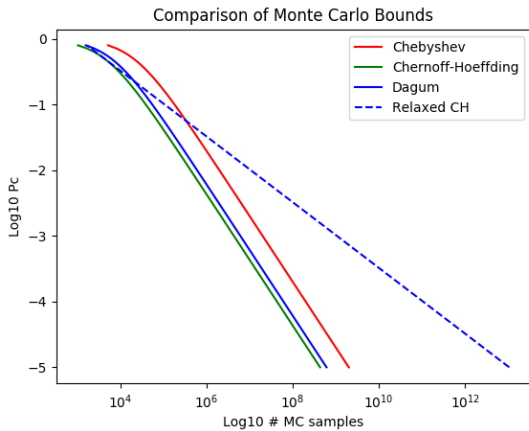
Figure 2.1: Comparison of Monte Carlo Bounds to Achieve a 5% Error with 99% Confidence.
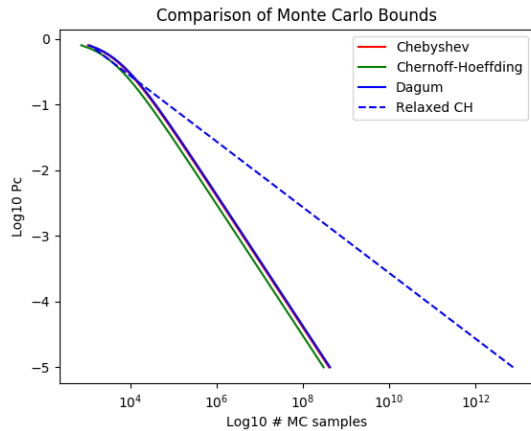
Figure 2.2: Comparison of Monte Carlo Bounds to Achieve a 5% Error with 95% Confidence.

bound is far superior to the Chernoff Hoeffding bound [74, 89]. This is an unfair comparison however since the Dagum bound is allowed to make use of a predicted mean and is often compared against the familiar relaxed version of the Chernoff Hoeffding bound. When information about the mean is provided to both the Chebyshev and Chernoff Hoeffding bounds, their performance is essentially the same as the Dagum bound to within a constant. Indeed, of the methods compared, it is clearly seen that the Chernoff Hoeffding bound provides the tightest estimate on the number of Monte Carlo runs needed. Apparently, while Chernoff and Hoeffding would not be surprised, this observation corrects a common miss-conception in the literature [74, 89].

The results in Table 2.1 show the benefits of using MCPI for the Monte Carlo. It is important to note that the version of MCPI used here is just the most basic version, without any enhancements and without taking advantage of parallel computing [113, 118]. Each ode solver in the table was used to propagate N trajectories using a $J2$ gravity model. From the table it is seen that MCPI results in about an order of magnitude speed up over ODE45 while an additional 20% time savings can be achieved in Monte Carlo settings through the use of a hot start. Another order of magnitude enhancement to the performance can be achieved using parallel architecture, since MCPI is inherently parallelizable, whereas traditional ode solvers such as ODE45 are not parallelizable along individual trajectories.

Table 2.1: Monte Carlo Propagation Times.

N	ODE45	MCPI	MCPI+HS
1000	41.5 s	4.7 s	3.9 s
5000	207.7 s	23.7 s	19.6 s
25000	1035.9 s	118.1 s	98.0 s

In Monte Carlo conjunction analysis it is also common to fit a low order polynomial to the time history of the miss distance between two trajectories. Cubic or quartic polynomials are usually used for this purpose, since the minimum miss distance can be found analytically. This approach can work but is prone to error. Since R_c is often on the order of 10 - 50 meters, errors in approximating the trajectory as a polynomial need to be much smaller than this. As the length of the encounter increases the order of the polynomial fit needs to increase as well. This type of error manifested itself when bench-marking the LG method from CRATER on the test cases from [89] and were discovered when the LG method appeared to be not even as good as the Foster method on these fairly linear test cases, a separate Monte Carlo was run to verify the results. Instead of using a cubic polynomial to detect collisions, the trajectory was propagated with a small enough time step such that the maximum relative velocity during the collision event multiplied into the the time step would produce a distance that was less than a radius of collision. The discrete set of points along each trajectory were then compared to see if the two closest points were within R_c of each other. Performing the Monte Carlo in this fashion agreed much better with the LG results as seen in Table 2.2. This approximation error introduced by the local cubic interpolation is not well understood or quantified in the current P_c literature, and hopefully this discussion will resolve the issue. The poorer performance of the LG method for cases 9 and 10 is indicative of the occasional difficulty experienced in accurately applying the LG approximation to near co-planar collisions.

When mapping the PDF forward in time or between coordinate systems it is important to recognize that nonlinearity is not homogeneous across all dimensions. This insight led to the important use of local Gaussians (LG) in Chapter 3. Figures 2.3 and 2.4 show 2D cross sections of the propagated PDF in orbital element space and corresponds to the PDF from CRATER test

Table 2.2: Discrete Monte Carlo Verification of Cubic Spline Method.

Test Case	Cubic MC P_c	Discrete MC P_c	LG P_c	Cubic Mc % Error	LG % Error
1	2.17E-01	2.58E-01	2.56E-01	15.85 %	0.98 %
2	1.57E-02 s	1.04E-02	1.14E-02	-51.41%	-9.78%
3	1.01E-01	1.33E-01	1.40E-01	24.01%	-5.80%
4	7.31E-02	3.23E-02	3.42E-02	-126.57%	-6.14%
5	4.45E-02	4.72E-02	4.65E-02	5.69%	1.45%
6	4.30E-03	4.57E-03	4.54E-03	5.87%	0.61%
7	1.61E-04	1.66E-04	1.64E-04	2.48%	0.88%
8	3.53E-02	4.76E-02	4.87E-02	25.91%	-2.32%
9	3.65E-01	3.70E-01	3.13E-01	1.19%	15.27%
10	3.63E-01	3.63E-01	3.13E-01	0.12%	13.84%
11	3.33E-03	4.31E-03	4.35E-03	22.85%	-0.90%
12	2.56E-03	3.76E-03	3.76E-03	32.03%	-0.04%

case 1. The cross sections are taken along the eigenvectors of the second moment of the PDF. The true PDF has been propagated via Monte Carlo, while the red concentric ellipses are the linear estimate of the PDF. The "eigenfiber", coined by Junkins in [98] has also been plotted in green and shows where local Gaussians (LG) would be placed to approximate this PDF. The error in the LG approximation is also shown as a heatmap.
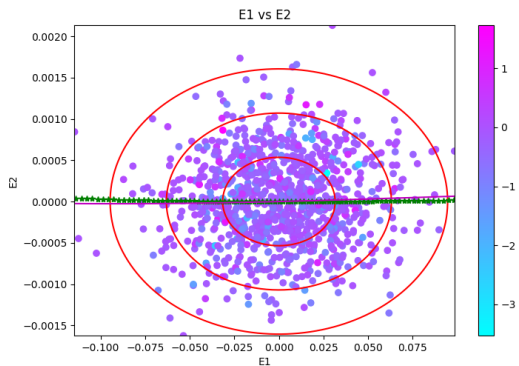
Figure 2.3: A 2D Subspace of the Propagated PDF with a Gaussian Cross Section.
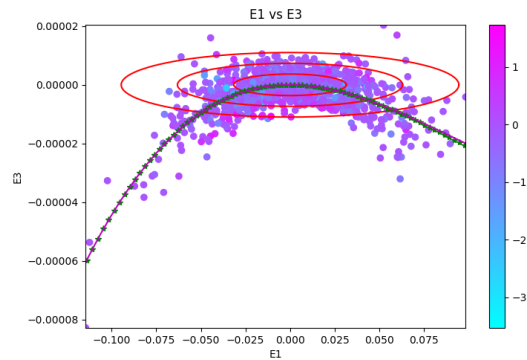
Figure 2.4: A 2D Subspace of the Propagated PDF with Significant Non-Gaussian Behavior Beyond 1σ.

The majority of 2D cross sections for the PDF resemble Figure 2.3 with only a few cross sections exhibiting non Gaussian behavior. This served as the motivation in CRATER to use GMM splitting only along the eigenfiber of the PDF as the other subspaces were still predominantly Gaussian. Even with a large Gaussian subspace there may be considerable error in the Local Gaussian approximation of the PDF. This level of error is acceptable for computing quanitities of interest where only the first one to two digits are required. This error however is not acceptable if we desire a much more accurate solution for diagnostic purposes. This error is driven down by including higher order terms from the approximation of the mapping as discussed in Section 2.2.6. The improvement in the PDF approximation is quantified in Figures 2.5 - 2.8. In these figures, the error in the PDF approximation is computed at 1000 discrete points, sampled from the initial Gaussian PDF. The exact solution to the Liouville equation was computed at each of the points giving an exact point-wise solution.
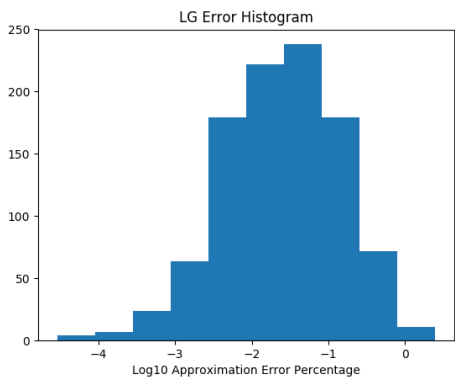
Figure 2.5: Histogram of LG PDF Approximation Error with Respect to Liouville Solution.
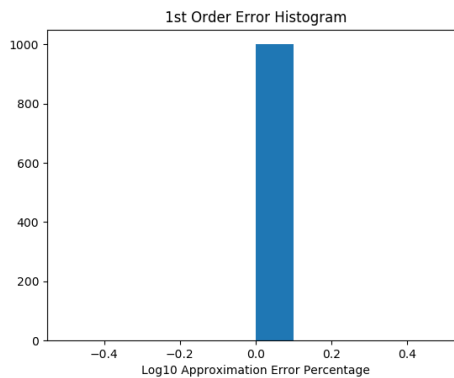
Figure 2.6: Histogram of 1st Order PDF Approximation Error with Respect to Liouville Solution.

For this case, the LG approximation is seen to be about 2 order of magnitude better than a linear approximation. More accurate approximations are obtained by using the 2nd and 3rd order STT. The third order STM (for this scenario) will be accurate enough to compute a nearly exact P_c. The exact P_c method for validating less accurate methods is demonstrated on CRATER test case
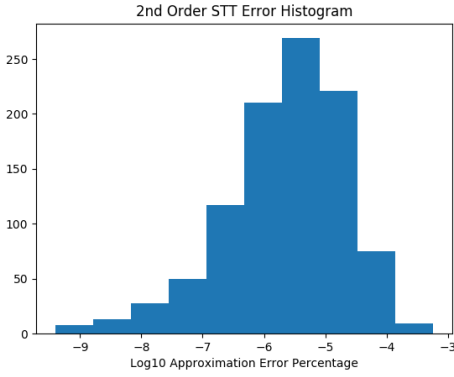
Figure 2.7: Histogram of 2nd Order PDF Approximation Error with Respect to Liouville Solution.
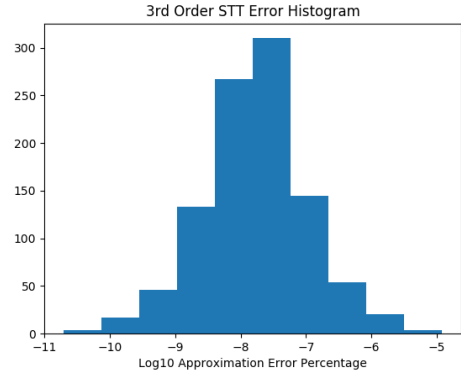
Figure 2.8: Histogram of 3rd Order PDF Approximation Error with Respect to Liouville Solution.

1. To reduce the dimensionality of the problem uncertainty was limited to the velocity space and the time of collision was fixed at the time of closest approach. Results are shown for six variants of this test case in Table 2.3 [123]. The error in the Monte Carlo is within the bound ϵ predicted by the Chernoff-Hoeffding bound for all cases.

Table 2.3: Liouville P_c vs Monte Carlo.

σ_v^2	r_c km	T_{CA}	PC_L	PC_{MC}	% Error	MC Size (Millions)
1E-7	0.1	0.25	5.85e-6	5.2e-6	6.4%	100
1E-7	0.1	0.75	2.34e-5	2.12e-5	6.3%	100
1E-7	0.1	1.25	9.36e-5	8.2e-5	4.5%	100
1E-4	10	0.25	5.85e-4	5.36e-4	3.9%	100
1E-4	10	0.75	9.36e-5	8.2e-5	1.0%	100
1E-4	10	1.25	5.85e-4	5.36e-4	8.6%	100

2.4   Conclusions

While Monte Carlo is an extremely important part of conjunction analysis, there is a significant variability in the level of understanding of the assumptions that go into producing the bounds within the P_c community. Some sub-spaces of the recent literature represent branches that are

not fully connected to the older developments. As a consequence we find that the Dagum bound, which promises near optimal performance, has gained in popularity despite offering no advantage over more established methods when a level playing field is used to test performance. Also of significance for all-on-all pairing, the Chebyshev bound is a more appropriate bound since it only requires pairwise independence.

The propagation portion of Monte Carlo conjunction analysis can consume a significant fraction of the overall computation time. The propagation can be significantly expedited by use of the recent enhancements to the MCPI ode solver. This method was shown to offer about an order of magnitude speed up over traditional integrators and an additional twenty percent speed up in Monte Carlo scenarios where use of the hot start is available and with even further speedup possible if massively parallel computation is used.

Linear and locally linear approximations of the PDF in orbital element space, while often accurate enough to compute P_c to one to two digits of accuracy, were shown not accurate enough to approach an exact solution. In this scenario Liouville methods are preferred to get the P_c. However, these methods come with the added computational expense of integration over all 12 dimensions of the joint PDF, which limit their practical usefulness outside the scope of validation studies for competing algorithms.

3.   THE CRATER ALGORITHM *

3.1   Introduction

This chapter details the development of a new collision risk assessment tool called CRATER. The CRATER algorithm was developed by the author and is a novel approach for conjunction assessment that makes use of new insights from collision geometry and from quantifying non-linearity in mappings to drive adaptive algorithm selection. New techniques, developed herein, for approximating probability density functions greatly enhance CRATER's computational performance over other contemporary approaches, while the exact Liouville solution is employed to quantify error in any approximations made during the uncertainty propagation phase. These features help to set CRATER apart from other approaches and build upon the current state of the art in conjunctions analysis.

There are many contributors to the current state of the art for calculating the probability of collision between satellites. One of the earliest treatments of the subject was by Foster [76] in 1992. This work was published around the time that space debris emerged as a major concern; with many countries and space agencies agreeing to a voluntary adoption of operational procedures to reduce the amount of debris their missions would produce. Foster's method assumed that the initial PDFs were Gaussian in Cartesian space and remained Gaussian for the remainder of the analysis window. Then, by assuming constant relative velocity and rectilinear motion during the collision event, the P_c integral was reduced to an analytical expression in two variables, valid for short term encounters. His work would influence later researchers such as Akella, Patera, Alfano, and Chan [84, 85, 87, 88, 89]. These early efforts were still heavily focused on short term encounters and many did not take into account full state uncertainty. Coppola, in his derivation of the P_c integral [96] arrived at an expression that allowed for velocity uncertainty and long term encounters. However, to reach his final result Coppola still assumed that the PDFs were Gaussian,

but noted that his methods could be extended via the Gaussian Mixture Model (GMM) to cases where the PDF was not Gaussian. This extension using a GMM was spelled out in an engineering note by DeMars K. et al. [72]. The works of Coppola and DeMars were added to recently by Joshua Horwood et al. [74] who advocated the use of orbital elements for the propagation phase and brought some additional insights into the construction of the GMM.

The CRATER Algorithm owes much to its predecessors, especially [96, 72, 74]. In order to be a general collision risk assessment tool, CRATER opted for an adaptive strategy, balancing fidelity and performance over an array of collision types. In collisions where nonlinear effects on the initial PDF (due to propagation) are negligible CRATER evaluates the P_c integral according to [96]. In cases of moderate non Gaussian behavior, where the relative inclination of the orbits is high, local Gaussians (defined later) are generated along the eigenfiber and the two nearest local Gaussians from each distribution at each time step are used to compute the P_c using Coppola's integral. In the context of this paper, eigenfiber will refer to the path generated in Cartesian space by displacements along the eigenvector of the covariance matrix in orbital element space with the largest eigenvalue. In the orbit problem, this invariably becomes the eigenvector that points predominantly along the direction of the time varying anomaly variable. This vector in orbital element space and its eigenvalue will serve as the basis for the approximation techniques presented later. Finally, if the distributions in Cartesian space are highly non Gaussian or the region of overlap of the two distributions is primarily in the direction of the eigenfiber, a GMM approximation of the PDF is formed in a manner similar to the one in [74] with the P_c evaluated according to [72], excluding mixture components that are further than 6σ from each other.

Another class of collisions are those with considerable model uncertainty. As of today, few studies have been done to consider the effects of model uncertainty on the probability of collision [124]. For LEO satellites, particularly debris objects with high surface area to mass ratios, significant model uncertainty may exist. Ignoring model uncertainty in these cases and using deterministic dynamics could result in erroneous and either overly optimistic P_c estimates or pessimistic estimates leading to excessive false alarms. CRATER focuses on an important subset of model un-

certainty in which the model uncertainty is strictly parametric. That is, only the parameters of the force model (with a known probability distribution function) are considered uncertain and capture all model error. This point of view can, for example, capture a "cannonball" drag model with an uncertain ballistic coefficient.

One of the primary problems facing all numerical simulations is knowing how well the computed result reflects reality. A necessary condition for a physically accurate solution is that the numerical simulation has computational fidelity with respect to the governing physics. CRATER seeks to address this problem by incorporating the Fokker Planck equation and using it as a truth model to measure the error caused by assumptions in the algorithm as well as to ensure that approximations of the PDF satisfy the Fokker Planck equation.

In the conjunction analysis and probability of collision problems, one is interested in identifying potential collisions and the probability of those collisions within some window of analysis (7 days in our case). The efforts detailed here focus on the second half of the problem. That is, determining the probability of collision for a given satellite pair (S1,S2). To determine the probability of collision, one must first know the nominal states for S1 and S2 at the initial time T_0 as well as the probability density function (PDF) for S1 and S2 at T_0. These inputs are the same as those required by other methods from the previously mentioned authors. The CRATER algorithm makes the assumption that the initial PDF is Gaussian in orbital element space [125]. In reality the initial PDF is likely not rigorously Gaussian in any coordinate frame (except, in some cases, the measurement frame); nevertheless, this assumption is made again here, as it has been in the previously cited works, to ensure the tractability of the required computations. While the theory remains the same for any set of non-singular element sets, the current version of CRATER is designed to work with the modified equinoctial orbital elements [126, 127]. Thus, the input mean and covariance are assumed to be in terms of normalized modified equinoctial orbital elements (MEEs).

Given the initial conditions, the algorithm propagates the mean and covariance of S1 and S2 using Linear Element Error Propagation (LEEP). This involves mapping the initial mean and covariance into a suitable set of non-singular orbital elements. The CRATER algorithm assumes that

this mapping has already occurred. The mean and covariance are then propagated using Gauss's variational form of the variation of parameters equations, formulated in modified equinoctial orbital elements, and the state transition matrix (STM). The STM can of course be augmented to account for parametric model uncertainty. Orbital elements are used to propagate the PDF, since a Gaussian distribution in orbital element space is able to capture, to a high degree of accuracy, the non-Gaussian behavior often observed in Cartesian space [128, 129].

Even in orbital element space, the Gaussian assumption will eventually break down. CRATER assumes that the PDF is adequately modeled by a single Gaussian in orbital element space, but computes and reports the error in this assumption relative to the solution of the Fokker Planck equation at discrete points, chosen along the eigenvectors of the distribution.

Since the probability of a collision is most easily measured in Cartesian space, it is required to map the propagated PDF from element space into Cartesian coordinates. This can result in a loss of covariance realism as described by Aristoff [130]. To maintain realism and aid computational efficiency, it is necessary to evaluate how non-Gaussian the PDF will be once mapped into Cartesian Coordinates. This is done by evaluating a non-linearity index, which evaluates how nonlinear the mapping is [42] at discrete points along the eigenfiber of the orbital element covariance ellipse that have been mapped into Cartesian space. If MEE are used for the uncertainty propagation in time, the primary source of non-linearity is typically the algebraic coordinate transformation of the propagated PDF back to Cartesian coordinates. If the non-linearity index is below a tolerance, the PDF is considered to be fully Gaussian in Cartesian coordinates over the region in which the tolerance is satisfied. If the non-linearity index is low, 20% -50% over $\pm 3\sigma$ then the PDF may be adequately approximated by a number of local Gaussians. Typically less than 100 local linearization points along the eignfiber, mapped into Cartesian coordinates, are sufficient to define a highly truncated but accurate PDF approximation over the collision region. However, for highly non-Gaussian PDFs, it may be preferable to use a Gaussian mixture when evaluating the probability of Collision (P_c) integral.

The P_c is then determined using Coppola's formulation of the integral [96], whose performance

has been verified by Hejduk [97] as well as by the previously cited studies [72, 74]. When re-deriving the P_c integral to account for parametric model uncertainty it was found that the addition of parametric model uncertainty did not affect the final formulation of the integral, but only enters in during the propagation of the covariance. This is a very attractive feature of incorporating the model uncertainty in this fashion. For a complete list of assumption please see Appendix D.

3.2 Methods

3.2.1 Uncertainty Propagation

From probability theory, we know that a function $g\colon X \to Y$ of a random variable $x \in X$, is also a random variable. The probability distribution $f_y(y)$ of a continuous, one-to-on map for the transformation $y = g(x)$ (often called a derived distribution) is commonly obtained by differentiating the cumulative distribution function $F_Y(y)$ with respect to y. This process is demonstrated in several texts including [131]. The distribution of $y = g(x)$ is then given by:

$$f_y(y) = f_x\big(g^{-1}(y)\big)|J^{-1}| \tag{3.1}$$

So long as g is one to one and invertible, where $J^{-1} = \frac{dg^{-1}(y)}{dy}$ is the Jacobian of the function g^{-1} evaluated at y. This relationship holds whether X and Y are scalars or vectors. In our case X is usually the state of the satellite at the initial time and Y is the state of the satellite at the final time. If X initially has a Gaussian distribution with mean μ and covariance matrix Σ then the distribution of X is given by

$$f_x(X) = \frac{1}{\sqrt{(2\pi)^n|\Sigma|}} \exp\left\{-0.5(X - \mu)^T\Sigma^{-1}(X - \mu)\right\} \tag{3.2}$$

We now wish to know the distribution of $Y = g(X)$. For the current discussion take g to be the nonlinear map of the state vector from the initial time t_0 to a given time t, Y to be the state at time t, and X to be the state at t_0. In general, the function g is not known globally in closed form, but can be evaluated pointwise by numerically solving the initial value problem. We can, however,

45

approximate g using a Taylor series expansion about the solution of the nominal trajectory. Doing this results in the following

$$Y = g(\mu + \Delta X, t, t_0) \approx g(\mu, t, t_0) + \nabla g(\mu, t, t_0)\Delta X + H.O.T \tag{3.3}$$

where $\Delta X = x(t_0) - \mu(t_0)$, $x(t)$ is a trajectory of interest, and $\mu(t)$ is the nominal trajectory

Subtracting over the first term and recognizing that if $g : X(t_0) \rightarrow X(t)$ then $\nabla g(\mu, t, t_0)$ is the state transition matrix Φ. We then rewrite the previous equation to first order as:

$$\Delta Y \equiv x(t) - \mu(t) = \Phi(\mu, t, t_0)\Delta X \tag{3.4}$$

For linear differential equations g is linear and equation 3.4 is exact for any input ΔX. Unfortunately, for systems governed by nonlinear differential equations, this relationship is approximate and will only be accurate within some finite neighborhood of μ. In the case of the two body equation, which governs the motion of the satellites in our collision problem (and is nonlinear whether formulated in Cartesian coordinates or orbital elements), prior work suggest that this neighborhood is not large enough (in Cartesian space) to capture the true nature of the PDF as it is propagated forward in time, since qualitatively, the state transition matrix will merely stretch and rotate the initial covariance ellipsoid, while the true distribution becomes, qualitatively, a skinny banana that wraps around the orbit. One way to solve the problem is to include the higher order terms in equation (3.3). Since g is a vector valued function, the nth order term will contain a nth order tensor of the mixed partial derivatives of g. Another approach, would be to introduce a change of variables to some regularized or slow variables, which make the dynamics more linear. That is to say, a change of variables which increase the domain over which the nonlinear equation (3.3) is well approximated by equation (3.4). One attractive set of such coordinates are the orbital elements.

The question then becomes, how long can the propagated PDF be accurately approximated as a Gaussian? This thinking has spurred the development of various metrics for answering this question and are explored in [42, 43, 128]. A more fundamental question may be, how well does

the approximation of the PDF satisfy the Fokker Planck equation? Recall that the Fokker Planck equation (or Kolmogorov forward equation [29]) is the partial differential equation governing the evolution of a PDF $p(x,t)$ where the time evolution of the state (x) is given by the stochastic differential equation

$$dx(t) = f(x(t), t)dt + G(x(t), t)dw(t) \tag{3.5}$$

In equation (3.5) $f(x(t), t)$ are the state dynamics acted on by a random forcing process $w(t)$ which is mapped onto the state space by the linear, time varying function $G(x(t), t)$ [49]. The Fokker Planck equation then is given by:

$$\frac{\partial p(x,t)}{\partial t} = -\sum_{i=1}^{n} \frac{\partial}{\partial x_i}\Big(p(x,t)f_i(x,t)\Big) + \sum_{i=1}^{n}\sum_{j=1}^{n} \frac{\partial^2}{\partial x_i \partial x_j}\Big(p(x,t)[GQG^T]_{ij}\Big) \tag{3.6}$$

CRATER assumes that all uncertainty associated with the process may be sufficiently modeled through parametric uncertainty. Therefore $Q = E[dwdw^T] = 0$. This reduces the Fokker Planck equation to the well known Liouville equation [132, 31].

$$\frac{\partial p(x,t)}{\partial t} + \sum_{i=1}^{n} \frac{\partial}{\partial x_i}(p(x,t)f_i(x,t)) = 0$$
$$\Rightarrow p(x,t)dv = p(x_0, t_0)dv_0 \tag{3.7}$$

The local volume distortion due to a non linear deformation $g(x, t, t_0)$ is simply $dv = |\nabla g|_{x,t,t_0} dv_0$ and again $\Phi(x, t, t_0) = \nabla g(x, t, t_0)$. Therefore, $p(x,t) = p(x_0, t_0)\frac{dv_0}{dv} = p(x_0, t_0)\frac{1}{|\Phi(t,t_0)|}$. The percent error in the Gaussian approximation of the propagated PDF at time t is then given by:

$$Error_t = \left|1 - \frac{|\Phi(\mu, t, t_0)|f_x(x(t), \mu(t), \Sigma(t))}{p(x_0, t_0)}\right| \tag{3.8}$$

Where the density function f_x is the same as in (3.2) and $\mu(t)$ and $\Sigma(t)$ are the propagated mean and covariance.

Equation (3.8) is computed at +1, +3, and +6 sigma points along each eigenvector of the covari-

ance matrix at time t. This information could be used in real time to adaptively refine a GMM or other approximation, similar to the adaptive entropy based approaches in [71, 72]. For the results computed in the next section, CRATER implemented a single mean and covariance, derived from linearization about the expected state in orbital element space, to model the propagated PDF and uses equation (3.8) to report the point-wise error in this assumption along the different eigenvectors of the orbital element covariance matrix. This single Gaussian in orbital element space was then used to generate local Gaussians or a GMM in the Cartesian space.

In the case where we wish to consider a vector of uncertain force model parameters $q \in \mathbb{R}^m$, the state equation becomes.

$$\chi(t) = \chi_0 + \int_{t_0}^{t} f(X, q, t) d\tau \tag{3.9}$$

Where $\chi(t)$ is the augmented state vector $\chi(t) = \begin{bmatrix} \boldsymbol{X}(t) \\ \boldsymbol{q}(t) \end{bmatrix}$. Differentiating equation (3.9) with respect to χ_0 we get the state transition matrix for our augmented state.

$$\boldsymbol{\Phi}_a = \begin{bmatrix} \boldsymbol{\Phi}(t, t_0) & \boldsymbol{\Psi}(t, t_0) \\ \frac{\partial \boldsymbol{q}(t)}{\partial \boldsymbol{X}(t_0)} & \frac{\partial \boldsymbol{q}(t)}{\partial \boldsymbol{q}(t_0)} \end{bmatrix} \tag{3.10}$$

Where $\boldsymbol{\Psi} = \frac{\partial X(t)}{\partial q(t_0)}$, as discussed in [33, pp. 632–646], is given by the solution to the matrix differential equation.

$$\dot{\boldsymbol{\Psi}} = \frac{\partial \boldsymbol{f}(X, q, t)}{\partial \boldsymbol{X}} \boldsymbol{\Psi} + \frac{\partial \boldsymbol{f}(X, q, t)}{\partial \boldsymbol{q}} \qquad \boldsymbol{\Psi}_0 = 0_{nxm} \tag{3.11}$$

Of course, equation (3.10) becomes much simpler if q is made up of time and state invariant parameters such as the ballistic coefficient for a uniform spacecraft. For the results in Section 3.3 the uncertain force model parameters were assumed to be constant both spatially and temporally.

Equations (3.9) and (3.10) are then used to propagate the mean and covariance of the initial distribution. At this point, we have developed the theory to map the initial PDF of the state and parameters from t_0 to t.

Unfortunately, the orbital elements are not a computationally efficient set of variables to analyze conjunctions with, since the relative position and velocity state is not easily expressed. This means that the PDF at time t must undergo another non linear transformation into Coordinates better suited for efficient P_c analysis (Cartesian Coordinates in this case).

3.2.2 PDF Approximation

The mapping of the PDF from orbital elements into Cartesian coordinates can result in a loss of covariance realism [130]. This effect is most egregious along the eigenfiber of the covariance ellipsoid, which corresponds to the center line of the banana shaped ellipsoid in Cartesian space as seen in Figure 3.1.
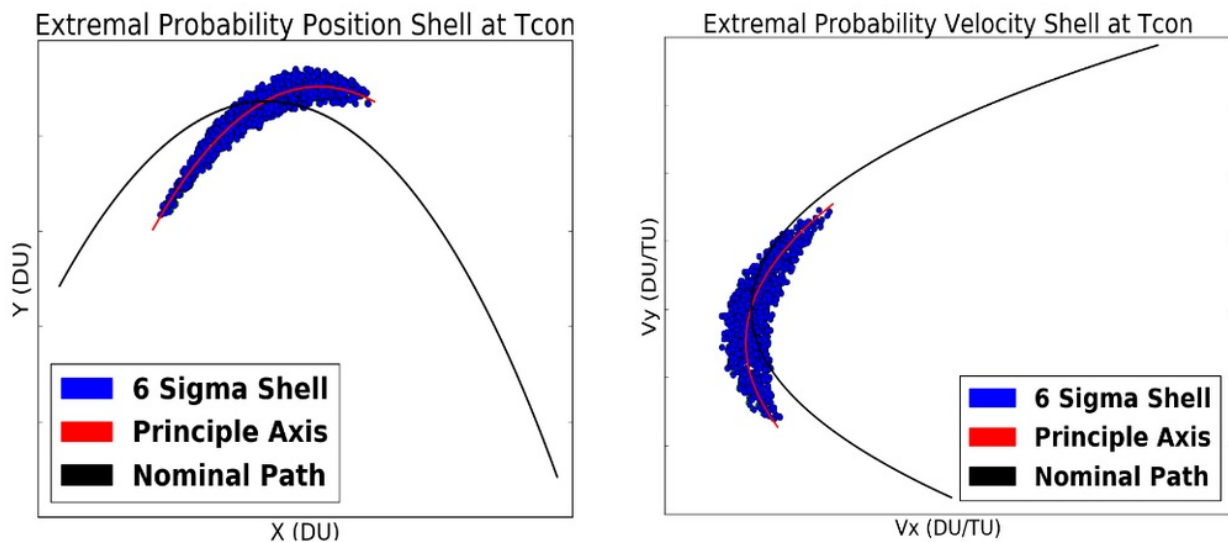
Figure 3.1: Projection of Principle Axis into Cartesian Coordinates. Reprinted with permission from [98].

Assuming that the approximate Gaussian PDF in orbital element space has sufficiently satisfied the Liouville equation, we can use the Gaussian in orbital element space as the truth for constructing a PDF in Cartesian space which also satisfies the Liouville equation. The PDF in Cartesian coordinates will be approximated locally as Gaussian in the direction of the eigenfiber and fully

49

Gaussian in the off axis directions for the CRATER algorithm. This approximation has be found to be well justified in most applications. The number of local Gaussians needed then is tied to the range of validity of the Gaussian assumption in the direction of the eigenfiber. This range can be determined by computing the error between the analytically exact mapping into Cartesian Coordinates (3.1) and a local linearly mapped PDF. The PDF with mean $\bar{P}$ and covariance Σ is given analytically in terms of Cartesian coordinates by

$$f_p\big(h^{-1}(X)\big) = \frac{1}{\sqrt{(2\pi)^n |\Sigma|}} \exp\left\{\frac{-1}{2}\big[h^{-1}(X) - \bar{P}\big]^T \Sigma^{-1}\big[h^{-1}(X) - \bar{P}\big]\right\} \frac{1}{|\nabla h(p)|_p} \quad (3.12)$$

Where $X = h(P)$, X is the Cartesian state, P is the corresponding state in orbital elements and $h : P \to X$. This exact mapping is then linearized and is substituted into (3.12) to give

$$f_x(X) = \frac{|R|_{\bar{p}}}{\sqrt{(2\pi)^n |\Sigma|}} \exp\left[\frac{-1}{2}(R\Delta X)^T \Sigma^{-1}(R\Delta X)\right] \quad (3.13)$$

Here $R = \frac{\partial P}{\partial X}$ and $\Delta X = h(P) - h(\bar{P})$. The error between the two then is simply

$$Error_c = \left|1 - \left(\frac{|R|_{\bar{p}}}{|R|_p} \exp\left\{\frac{-1}{2}\big[(\boldsymbol{R}\Delta\boldsymbol{X})^T\boldsymbol{\Sigma}^{-1}(\boldsymbol{R}\Delta\boldsymbol{X}) - (\Delta\boldsymbol{P})^T\boldsymbol{\Sigma}^{-1}(\Delta\boldsymbol{P})\big]\right\}\right)\right| \quad (3.14)$$

where $\Delta P = h^{-1}(X) - \bar{P}$. This error is evaluated along the eigenfiber of the covariance ellipsoid in element space starting at 6σ (where σ is the square root of the eigenvalue associated with the eigenfiber) and moving inward along the eigenfiber until $Error_c(\Delta P) \leq \epsilon$. Here, ϵ is a desired tolerance for the linear approximation. The number of Local Gaussians is then $12\sigma/\Delta\sigma$, such that $\Delta P = \Delta\sigma \boldsymbol{E}_\nu$ where E_ν is the eigenfiber and ΔP satisfies the linearity tolerance.

Depending on $Error_c$ and the geometry of the collision, the PDF will be approximated as a single Gaussian PDF, by the best local Gaussian PDF, or as a Gaussian Mixture Model. A GMM is used over the best local Gaussian when the relative angle between the orbital planes is low.

To define the local Gaussian approximation, consider a PDF in Cartesian Space that is most non Gaussian along the direction corresponding the eigenfiber of the covariance ellipse in orbital

element space. Points are placed sufficiently dense along this axis such that equation (3.14) globally satisfies a desired tolerance. These points are the nodes where the local Gaussians will be created. As the PDFs of the two satellites pass through each other the Gaussians of the two closest nodes are used to create the joint PDF for evaluation in Coppola's integral.

To create a local Gaussian in the vicinity of a node point P_i in orbital element space, consider the following: We are interested in creating a locally valid Gaussian in Cartesian space in the neighborhood of $h(P_i)$ where h is the mapping from a point in element space to the corresponding point in Cartesian space. Suppose the point we are interested in can be expressed as

$$P = (P - P_i) + (P_i - \bar{P}) + \bar{P} \tag{3.15}$$

where $\bar{P}$ is the mean of the distribution and $(P - P_i)$ is assumed to be small such that it can be accurately approximated linearly as:

$$\Delta P_i = (P - P_i) = \frac{\partial P}{\partial X} \Delta X_i \tag{3.16}$$

where ΔX_i is $X - h(P_i)$. Note this assumption is justified in evaluating the joint PDF over the sphere defined by the radius of collision, but may break down when integrating over the velocities entering the sphere, as is required when the collision is defined as it is in equation (3.22)

Plugging (3.15) and (3.16) back into the Gaussian defined in element space the exponent of the Gaussian becomes.

$$\frac{-1}{2} (R\Delta X_i + \Delta \bar{P})^T \Sigma^{-1} (R\Delta X_i + \Delta \bar{P}) \tag{3.17}$$

Where $R = \frac{\partial P}{\partial X}$ evaluated at P_i and $\Delta \bar{P} = (P_i - \bar{P})$. This can be rearranged to the following.

$$\frac{-1}{2} \left[(\Delta X + M\lambda)^T M^{-1} (\Delta X + M\lambda) + \Delta \bar{P}^T \left(\Sigma^{-1} - \Sigma^{-1} R M R^T \Sigma^{-1} \right) \Delta \bar{P} \right] \tag{3.18}$$

Where $M = (R^T \Sigma^{-1} R)^{-1}$ and $\lambda = R^T \Sigma^{-1} \Delta \bar{P}$. Note that the second term in (3.18) reduces

to zero. Thus the local Gaussian in the neighborhood of X_i is

$$f_x(X) = \frac{1}{\sqrt{(2\pi)^n |\Sigma|}} \exp\left\{ \frac{-1}{2} \left[X - (X_i - R^{-1}\Delta\bar{P}) \right]^T M^{-1} \left[X - (X_i - R^{-1}\Delta\bar{P}) \right] \right\} \quad (3.19)$$

If we desire to integrate (3.19) in the Cartesian domain we must include the determinant of the Jacobian of the transformation R. Since $\frac{1}{\sqrt{|M|}} = \frac{|R|}{\sqrt{|\Sigma|}}$, the integral of (3.19) can simply be written as the integral of a normal distribution $N(X, \mu, M)$ over X with a mean of $(X_i - R^{-1}\Delta\bar{P})$ and covariance M

$$\int f_x(X)dX = \int N\big(X, (X_i - R^{-1}\Delta\bar{P}), M\big)dX \quad (3.20)$$

The Local Gaussians have poor global error characteristics, especially when compared to other forms of approximating the PDF such as GMM. What motivates their use here is their superior local error characteristics, since the radius of collision is usually on the order of $0.01km - 0.1km$ while the 6σ contours of the PDF may span hundreds of kilometers, two local Gaussians in the neighborhood of the hardball radius can generate a very good local estimate of the joint PDF, especially in cases where the relative inclination between the orbits is high as shown in Figure 3.2.
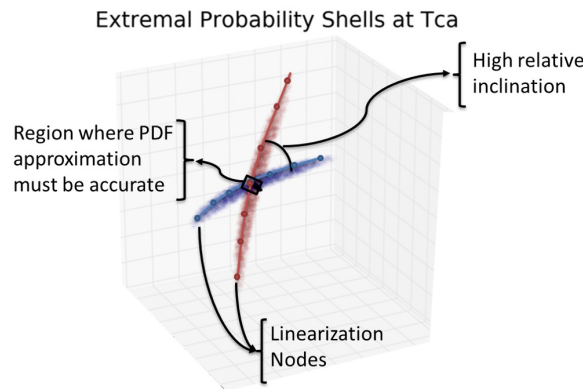
Figure 3.2: Influence of Collision Geometry on the Joint PDF. Reprinted with permission from [98].

In the event that a GMM is needed, the methods outlined in [72, 130] are used. However, instead of using the algorithms in [130] to generate the GMM, the number of mixture components is determined by a nonlinearity index (η_i) evaluated along the eigenfiber of the PDF.

$$\eta_i = \frac{||\nabla h(P_i) - \nabla h(\bar{P})||_2}{||\nabla h(\bar{P})||_2} \tag{3.21}$$

In equation (3.21) h and $\bar{P}$ are as defined in (3.12) where ∇ denotes the gradient and $|| \cdot ||_2$ is the 2-norm. P_i is moved in along the eigenfiber until η_i satisfies a desired nonlinearity tolerance. The $\Delta\sigma$ is computed as before and the number of mixture components (n) is then $12\sigma/\Delta\sigma$. Equation (3.21) is used here as opposed to (3.14) as (3.14) tends to over predict the the number of Gaussians needed to construct a global approximation.

Each mixture component is given the same covariance matrix and placed along the eigenfiber such that $\mu_i = r \tan(\theta_i)$, $\theta_i = linspace(-\frac{\pi}{4}, \frac{\pi}{4})$ and r is equal to $min\Big(max\big(GH\_node(n)\big), 6\Big)$.

The function $GH\_node(n)$ simply returns all of the roots of the nth degree Hermite polynomial [115]. The covariance of each mixture is the same as the original except the principle eigenvalue is weighted by a scalar $sigscalar = 0.5 * \frac{1.0+n}{n^k}$. The weights are computed offline according to algorithm 1 from [130] and are loaded by the CRATER algorithm if needed. Each mixture component is propagated through the collision window using the full nonlinear dynamics and are mapped into Cartesian coordinates using the 4th order Conjugate Unscented Transform points [58].

3.2.3 PC Integral

Recall from Coppola [96] that Λ_t is the set of all trajectories from satellites 1 and 2 that result in a collision at some time $t \in (t_0, t_0 + T]$ and is defined below.

$$\Lambda_t = \{X(t)|r(t) = R_c \text{ and } (v \cdot \hat{r}) \le 0\} \tag{3.22}$$

Where $r(t)$ is the relative distance along the unit vector $\hat{r}$, v the relative velocity of the two satellites, and R_c is the radius of collision [76]. With Λ_t defined in this manner, assuming the satellites

have large initial separation, integrating the joint density function $\rho(X, t; t_0)$ over the union of all Λ_t gives the probability of collision between the two satellites as seen in equation (3.23).

$$P_I = \int_{t_0}^{t_0+T} \int_{\Lambda_t} \rho(X, t; t_0) |v \cdot \hat{r}| dA_{\Lambda_t} dt \tag{3.23}$$

Where $|v \cdot \hat{r}|$ is an artifact from the change of variables $dr = \frac{dr}{dt} dt$.

With the addition of a vector of uncertain force model parameters q, dA_{Λ_t} is given by:

$$dA_{\Lambda_t} = R_c^2 cos(\theta) dx_1 dq dv d\theta d\phi \tag{3.24}$$

Here x_1 is the six dimensional state of satellite 1, v is the three dimensional relative velocity, and θ and ϕ are the azimuth and elevation of the vector $\hat{r}$.

Substituting equation (3.24) back into (3.23) it is apparent that we will need to integrate over $2d + m$ dimensions where d is the dimension of the state and m is the dimension of the parameter vector q. If the density function $\rho(\chi, t; t_0)$ (where χ is the same as in equation (3.9)) is the normal distribution or can be expressed as a sum of Gaussian PDFs, then the integral over all but three of these dimensions can be evaluated analytically. This is demonstrated in [96] and [72] and is only briefly summarized here.

Following the development in [96], see [72] for GMM development, if $\rho(\chi, t; t_0)$ is the normal distribution, with satellite 1 and 2 moving independently of each other, then equation (3.23) becomes the following.

$$P_I = \int_{t_0}^{t_0+T} \int_{\Lambda_t} N\big[\chi_1(t), \mu_{\chi_1}(t), \Sigma_{\chi_1}(t)\big] N\big[\chi_2(t), \mu_{\chi_2}(t), \Sigma_{\chi_2}(t)\big] |v \cdot \hat{r}| dA_{\Lambda_t} dt \tag{3.25}$$

If we let $\chi_2 = \chi_r + \chi_1$, where χ_r is the relative state and substitute back into (3.25) then we obtain a joint PDF that is a function of the state of satellite 1 and the relative state. The product of

Gaussians in equation (3.25) can then be manipulated to obtain the distribution of the relative state

$$N\big[\chi_1(t), \mu_{\chi_1}(t), \Sigma_{\chi_1}(t)\big] N\big[\chi_2(t), \mu_{\chi_2}(t), \Sigma_{\chi_2}(t)\big] =$$
$$N\big[\chi_1(t) + T\chi_r(t), \mu_{\chi_1}(t) + T\mu_{\chi_r}(t), M(t)\big] N\big[\chi_r(t), \mu_{\chi_r}(t), \Sigma_{\chi_r}(t)\big] \tag{3.26}$$

where $\mu_{\chi_r} = \mu_{\chi_2} - \mu_{\chi_1}$, $\Sigma_{\chi_r} = \Sigma_{\chi_1} + \Sigma_{\chi_2}$, $M^{-1} = \Sigma_{\chi_1}^{-1} + \Sigma_{\chi_2}^{-1}$ and $T = M\Sigma_{\chi_2}^{-1}$. Substituting equation (3.26) into (3.25), the expression can then be integrated analytically over χ_1 leaving the joint PDF exclusively in terms of the relative state χ_r.

$$P_I = \int_{t_0}^{t_0+T} \int_{\Lambda'_t} N\big[\chi_r(t), \mu_{\chi_r}(t), \Sigma_{\chi_r}(t)\big] |v \cdot \hat{r}| R_c^2 cos(\theta) dq dv d\theta d\phi dt \tag{3.27}$$

The integration over dq is handled using Lemma I from Coppola's paper. That is, the Gaussian PDF in equation (3.27) is split into two portions such that a Gaussian with full state uncertainty and m uncertain force model parameters is given by the following.

$$N_{6+m}(\chi_r, \mu_{\chi_r}, \Sigma_{\chi_r}) = N_6(X_r, \mu_{x_r}, \Sigma_{x_r}) N_m(q', \mu'_q, \Sigma') \tag{3.28}$$

Since the portion of the PDF containing the relative state X_r does not depend on q, it can be pulled out of the integral over dq and the integral of $N_m(q', \mu'_q, \Sigma')$ over dq evaluates to 1. Of course this assumes that the distributions are Gaussian. If the distributions are not Gaussian, it may not be possible to separate the PDF into two parts as described in the previous paragraph. To get around this difficulty CRATER will approximate the PDF using the LG (when possible) or GMM method, since both of these methods can make use of the analytical marginalization described above.

From this point forward, one can follow the rest of Coppola's derivation to arrive at the same formulation for P_c, but now taking into account the effects of parametric uncertainty. The numerical quadrature over θ and ϕ is computed using Lebedev quadrature [133], while the quadrature over time is handled using Python's numpy.trapz.

This formulation of the P_c is subject to the following assumptions:

A1. Trajectories only enter the hardball radius once

A2. Trajectories do not satisfy $r(t) = R_c$ (where $r(t)$ is the relative distance between the satellites) for a finite amount of time, such that each trajectory belongs to a unique Λ_t

A3. The dynamics and PDF of each object are independent

A4. The PDF at time T can be modeled as a Gaussian Mixture or is locally Gaussian

Under these assumptions, CRATER will be able to consider conjunctions with parametric model uncertainty, full state uncertainty, long encounter times, and non-Gaussian PDFs (in Cartesian space). It is felt that this level of generality, adaptability, accuracy and numerical efficiency, sets a new standard in conjunction analysis.

3.3   Results and Discussion

The CRATER algorithm has been tested so far on eight different test cases. For the test cases below, the P_c was computed using four different methods. The single Gaussian (SG) method, assumes that the PDF in Cartesian space is adequately modeled by a single mean and covariance and the P_c is computed with respect to Coppola's result allowing for non linear relative motion. The second and third methods used were the local Gaussian approximation (LG) and the Gaussian mixture model GMM as described in Section 3.2. These results are then compared with the fourth method; a Monte Carlo (MC) simulation.

To facilitate easily verifiable and illuminating comparison, all test cases except IV, V, and VIII use unperturbed Keplarian motion as the force model. Test case IV includes J2 and cases V and VIII include a simplified version of the Harris Priester drag model [134] . In the tables below, the approximate time of closest approach (T_{CA}) as well as the screening period relative to the epoch time is given as a scalar multiple of the orbital period of either satellite 1 or 2, where the orbital period for satellites 1 and 2 are denoted T_1 and T_2 respectively. Test Case IV involves a collision where there is uncertainty in the J2 parameter. J2 was chosen as the uncertain parameter for test case IV, merely to demonstrate that CRATER is not limited to drag uncertainty only. It should be noted that the initial conditions for the test cases below have been converted from normalized modified equinoctial orbital elements to ECI Cartesian coordinates and Kepler orbital elements to

help the reader visualize the scenario.

With each set of results is listed the convergence interval (ϵ) of the Monte Carlo result as computed by the Dagum bound [106] with a confidence of $(1 - \alpha) = 95\%$. The Dagum convergence interval (ϵ) in equation (3.29) is used to compute the lower bound of the number of Monte Carlo samples (N) needed to ensure the predicted value of the P_c is within $\pm\epsilon\%$ of the true P_c value (P_T) with a confidence of $(1 - \alpha)$. In equation (3.29) e is Euler's number.

$$N > \frac{4(e - 2)(1 - P_T)}{\epsilon^2 P_T} \ln\left(\frac{2}{\alpha}\right) \tag{3.29}$$

The Dagaum bound has the advantage of requiring far fewer MC samples than other methods, such as the Chernoff-Hoeffding bound [104], in cases where the expected value of P_T is known and $\epsilon * P_T < (1 - P_T) * P_T$ as discussed in [89]. For the ϵ computed in the tables below, the MC result was used for P_T along with the stated number of MC samples. Except for test case VII, which used the LG result for P_T.

In addition to P_c results, the run times of each method on the different test cases are also given. The LG P_c and run time are then compared to the Monte Carlo predicted P_c and run time and are presented in the LG percent error column, giving the percent difference between the LG and MC P_c result and how much faster the LG method was computed by taking the MC run time divided by the LG run time.

3.3.1 Test Case I

The test case in Table 3.1 was run with a radius of collision $R_c = 1.0 km$ and verified via a 100 million sample Monte Carlo. Results are shown in Table 3.2. The screening interval was $[1.24\ T_1, 1.26 T_1]$.

Table 3.1: Initial Conditions Test Case I. Reprinted with permission from [98].

$T_{CA} = 1.25T_1$	**Orbit 1**	**Orbit 2**
a	10000 km	10000 km
e	1.0e-7	1.0e-7
i	90.0	90.0
ω	0.0	0.0
Ω	0.0	90.0
θ	0.0	0.0
$\sigma_X^2, \sigma_Y^2,$	1.0e-2 $(km)^2$	1.0e-2 $(km)^2$
$\sigma_Z^2,$	1.0e-1 $(km)^2$	1.0e-1 $(km)^2$
$\sigma_{V_x}^2, \sigma_{V_y}^2,$	1.0e-5 $(km/s)^2$	1.0e-5 $(km/s)^2$
$\sigma_{V_z}^2,$	1.0e-4 $(km/s)^2$	1.0e-4 $(km/s)^2$

Table 3.2: Results Test Case I. Reprinted with permission from [98].

	SG	LG	GMM	MC	LG % Error	Dagum ϵ
P_c	2.809E-4	2.809E-4	2.769E-4	2.675E-4	5.0%	1.9%
Time	2.6 sec	5.6 sec	1728 sec	26299 sec	4.6E3 faster	

3.3.2 Test Case II

Table 3.3: Initial Conditions Test Case II. Reprinted with permission from [98].

$T_{CA} = 1.237T_1$	**Orbit 1**	**Orbit 2**
a	10000 km	9935 km
e	1.0e-7	1.0e-7
i	90.0	93.0
ω	0.0	0.0
Ω	0.0	90.0
θ	0.0	2.0
$\sigma_X^2, \sigma_Y^2,$	1.0e-2 $(km)^2$	1.0e-2 $(km)^2$
$\sigma_Z^2,$	1.0e-1 $(km)^2$	1.0e-1 $(km)^2$
$\sigma_{V_x}^2, \sigma_{V_y}^2,$	1.0e-5 $(km/s)^2$	1.0e-5 $(km/s)^2$
$\sigma_{V_z}^2,$	1.0e-4 $(km/s)^2$	1.0e-4 $(km/s)^2$

The test case defined in Table 3.3 was run with $R_c = 1.0km$ and verified via a 164 million sample Monte Carlo. Results are in Table 3.4 The screening interval was [1.228 T_1, 1.26T_1].

Table 3.4: Results Test Case II. Reprinted with permission from [98].

	SG	LG	GMM	MC	LG % Error	Dagum ϵ
P_c	3.53E-5	5.97E-5	5.993E-5	5.892E-5	1.36%	1.0 %
Time	2.7 sec	5.1 sec	436 sec	65250 sec	1.2E4 faster	

3.3.3 Test Case III

Table 3.5: Initial Conditions Test Case III. Reprinted with permission from [98].

$T_{CA} = 1.0T_2$	**Orbit 1**	**Orbit 2**
a	7000 km	24500 km
e	1.0e-7	0.714285714286
i	0.0	40.0
ω	0.0	0.0
Ω	0.0	0.0
θ	-197.244	0.0
$\sigma_X^2, \sigma_Y^2,$	1.0e-2 $(km)^2$	1.0e-2 $(km)^2$
$\sigma_Z^2,$	1.0e-1 $(km)^2$	1.0e-1 $(km)^2$
$\sigma_{V_x}^2, \sigma_{V_y}^2,$	1.0e-5 $(km/s)^2$	1.0e-5 $(km/s)^2$
$\sigma_{V_z}^2,$	1.0e-4 $(km/s)^2$	1.0e-4 $(km/s)^2$

The test case defined in Table 3.5 was run with $R_c = 0.5km$ and verified via a 100 million sample Monte Carlo. Results are in Table 3.6 The screening interval was [0.9999 T_2, 1.0001T_2].

Table 3.6: Results Test Case III. Reprinted with permission from [98].

	SG	LG	GMM	MC	LG % Error	Dagum ϵ
P_c	9.29E-4	9.29E-4	9.893-4	9.740E-4	4.62%	1.0%
Time	4.1 sec	4.4 sec	4842	25038 sec	5.7E3 faster	

3.3.4   Test Case IV

Table 3.7: Initial Conditions Test Case IV. Reprinted with permission from [98].

$T_{CA} = 5.017T_1$	**Orbit 1**	**Orbit 2**
a	7000 km	7000 km
e	1.0e-7	1e-7
i	90.0	90.0
ω	0.0	0.0
Ω	0.0	90.0
θ	-90	-90.0
$\sigma_X^2, \sigma_Y^2, \sigma_Z^2,$	1.0e-4 $(km)^2$	1.0e-4 $(km)^2$
$\sigma_{V_x}^2, \sigma_{V_y}^2, \sigma_{V_z}^2,$	1.0e-12 $(km/s)^2$	1.0e-12 $(km/s)^2$
$\sigma_{J2}^2,$	$(J2/10)^2$	$(J2/10)^2$

The test case defined in Table 3.7 was run with $R_c = 0.05km$ and verified via a 100 million sample Monte Carlo. Results are in Table 3.8 The screening interval was [5.008 T_1, 5.026T_1].

Table 3.8: Results Test Case IV. Reprinted with permission from [98].

	SG	LG	GMM	MC	LG % Error	Dagum ϵ
P_c	6.149E-4	6.149E-4	6.047E-4	2.21e-4	178%	2.2 %
Time	16.27 sec	16.8 sec	4821 sec	26200 sec	1.5E3 faster	

3.3.5 Test Case V

Table 3.9: Initial Conditions Test Case V. Reprinted with permission from [98].

$T_{CA} = 0.877T_1$	**Orbit 1**	**Orbit 2**
a	6500 km	6500 km
e	1.0e-7	1e-7
i	90.0	90.0
ω	0.0	0.0
Ω	0.0	90.0
θ	-90	-90.0
$\sigma_X^2, \sigma_Y^2, \sigma_Z^2,$	1.0e-6 $(km)^2$	1.0e-6 $(km)^2$
$\sigma_{V_x}^2, \sigma_{V_y}^2, \sigma_{V_z}^2,$	1.0e-9 $(km/s)^2$	1.0e-9 $(km/s)^2$
$\sigma_{BC}^2,$	$(BC/100)^2$	$(BC/100)^2$

The test case defined in Table 3.9 was run with $R_c = 1.0km$ and verified via a 51 million sample Monte Carlo. Results are shown in Table 3.10 The screening interval was [0.872 T_1, 0.8795T_1]. The nominal ballistic coefficient (BC) was 0.0196 m^2/kg.

Table 3.10: Results Test Case V. Reprinted with permission from [98].

	SG	LG	GMM	MC	LG % Error	Dagum ϵ
P_c	12.1E-3	12.1E-3	9.872E-3	5E-3	142%	0.6 %
Time	8.2 sec	8.9 sec	4842 sec	28000 sec	3.1E3 faster	

3.3.6 Test Case VI

Table 3.11: Initial Conditions Test Case VI. Reprinted with permission from [98].

$T_{CA} = 1.237T_1$	**Orbit 1**	**Orbit 2**
a	10000 km	9913 km
e	1.0e-7	1e-7
i	90.0	93.0
ω	0.0	0.0
Ω	0.0	89.0
θ	0.0	2.0
$\sigma_X^2, \sigma_Y^2,$	1.0e-2 $(km)^2$	1.0e-2 $(km)^2$
$\sigma_Z^2,$	1.0e-1 $(km)^2$	1.0e-1 $(km)^2$
$\sigma_{V_x}^2, \sigma_{V_y}^2,$	1.0e-5 $(km/s)^2$	1.0e-6 $(km/s)^2$
$\sigma_{V_z}^2,$	1.0e-4 $(km/s)^2$	1.0e-5 $(km/s)^2$

The test case defined in Table 3.11 was run with $R_c = 1.0km$ and verified via a 500 million sample Monte Carlo. Results are shown in Table 3.12. The screening interval was [1.227 T_1, 1.247T_1].

Table 3.12: Results Test Case VI. Reprinted with permission from [98].

	SG	LG	GMM	MC	LG % Error	Dagum ϵ
P_c	7.966E-9	1.235E-5	1.205E-5	1.200E-5	2.92%	4.2 %
Time	20.7 sec	25.6 sec	258 sec	32000 sec	1.2E3 faster	

The difference of the SG result compared to the others is understood when looking at the collision geometry in Figure 3.3. Significant non-Gaussian behavior has developed in the distribution of satellite 1, as is seen when contrasting the blue (true) distribution with the pink (Gaussian) distribution. Whereas, the true distribution of satellite 2 (green) is still relatively Gaussian. Since the intersection of the distributions of satellites 1 and 2 occurs almost exclusively between the blue and green distributions the SG method will result in a gross under prediction of the true P_c.
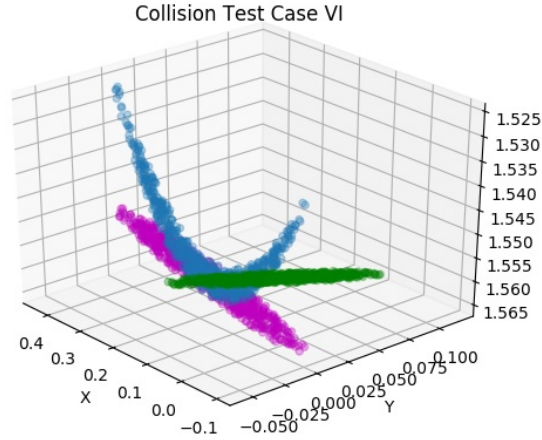
Figure 3.3: TC VI Collision Geometry. Reprinted with permission from [98].

3.3.7 Test Case VII

Table 3.13: Initial Conditions Test Case VII. Reprinted with permission from [98].

$T_{CA} = 1.237T_1$	**Orbit 1**	**Orbit 2**
a	7000 km	6970 km
e	1.0e-7	1e-7
i	90.0	93.0
ω	0.0	0.0
Ω	0.0	40.0
θ	0.0	2.0
$\sigma_X^2, \sigma_Y^2,$	1.0e-2 $(km)^2$	1.0e-2 $(km)^2$
$\sigma_Z^2,$	1.0e-1 $(km)^2$	1.0e-1 $(km)^2$
$\sigma_{V_x}^2, \sigma_{V_y}^2,$	1.0e-5 $(km/s)^2$	1.0e-6 $(km/s)^2$
$\sigma_{V_z}^2,$	1.0e-4 $(km/s)^2$	1.0e-5 $(km/s)^2$

The test case defined in Table 3.13 was run with $R_c = 1.0km$ and verified via a 100 million sample Monte Carlo. Results are shown in Table 3.14. The screening interval was [1.217 T_1, 1.247T_1].

Table 3.14: Results Test Case VII. Reprinted with permission from [98].

	SG	LG	GMM	MC	LG % Error	Dagum ϵ
P_c	2.790E-5	2.187E-11	3.094E-11	0.0	NA	6960 %
Time	20.3 sec	25.4 sec	106 sec	27800 sec	1.1E3 faster	

In contrast to the test case VI, this case was designed to yield a higher P_c if an incorrect Gaussian assumption was made for satellite 1. In Figure 3.4 below we see the distribution of satellite 2 (green) predominantly intersecting the Gaussian approximation of satellite 1's distribution (pink).
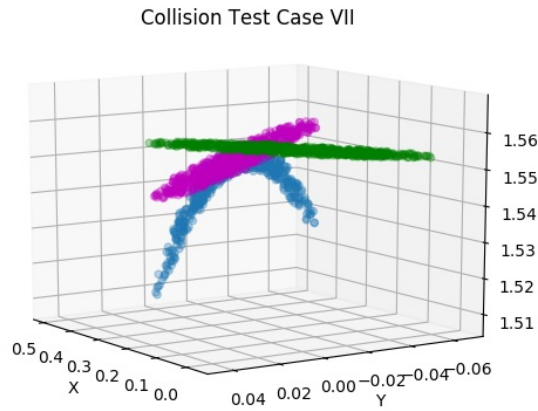
Figure 3.4: TC VII Collision Geometry. Reprinted with permission from [98].

3.3.8 Test Case VIII

Table 3.15: Initial Conditions Test Case VIII. Reprinted with permission from [98].

$T_{CA} = 0.9999T_1$	**Orbit 1**	**Orbit 2**
a	6600 km	6600 km
e	1.0e-7	1.0e-7
i	90.0	90.0
ω	0.0	0.0
Ω	0.0	90.0
θ	-90	-90.0
σ_X^2,	1.0e-3 $(km)^2$	1.0e-4 $(km)^2$
σ_Y^2,	1.0e-4 $(km)^2$	1.0e-3 $(km)^2$
σ_Z^2,	1.0e-4 $(km)^2$	1.0e-4 $(km)^2$
$\sigma_{V_x}^2, \sigma_{V_y}^2, \sigma_{V_z}^2$,	1.0e-8 $(km/s)^2$	1.0e-8 $(km/s)^2$
σ_{BC}^2,	$(0.2BC)^2$	$(0.2BC)^2$

The test case defined in Table 3.15 was run with $R_c = 0.1km$ and verified via a 1 million sample Monte Carlo. Results are shown in Table 3.16. The screening interval was [0.999725 T_1, 1.0001T_1]. The nominal ballistic coefficient (BC) was 0.0196 m^2/kg.

Table 3.16: Results Test Case VIII. Reprinted with permission from [98].

	SG	LG	GMM	MC	LG % Error	Dagum ϵ
P_c	1.298E-2	1.298E-2	1.298E-2	1.2562E-2	3.33%	2.8 %
Time	3.4 sec	5.6 sec	28.5 sec	287 sec	50x faster	

To demonstrate the effects of force model uncertainty on the predicted P_c, this test case was run using a range of different uncertainties for the ballistic coefficient. Since the collision was nearly deterministic before considering drag uncertainty, the effect of adding more drag uncertainty was to decrease the likelihood of the collision as shown in Figure 3.5.
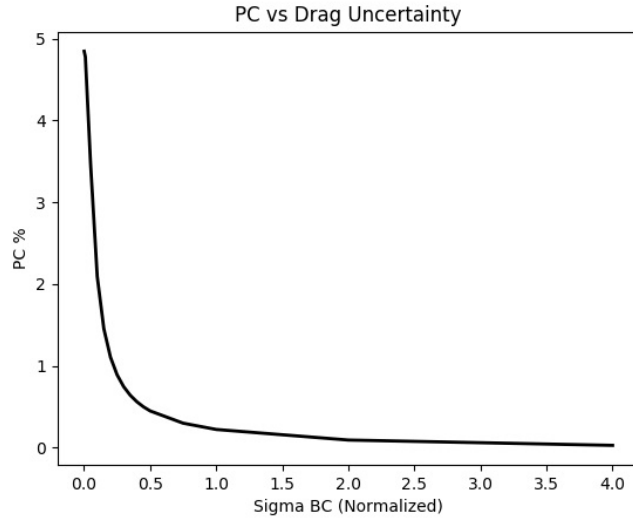
Figure 3.5: P_c vs Drag Uncertainty. Reprinted with permission from [98].

3.3.9 Propagation Error

Notice, from the last section, that there was good agreement between CRATER results and Monte Carlo results for all test cases except cases IV and V. The reason for this is most likely explained by the results in the following table.

Table 3.17: Propagation Error. Reprinted with permission from [98].

Test Case	I	II	III	IV	V	VI	VII	VIII
$1\,\sigma$ Error	9.7%	6.3 %	88.4%	100%	100%	7.7 %	7.2 %	23 %

Table 3.17 shows the maximum 1σ propagation error for the PDF in orbital element space. That is the percent difference as predicted by (3.8). Recall that the error was computed at $+1$, $+3$, and $+6$ sigma along each eigenvector of the distribution. The maximum 1σ error was invariably along the eigenfiber in all test cases. For test cases IV and V the error at 1σ along the eigenfiber has saturated at 100% and was significant along the other eigenvectors. In other words these test cases violated the assumption that the PDF remains Gaussian in orbital element space.

66

Notice in all cases where the Gaussian assumption in orbital element space was met, the LG approach yielded small single digit percentage errors in P_c with about one order of magnitude speedup relative to GMM. In fact the computational burden was more comparable to the linear analysis SG, but for the most nonlinear conjunction scenarios corrected errors of 4 to 6 orders of magnitude when estimating P_c.

3.3.10 Sensitivity of P_c Results

One question with any simulation is: How good are the results? This worry alone has driven some operators to doubt the fidelity of the P_c computed and therefore to simply ignore conjunction warnings. CRATER seeks to address this concern by quantifying the error in the propagated PDF with respect to the Fokker Planck equation, as well as computing the sensitivity of the computed probability of collision to variations in the initial distributions.

Prior work shows that the P_c can vary by orders of magnitude with respect to distribution parameters and associated assumptions. Often these works also present the maximum probability of collision [88, 122], in which, the eigenvalues that give the maximum probability of collision are found. What is frequently missing from this discussion however, is the likelihood of the distribution from which the maximum probability of collision was computed. In other words, the maximum P_c is a conditional probability and will likely not accurately represent the threat of a collision without knowing how likely the initial distribution was that resulted in the max P_c. Unfortunately this likelihood function is not in general known, leaving limited options when wishing to consider the P_c with uncertainty in the initial distribution. If the likelihood function is known then the P_c can be computed which properly takes into account the uncertainty in the initial distribution using the law of total probability. One quantity that is readily computed is the sensitivity of the P_c to perturbations in the initial distribution. Using CRATER, the sensitivity of the P_c can be computed for collisions with longer encounter times and non Gaussian distributions.

Earlier methods for computing P_c rely on linearizing the dynamics and may not consider full state uncertainty [76, 88, 85, 87, 84]. For most collision candidates these assumptions are justified and convenient, but can cause problems in more non-linear collision scenarios. CRATER builds

on the works of [74, 72, 96] which avoids these limiting assumptions, but is still in a form where the sensitivity is easily computed.

The probability of collision computed using two local Gaussians or two components of a GMM is given by.

$$P_I = \int_{t_0}^{t_f} \int_0^{2\pi} \int_{\frac{-\pi}{2}}^{\frac{\pi}{2}} \mathcal{N}_3(\boldsymbol{r}, \boldsymbol{\mu}_r(t), \boldsymbol{A}(t)) \nu(\hat{\boldsymbol{r}}, t) R^2 \cos\theta \ d\theta \ d\phi \ dt \qquad (3.30)$$

Where $\mathcal{N}_3$ is a normal distribution with mean $\boldsymbol{\mu}_r = \boldsymbol{\mu}_2 - \boldsymbol{\mu}_1$ and covariance $\boldsymbol{A} = P_1 + P_2$, and $\nu(\hat{\boldsymbol{r}}, t)$ is the 1D analytical integral of the relative velocity along the direction $\hat{\boldsymbol{r}}$ as derived in [96].

If the eigenvalues of the initial covariance matrices P_{01} and P_{02} were scaled by scalars α_1, α_2 respectively, then Equation (3.30) can be differentiated with respect to these scalars to find the sensitivity of the P_c.

$$\begin{aligned} \frac{\partial P_I}{\partial \alpha_i} = \int_{t_0}^{t_f} \int_0^{2\pi} \int_{\frac{-\pi}{2}}^{\frac{\pi}{2}} &\left(\frac{\partial \mathcal{N}_3(\boldsymbol{r}, \boldsymbol{\mu}_r(t), \boldsymbol{A}(t))}{\partial \alpha_i} \nu(\hat{\boldsymbol{r}}, t) + \right. \\ &\left. \mathcal{N}_3(\boldsymbol{r}, \boldsymbol{\mu}_r(t), \boldsymbol{A}(t)) \frac{\partial \nu(\hat{\boldsymbol{r}}, t)}{\partial \alpha_i} \right) R^2 \cos\theta \ d\theta \ d\phi \ dt \end{aligned} \qquad (3.31)$$

Once the terms $\frac{\partial \mathcal{N}_3(\boldsymbol{r}, \boldsymbol{\mu}_r(t), \boldsymbol{A}(t))}{\partial \alpha_i}$ and $\frac{\partial \nu(\hat{\boldsymbol{r}}, t)}{\partial \alpha_i}$ are computed the expression in (3.31) is easily evaluated via numerical integration.

Expansion of equation (3.31) $\frac{\partial \mathcal{N}_3(\boldsymbol{r}, \boldsymbol{\mu}_r(t), \boldsymbol{A}(t))}{\partial \alpha_i}$ and $\frac{\partial \nu(\hat{\boldsymbol{r}}, t)}{\partial \alpha_i}$

$$\frac{\partial \mathcal{N}_3(\boldsymbol{r}, \boldsymbol{\mu}_r(t), \boldsymbol{A}(t))}{\partial \alpha_i} = \frac{\partial}{\partial \alpha_i} \left(\frac{1}{\sqrt{2\pi^d det(\alpha_1 P_1 + \alpha_2 P_2)}} exp - 0.5\Delta r^T (\alpha_1 P_1 + \alpha_2 P_2)^{-1} \Delta r \right) \qquad (3.32)$$

Let $K(\alpha) = det(\alpha_1 P_1 + \alpha_2 P_2)$ and recall $\boldsymbol{A} = \alpha_1 P_1 + \alpha_2 P_2$ then

$$\begin{aligned} \frac{\partial \mathcal{N}_3}{\partial \alpha_i} = &\left(\frac{-1}{2\sqrt{2\pi^d} K^{3/2}} \frac{\partial K}{\partial \alpha_i} exp(-0.5\Delta r^T (A)^{-1} \Delta r) \right) + \\ &\left(\frac{1}{\sqrt{2\pi^d K}} exp(-0.5\Delta r^T (A)^{-1} \Delta r)(-0.5\Delta r^T \frac{\partial A^{-1}}{\partial \alpha_i} \Delta r) \right) \end{aligned} \qquad (3.33)$$

Where

$$\frac{\partial K}{\partial \alpha_i} = det(A)tr(A^{-1}P_i) \tag{3.34}$$

and

$$\frac{\partial A^{-1}}{\partial \alpha_i} = -A^{-1}P_iA^{-1}. \tag{3.35}$$

Now we wish to consider $\frac{\partial \nu(\hat{r},t)}{\partial \alpha_i}$.

$$\nu(\hat{r},t) = \frac{\sigma}{\sqrt{2\pi}}e^{-\frac{\nu_0^2}{2\sigma^2}} - \frac{\nu_0}{2}[1 - erf(\frac{\nu_0}{\sigma\sqrt{2}})] \tag{3.36}$$

$$\frac{\partial \nu(\hat{r},t)}{\partial \alpha_i} = \frac{1}{\sqrt{2\pi}}\frac{\partial \sigma}{\partial \alpha_i}e^{-U} - \frac{\sigma}{\sqrt{2\pi}}e^{-U}\frac{\partial U}{\partial \alpha_i} - \frac{\partial \nu_0}{2\partial \alpha_i}[1 - erf(\sqrt{U})] + \frac{\nu_0}{2}\frac{\partial erf(\sqrt{U})}{\partial \alpha_i} \tag{3.37}$$

Where $U = \frac{\nu_0^2}{2\sigma^2}$ and let $r^* = R\hat{r} - \boldsymbol{\mu}_r$ then

$$\frac{\partial \nu_0}{\partial \alpha_i} = \hat{r}^T[B_iA^{-1}r^* + B_iA^{-1}P_iA^{-1}r^*] \tag{3.38}$$

and

$$\frac{\partial \sigma^2}{\partial \alpha_i} = \hat{r}^T[C_i - (B_iA^{-1}B^T + BA^{-1}P_iA^{-1}B^T + BA^{-1}B_i^T)]. \tag{3.39}$$

And finally,

$$\frac{\partial erf(\sqrt{U})}{\partial \alpha_i} = \frac{e^{-U}}{\sqrt{\pi U}}\frac{\partial U}{\partial \alpha_i} \tag{3.40}$$

For the sensitivity analysis, we consider four test cases. Test Case I represents a nominal collision scenario where 2D methods would be adequate. Test cases VI and VII are cases where the linear analysis under predicts and over predicts the P_c respectively and Test Case VIII is a nominal case with uncertainty in the ballistic coefficient. The initial eigenvalues of the two distributions are independently scaled by $\pm 10\%$ yeilding four P_c results for each test case the nominal max and min P_c are then plotted for each test case, showing the sensitivity in the P_c to a ten percent change

in the Eigenvalues using equation (3.31). In addition to this analysis the mean of the distribution was allowed to vary within its 95% confidence bound, based on a theoretical 1000 sample mean, the 95% confidence bound on the P_c was then numerically computed via Monte Carlo.
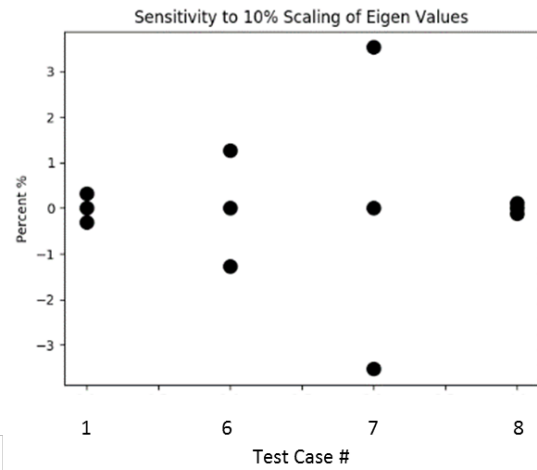
Figure 3.6: Variation in Eigenvalues.
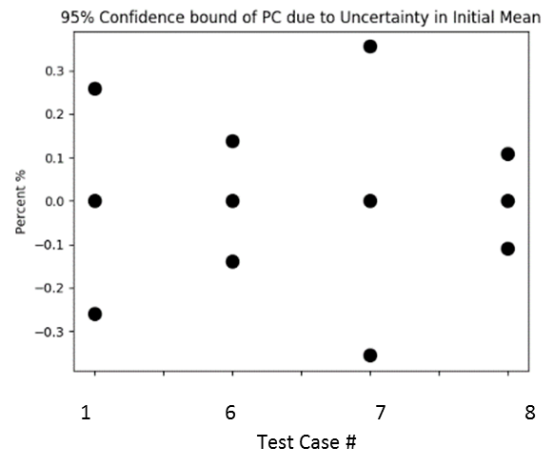
Figure 3.7: Variation in Mean.

As can be seen in the figures, small variations in the mean and covariance did not lead to large changes in the computed P_c for these four test cases. With P_c variations remaining below $\pm 4\%$ of the nominal value. While there are cases where small changes in the initial conditions can lead to large changes in the computed P_c, it is important to ascertain the likelihood of these events if possible.

The developments leading to Figures 3.6 and 3.7 represent an important first step in a process that can increase confidence in P_c computation. In principle only parametric model and distribution uncertainty can be treated in a similar fashion to assess the sensitivity of the computed P_c to model errors and errors in the reported distributions.

3.4 Conclusions

In most of the test cases, there was not an appreciable difference seen in the predicted results using the various methods. That said, the GMM was slightly more accurate on most test cases.

This is contrasted by test cases II, VI, and VII where the collision was designed such that linear approximations would result in either an over or under prediction of the P_c. In these cases LG and GMM solutions were seen to agree more closely with the MC results. Since these types of collisions can occur under a number of scenarios, CRATER only adaptively selects to use the SG solution when the true distribution is determined to be sufficiently Gaussian by use of of the non-linearity index.

The LG approximation were shown to offer a significant step of realism over the SG approach, when nonlinear effects were significant, while maintaining much of the computational efficiency. This approximation scheme works particularly well when the R_c is small compared to the valid domain of the LG and when the colliding satellites have a high relative inclination to each other. In cases where there is a low relative inclination, it is possible that the PDFs intersect in such a way that the intersection region spans the domains of several LGs. This case traditionally calls for the use of a GMM, however if care is taken during the integration phase, LGs could be a more efficient alternative to GMM in these collision scenarios as well.

Error in the propagated PDF clearly has the strongest correlation with the fidelity of the predicted results, as demonstrated by test cases IV, and V. Both of these cases had high propagation error and consequently had the largest discrepancies of any of the test cases with respect to their corresponding Monte Carlo results. Quantifying the error with respect to the Liouville equation has shown that the most restrictive of the assumptions imposed on the test cases was the assumption that the PDF remains Gaussian in orbital element space. It was seen that the error in this assumption was most severe along the eigenfiber of the covariance ellipsoid. Since this error is largely restricted to a single axis, it is a simple matter adapt the LG or GMM generation techniques used in CRATER to fit the true PDF along this axis. This way, CRATER would use the same LG and GMM approximation techniques to handle the nonlinear transformation of the PDF, in orbital element space, through time as it does when mapping the propagated PDF from orbital elements to Cartesian coordinates.

Finally, the ability to consider uncertain force model parameters was added to the CRATER

algorithm. It was shown that under the given assumptions, the uncertain force parameters only affect the propagation of the PDF and not the process used to compute the final P_c integral. While accounting for uncertain force model parameters did not affect the form of the P_c integral, accounting for them did correctly affect the computed P_c by orders of magnitude as seen in test cases IV, V, and VIII. This is because uncertainty in the force model parameters affects the evolution of the covariance matrix over time, causing it to become significantly changed with respect to a covariance matrix that was propagated without taking model uncertainty into account. This is in agreement with the results reported in [122], which investigated the effects scaling the covariance matrix had on the computed P_c and similarly found that the P_c could vary by orders of magnitude as a result of simply scaling the covariance matrix.

In Summary, the CRATER algorithm has sought to combine the best elements of [96, 72, 74] while adding some important features. These key features are summarized as:

- Quantifying the error in the propagated PDF with respect to the Liouville Equation

- Adaptive local Gaussian approximations and algorithm selection based on the non Gaussianity / linearity of the problem

- Accounting for force model uncertainty

- Adaptive construction of GMM based on the errors in the Gaussian assumption

- Use of the full nonlinear dynamics to allow long term encounters when velocities are not constant over the collision event

When operating within the bounds of its assumptions, CRATER is able to accurately predict the probability of collision while appropriately adapting to the collision under analysis to reach an amicable union of accuracy, adaptability, and computational performance.

4. RELATIVE ORBITAL ELEMENTS [*]

4.1 Introduction

The satellite probability of collision problem is an important part of space situational aware-ness (SSA) and risk analysis for space based assets. Efficient computation of the probability of collision (P_c) is highly dependent on Gaussian initial conditions, linear dynamics and linear coor-dinate transformations. Many early efforts on this problem relied heavily on these assumptions and focused primarily on developing efficient 2D methods [76, 84, 85, 87, 88, 89]. Since then more emphasis has been placed on higher fidelity analysis that makes use of full state uncertainty and relaxes the dependence on Gaussian and linearizing assumptions [96, 72, 64, 74, 98, 73, 100].

Most of these methods however, rely on evaluating the P_c integral in Cartesian coordinates. Since uncertainty is usually propagated in the more linear orbital element space, evaluation of the P_c integral will necessitate a nonlinear coordinate transformation into Cartesian coordinates. When assessing the non-linearity of the problem [42], previous work (see Chapter 3) suggests that one of the most nonlinear parts of the P_c problem is this mapping of the propagated distribution from orbital element space into Cartesian coordinates. This nonlinear mapping is typically addressed by projecting the distribution onto a set of basis functions [135, 136]. This approach is able to capture the nonlinear effects on the transformed distribution, but can require a large number of basis functions. The present work seeks to address this nonlinear portion of the probability of collision problem by deriving the P_c integral in terms of relative orbital elements. This will extend the range over which local Gaussian approximations (introduced in Chapter 3) are valid and reduce the number of mixture components needed, if using a Gaussian mixture to represent the distribution at the time of integration.

Throughout this chapter there will be frequent mention of the eigenfiber and nonlinearity (NL) index. These concepts are presented in greater context in Chapter 3 and in [42, 98], but key

---

elements are reproduced here to facilitate the discussion of this chapter. If the initial PDF is taken to be Gaussian in orbital element space then before long, and regardless of the initial distribution, the eigenvector of the covariance matrix that points along the true anomaly direction will become the largest principle axis of the element space covariance ellipsoid. When, centered at the nominal trajectory, this straight vector in orbital element space is mapped into Cartesian coordinates it becomes, to a high degree of fidelity, the center line of the banana shaped distribution. For ease of reference we call this space curve the eigenfiber.

The NL index was developed and investigated extensively in [42] as an answer to the question, "How nonlinear is it?", referring to a given dynamic or static nonlinear mapping. In the context of P_c analysis the NL index is used primarily to quantify the nonlinearity of coordinate changes, but is also used to quantify the nonlinearity of the dynamics as well. If we define the nonlinear algebraic one-to-one coordinate transformation from classical orbital elements ($\boldsymbol{q}$) to Cartesian coordinates ($\boldsymbol{X}$) as $\boldsymbol{X} = f(\boldsymbol{q})$, then the Jacobian $J(\boldsymbol{q}) = \frac{\partial f}{\partial \boldsymbol{q}}$ is easily evaluated at any $\boldsymbol{q}_i$. The NL index (η) is then defined as

$$\eta_{ij} = \frac{||J(\boldsymbol{q}_j) - J(\boldsymbol{q}_i)||_2}{||J(\boldsymbol{q}_i)||_2} \tag{4.1}$$

where $|| \cdot ||_2$ is the 2 norm. Hence, the NL index is essentially the relative change in the first derivatives of the mapping $f(\boldsymbol{q})$ along the vector $\boldsymbol{q}_j - \boldsymbol{q}_i$. If $\boldsymbol{q}_i$ is taken as the nominal or center-point of the orbital element distribution then $\boldsymbol{q}_j$ can be taken along each eigenvector. This is used to estimate the neighborhood over which a first order Taylor series approximation of $f(\boldsymbol{q})$ is valid and identify any quasi-linear sub-spaces in the mapping.

4.2   Methods

Consider a possible collision between two satellites S_1 and S_2. The initial conditions of these satellites are given as Gaussian distributions in orbital element space with respective means $\bar{\boldsymbol{q}}_{1_0}$ and $\bar{\boldsymbol{q}}_{2_0}$ and covariances Q_{1_0} and Q_{2_0}. For the ease of discussion, let us suppose these means and covariances are given in terms of the Kepler orbital elements [137]. The motion of the satellites is then fully characterized by the orbital elements $\{a_j, e_j, i_j, \omega_j, \Omega_j, \nu_j\}$, $j = 1, 2$. Note that the

elements $\{a, e, \nu\}$ fully describe the planar motion of a satellite in the perifocal orbital reference frame (hereafter the perifocal frame), while the orientation of that frame is given by the 3-1-3 rotation through the angles $\{\Omega, i, \omega\}$. Let R_1 and R_2 be the 3-1-3 rotation matrices from the inertial frame to the perifocal frames of S_1 and S_2 respectively. Then a vector can be mapped from the S_2 into the S_1 perifocal frame through the composite rotation $R_1 R_2^T$.

At this point, we would like to describe the motion of S_2 with respect to the perifocal frame of S_1. As before $\{a_2, e_2, \nu_2\}$ describe the planar motion of S_2, we then need to define a set of relative orbital elements $\{\Omega_r, i_r, \omega_r\}$ that give the orientation of the S_2 perifocal frame, in terms of a 3-1-3 rotation R_r, with respect to the S_1 perifocal frame. It is clear that $R_r = R_2 R_1^T$. Since R_r is a 3-1-3 rotation the elements Ω_r, i_r, ω_r can be expressed in terms of the elements of the matrix $R_{r_{i,j}}$ by noting

$$
\begin{aligned}
\cos i_r &= R_{r_{3,3}} \\
\tan \omega_r &= \frac{R_{r_{1,3}}}{R_{r_{2,3}}} \\
\tan \Omega_r &= \frac{R_{r_{3,1}}}{-R_{r_{3,2}}}
\end{aligned}
\tag{4.2}
$$

If we then express R_r in terms of the orbital elements of S_1 and S_2, the following relations are obtained.

$$
\begin{aligned}
\cos i_r &= \sin i_1 \sin i_2 \cos (\Omega_2 - \Omega_i) + \cos i_1 \cos i_2 \\
\tan \Omega_r &= \frac{\mathcal{S}_{i_2}(\mathcal{C}_{\omega_1}\mathcal{S}_{\Omega_2 - \Omega_1} - \mathcal{C}_{i_1}\mathcal{S}_{\omega_1}\mathcal{C}_{\Omega_2 - \Omega_1}) + \mathcal{C}_{i_2}\mathcal{S}_{i_1}\mathcal{S}_{\omega_1}}{\mathcal{S}_{i_2}(\mathcal{S}_{\omega_1}\mathcal{S}_{\Omega_2 - \Omega_1} + \mathcal{C}_{i_1}\mathcal{C}_{\omega_1}\mathcal{C}_{\Omega_2 - \Omega_1}) - \mathcal{C}_{i_2}\mathcal{S}_{i_1}\mathcal{C}_{\omega_1}} \\
\tan \omega_r &= \frac{-\mathcal{S}_{i_1}(\mathcal{C}_{\omega_2}\mathcal{S}_{\Omega_2 - \Omega_1} + \mathcal{C}_{i_2}\mathcal{S}_{\omega_2}\mathcal{C}_{\Omega_2 - \Omega_1}) + \mathcal{C}_{i_1}\mathcal{S}_{i_2}\mathcal{S}_{\omega_2}}{\mathcal{S}_{i_1}(\mathcal{S}_{\omega_2}\mathcal{S}_{\Omega_2 - \Omega_1} - \mathcal{C}_{i_2}\mathcal{C}_{\omega_2}\mathcal{C}_{\Omega_2 - \Omega_1}) + \mathcal{C}_{i_1}\mathcal{S}_{i_2}\mathcal{C}_{\omega_2}}
\end{aligned}
\tag{4.3}
$$

where $\mathcal{S}_\theta = \sin(\theta)$ and $\mathcal{C}_\theta = \cos(\theta)$.

As expected i_r is the angle between the two angular momentum vectors $\boldsymbol{h}_1$ and $\boldsymbol{h}_2$, Ω_r is the angle between the eccentricity vector of S_1 and the vector $\boldsymbol{h}_1 \times \boldsymbol{h}_2$, and ω_r is the angle between
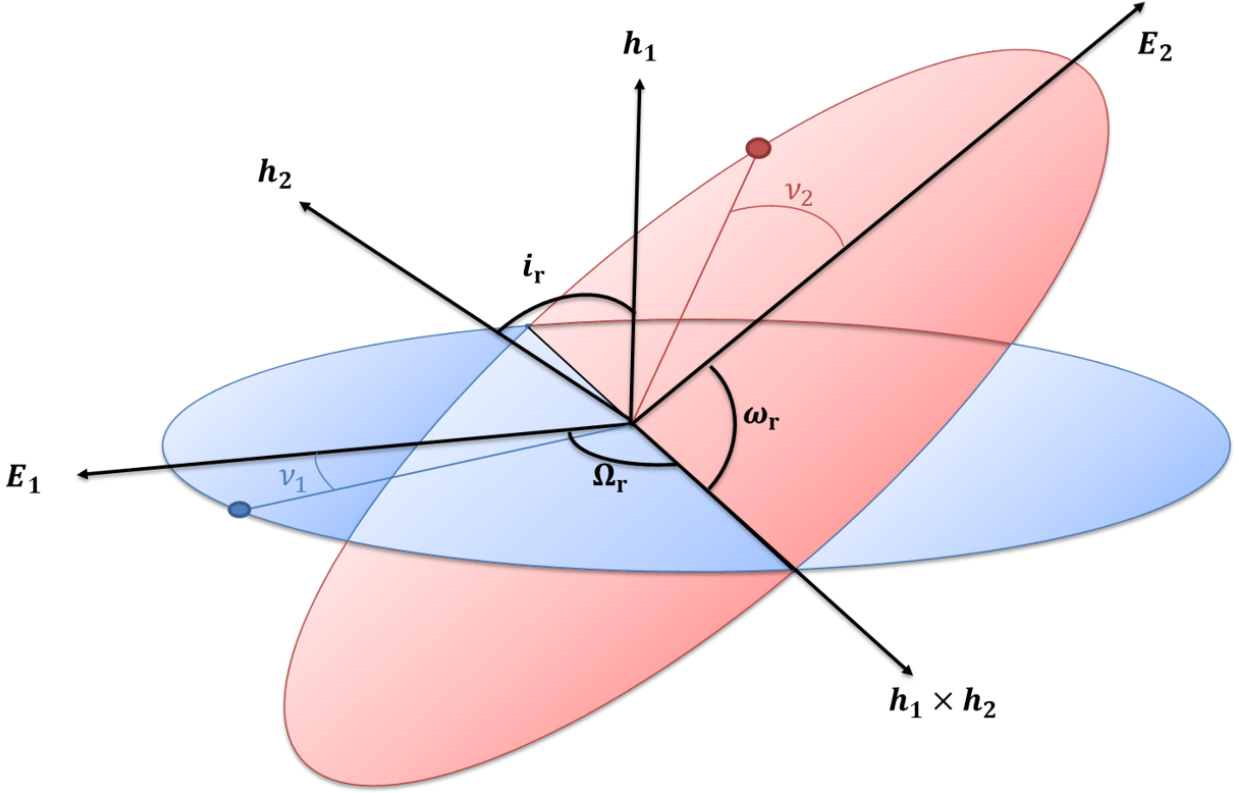
Figure 4.1: Relative Orbit Geometry. Reprinted with permission from [103].

the eccentricity vector of S_2 and $\boldsymbol{h}_1 \times \boldsymbol{h}_2$, as shown in Figure 4.1. Defining the relative orbital elements in this way will of course be problematic for cases where either orbit has zero inclination, zero eccentricity, or are co-planar. The developments are presented for the classical elements, because of the ease of visualization. The analogous process though is easily carried out for other element sets which can mitigate these singularities, and is done for the modified equinoctial elements in Appendix C. These relative orbital elements are related, but distinct from those often used in relative satellite motion applications [138, 139, 140].

With the relative geometry defined and the relations given by equation (4.3), the state of the system can be redefined as a twelve element set with the last three being the relative elements

$$\boldsymbol{P} = [\{a_1, e_1, \nu_1\}\{i_1, \omega_1, \Omega_1\}\{a_2, e_2, \nu_2\}\{i_r, \omega_r, \Omega_r\}]^T \qquad (4.4)$$

Since the relative elements $\{i_r, \omega_r, \Omega_r\}$ are functions of both $\boldsymbol{q}_1$ and $\boldsymbol{q}_2$, it may be preferable to propagate the state and PDF in terms of $\boldsymbol{q}_1$ and $\boldsymbol{q}_2$ and then map the distribution into terms of the 12 elements of $\boldsymbol{P}$ for analysis. The primary motivation for defining the state of the system this way is to avoid the need to convert to Cartesian coordinates when it comes time to evaluate the P_c integral. The details of this are presented in the Planar Conjunction Analysis section.

4.2.1 Collision Prefiltering

Before moving on to the probability of collision calculations, let us first consider some of the insights that can be gained from examining Figure 4.1. One aspect of conjunction analysis is the prefiltering stage. The crux of this part of problem lies in quickly finding pairs of satellites that may potentially collide within some screening window while screening out satellite pairs that do not warrant a full P_c analysis. For example, one of the coarsest filters on collisions is to compare the radius of perigee of one orbit with the radius of apogee of the other orbit and see if there is a possible overlap. Should two orbits pass this filter, we then need to take a closer look to see if a P_c analysis is necessary. A number of Geometric conditions exist for doing this type of analysis and have been explored in [77] and have been used by agencies such as NORAD to find and issue conjunction warnings. One issue of only using geometric filters is that it generally relies on heuristic processes and bounds to decide what defines a close approach and how close two objects need to be before the pair is considered for a probability of collision analysis. By incorporating the information from the initial distributions and the radius of collision a more probabilistic definition of close approach can be formed and lend some formality to establish a probabilistic means of prefiltering without the need to numerically propagate the orbit or the distributions in time.

It is obvious from the geometry in Figure 4.1 that collisions will only occur within a small neighborhood of the relative line of nodes that lies along the instantaneous vector $\boldsymbol{h}_1 \times \boldsymbol{h}_2$, with the exception of orbits that are, or nearly are, coplanar. We can then filter out improbable collisions, for a large class of collision scenarios, by comparing $r_1(a_1, e_1, \nu_1 = \{\Omega_r, \Omega_r \pm \pi\})$ and $r_2(a_2, e_2, \nu_2 = \{-\omega_r, -\omega_r \pm \pi\})$ by projecting the initial distribution in $\{\boldsymbol{q}_1, \boldsymbol{q}_2\}$ onto Δr along this direction. This will allow us to answer the question: "What is the probability that the two orbits come within

a radius of collision (R_c) of each other?". This probability must be computed for two cases, the ascending node $\nu_1 = \Omega_r$, $\nu_2 = -\omega_r$, and descending node $\nu_1 = \Omega_r + \pi$, $\nu_2 = \pi - \omega_r$.

The mean of this distribution can be defined as $\Delta\bar{r} = \bar{r}_2 - \bar{r}_1$, where $\bar{r}_i \approx r(\bar{a}_i, \bar{e}_i, \bar{\nu}^*_i = 0, \pi)$ and

$$
\begin{aligned}
\nu_1^* &= \nu_1 - \Omega_r \\
\nu_2^* &= \nu_2 + \omega_r
\end{aligned}
\tag{4.5}
$$

Next the variance in Δr can be obtained through a similarity covariance mapping

$$
\sigma_{\Delta r}^2 \approx \frac{d\Delta r}{d\boldsymbol{P}} Q_{P_0} \frac{d\Delta r}{d\boldsymbol{P}}^T
\tag{4.6}
$$

Where $\frac{d\Delta r}{d\boldsymbol{P}}$ is the 1×12 gradient of Δr evaluated at $\bar{a}_i, \bar{e}_i, \bar{\nu}^*_i = 0, \pi$. When mapping the 12×12 covariance into $\sigma_{\Delta r}^2$ note that we do not map any initial uncertainty in ν_1 or ν_2 into Δr, since these angles are given. Instead uncertainty in the relative angles Ω_r and ω_r are mapped into $\sigma_{\Delta r}^2$. Alternatively, it is a simple matter to use nonlinear mapping techniques to acquire $\Delta\bar{r}, \sigma_{\Delta r}$, or even a non-Gaussian probability distribution for Δr.

Now suppose we are considering the ascending node case $\nu_1 = \Omega_r, \nu_2 = -\omega_r$. The probability that the two orbits come within R_c of each other (P_c^*), or equivalently the probability of a collision between two satellites given $\nu_1 = \Omega_r, \nu_2 = -\omega_r$ is then

$$
\begin{aligned}
P_c^* = P(\Delta r \leq R_c | \nu_1 = \Omega_r, \nu_2 = -\omega_r) &= \int_{-R_c}^{R_c} N(\Delta r, \Delta\bar{r}, \sigma_r) d\Delta r \\
P_c^* &= \frac{1}{2}\left\{ erf\left(\frac{\Delta\bar{r} + R_c}{\sigma_r\sqrt{2}}\right) - erf\left(\frac{\Delta\bar{r} - R_c}{\sigma_r\sqrt{2}}\right)\right\}
\end{aligned}
\tag{4.7}
$$

If $P_c^* \leq \epsilon$ for both the ascending and descending nodes, where ϵ is a desired tolerance, then the two orbits in question may be considered non-colliding. It is important to recognize that P_c^* is an upper bound to the probability of collision, and not the probability of collision itself, since it is conditioned on the event that both satellites are exactly on the line of relative nodes. Furthermore,

this analysis is linear, and Keplerian, as such, $\sigma_{\Delta r}^2$ may not be sufficient to characterized the distribution if the initial uncertainty is too large to accurately map linearly. Additionally, perturbations will cause ω_r and Ω_r to process with time. To account for this effect one can easily compute the mean procession rates for $\omega_1, \omega_2, \Omega_1, \Omega_2$ due to a J2 gravity model [141, 142, 143]. The mean procession rates for the relative orbital elements ω_r, Ω_r is then

$$\dot{\Omega}_r = \frac{\partial \Omega_r}{\partial \Omega_1}\dot{\Omega}_1 + \frac{\partial \Omega_r}{\partial \omega_1}\dot{\omega}_1 + \frac{\partial \Omega_r}{\partial \Omega_2}\dot{\Omega}_2 + \frac{\partial \Omega_r}{\partial \omega_2}\dot{\omega}_2 \tag{4.8}$$

$$\dot{\omega}_r = \frac{\partial \omega_r}{\partial \Omega_1}\dot{\Omega}_1 + \frac{\partial \omega_r}{\partial \omega_1}\dot{\omega}_1 + \frac{\partial \omega_r}{\partial \Omega_2}\dot{\Omega}_2 + \frac{\partial \omega_r}{\partial \omega_2}\dot{\omega}_2 \tag{4.9}$$

Even taking into account the mean procession rate, this analysis is meant to filter out unlikely conjunctions that may occur within a moderate analysis window.

Another useful quantity to consider is the phase angle between the two satellites. If we define a phase angle ϕ.

$$\phi = (\nu_2 + \omega_r) - (\nu_1 - \Omega_r) = (\nu_2 - \nu_1) + (\omega_r + \Omega_r) \tag{4.10}$$

and for Keplerian motion

$$\dot{\phi} = \dot{\nu}_2 - \dot{\nu}_1 \tag{4.11}$$

If we express the phase angle and rate in terms of the mean anomalies we get

$$\phi^* = (M_2 - M_1) + (\Omega_r^* + \omega_r^*)$$
$$\dot{\phi}^* = n_2 - n_1 = \sqrt{\mu}(a_2^{-\frac{3}{2}} - a_1^{-\frac{3}{2}}) \tag{4.12}$$

Dividing this rate by 2π yields the mean beat frequency of collisions between the two satellites, or divide by 2 if there are two collisions possible per period, and the mean period between possible collisions for satellites in circular or near circular orbits is then given by $\bar{T}_{col}$.

$$\bar{T}_{col} = \frac{2\pi}{n_2 - n_1} \tag{4.13}$$

This quantity can then be used to estimate how many close encounters to anticipate in a given analysis window.

In particular, for collisions, one is interested in the phase angle as one of the satellites passes through the orbital plane of the other. If the quantity $P_c^* \leq \epsilon$, on either the ascending or descending node, we do not need to concern ourselves with the phase angle at that node. Suppose for a given pair of satellites that P_c^* is significant only for the ascending node. For this example, let satellite S_1 be the reference orbit, thus we are looking at the phase angle ϕ as S_2 passes through the relative ascending node $\nu_2^* = 0$. If the period of S_2 is T_2 and has a time till first nodal crossing of t_{nc} (which we find using the Kepler solution) then the times of the future nodal crossings is simply

$$T_{nc_i} = i * T_2 + t_{nc}, \quad i = 0, 1, 2, ...$$

At this point we would like to quantify, in a statistical sense, the distance between S_1 and S_2. To do this we find the initial change in the semi major axis Δa_0 such that $0 = \nu_1^*(T_{nc_i})$ As this is a prefiltering method, and the semi-analytical methods for computing the P_c presented later in this paper take little longer than numerically propagating the orbit, we shall use either the Kepler solution, or a low order zonal only gravity model to find Δa_0. Proceeding with the Kepler solution, we can analytically find Δa_0, by transforming Ω_r into a mean anomaly angle M_{Ω_r} and solving

$$M_{\Omega_r} + i * 2\pi = \sqrt{\frac{\mu}{(\bar{a}_0 + \Delta a_0)^3}}(T_{nc_i} - T_0) + M_0 \tag{4.14}$$

for Δa_0. We can now compute the minimum Mahalanobis distance [144] between S_1 and S_2 in terms of the initial Gaussian distributions. Recall $\boldsymbol{q}_{2_0}$ had a covariance of Q_{2_0}. Let $Q_{2_0} = \begin{bmatrix} A & B^T \\ B & C \end{bmatrix}$. The minimum Mahalonobis distance (D_m) is then

$$D_m^2 = [\Delta a_0, \boldsymbol{\xi}^T]Q_{2_0}^{-1}\begin{bmatrix} \Delta a_0 \\ \boldsymbol{\xi} \end{bmatrix} \tag{4.15}$$

where $\boldsymbol{\xi} = -C^{-1}B\Delta a_0$

Should this distance remain large for all nodal crossings, then a collision will be of negligible probability. Additionally plugging in $\pm 6\sigma$ values for Δa_0 into (4.14) and solving for T will give the approximate limits of integration for the time integral when it comes time to compute the P_c.

4.2.2 Planar Conjunction Analysis

Let us resume our consideration of the possible collision between satellites S_1 and S_2. To simplify our analysis, we shall first explore the case where the orbits of the two satellites have a high relative inclination and the distributions are either Gaussian, locally Gaussian, or given by a GMM. At each time t we map the state and distribution from the inertial orbital elements $\bar{q}_1(t), \bar{q}_2(t), Q_1(t), Q_2(t)$ into the relative orbital elements $\bar{\boldsymbol{P}}(t), Q_p(t)$. Since $\{\Omega_r, i_r, \omega_r\}$ describe the relative orientation of the two orbital planes, we can take the orbital plane of S_1 as fixed with uncertainty in the orientation of the plane of S_2 with respect to S_1. It is clear then that any collision will occur within $\pm R_c$ of the orbital plane of S_1. For high relative inclinations and all but the most extreme values of R_c we can limit our analysis to collisions on the orbital plane of S_1 without an appreciable affect on the computed P_c. In this case we assume S_2 trajectories only cross the orbital plane of S_1 once at a unique $\tau \in (t_0, t_f]$. We use this assumption to define the collision event set Λ_τ.

$$\Lambda_\tau := \{\boldsymbol{P}(t) |\ \rho(t) \leq R_c\ \text{at time}\ t = \tau\} \tag{4.16}$$

for some $\tau \in (t_0, t_f]$ and where $\rho(t)$ is the Euclidean distance between S_1 and S_2. That is Λ_τ will simply be the subset of the states on the orbital plane of S_1 at time $t = \tau$ (or equivalently for which $\nu_2^* = 0, \pi$) that satisfy the collision criteria $\rho(t) \leq R_c$. The union of all Λ_τ then would be the set of all $\boldsymbol{P}$ that resulted in a collision anytime between t_0 and t_f. In terms of the set Λ_τ the P_c can then be defined as

$$P_c = \int_{t_0}^{t_f} \int_{\Lambda_\tau} f_p(\boldsymbol{P}(t), t; t_0) d\boldsymbol{P} \tag{4.17}$$

81

For our planar analysis, a state $\boldsymbol{P}$ can be said to belong to the set Λ_τ if and only if

$$\nu_2^* = 0, \pi$$

$$R_c^2 \geq \Delta r^2 + (\bar{r}_2^* \nu_1^*)^2$$

(4.18)

Where $\bar{r}_2^*$ is the r corresponding to the orbital element state $\boldsymbol{q}_2(\tau)$ along the eigenfiber of the S_2 distribution that intersects the S_1 plane at time $t = \tau$. That is

$$\boldsymbol{q}_2(\tau) = \bar{\boldsymbol{q}}_2(t) - \frac{\bar{\nu}_2^*(t)}{\lambda_\nu} \boldsymbol{E}_\nu$$

(4.19)

where $\boldsymbol{E}_\nu$ is the eigenfiber with an eigenvalue of λ_ν As with other planar P_c formulations, the velocity does not explicitly enter into the conditions for a collision. From these conditions we can define limits of integration over $\{\Delta r, \nu_1^*\}$.

$$|\Delta r| \leq \sqrt{R_c^2 - (\bar{r}_2^* \nu_1^*)^2}$$

$$\Rightarrow |\nu_1^*| \leq \frac{R_c}{\bar{r}_2^*}$$

(4.20)

Integrating over the limits in (4.20) would produce the probability of a collision given $\nu_2^* = 0, \pi$. From the law of total probability, it is clear that to get the probability of collision we must include the probability density of the event that $\nu_2^* = 0, \pi$ at time $t = \tau$ and integrate over all such events. This integration will be made easier by noting that the differential $d\nu_2^*$ can be written as the following.

$$d\nu_2^* = \frac{d\nu_2^*}{dt} dt$$

(4.21)

To evaluate the integral in (4.17), we shall employ a change of variables from relative orbital elements to relative polar coordinates $\boldsymbol{\chi} = [\Delta r, \nu_1^*, \nu_2^*]^T$. Since the relative orbital elements are functions of $\boldsymbol{q}_1$ and $\boldsymbol{q}_2$ it is easier to form the distribution in $\boldsymbol{\chi}$ directly from the distribution in $\boldsymbol{P}$ as opposed to forming a distribution in $\{r_1, \theta_1\}$, $\{r_2, \theta_2\}$ and then forming the relative distribution as is done in [96]. After mapping the PDF into the relative polar coordinates and bringing in the

limits of integration from (4.20), the P_c is given by the following expression.

$$P_c = \int_{t_0}^{t_f} \int_{-R_c/\bar{r}_2^*}^{R_c/\bar{r}_2^*} \int_{-\sqrt{R_c^2-(\bar{r}_2^*\nu_1^*)^2}}^{+\sqrt{R_c^2-(\bar{r}_2^*\nu_1^*)^2}} f_\chi(\boldsymbol{\chi}(t),t;t_0)|\dot{\nu}_2^*| \ d\Delta r \ d\nu_1^* \ dt \tag{4.22}$$

If the PDF in $\boldsymbol{\chi}$ can be expressed in terms of a Gaussian and if the motion of $\boldsymbol{q_1}$ is independent of $\boldsymbol{q_2}$, then equation (4.22) can be reduced to

$$P_c = \int_{t_0}^{t_f} \int_{-R_c/\bar{r}_2^*}^{R_c/\bar{r}_2^*} \int_{-\sqrt{R_c^2-(\bar{r}_2^*\nu_1^*)^2}}^{+\sqrt{R_c^2-(\bar{r}_2^*\nu_1^*)^2}} N(\boldsymbol{\chi},\boldsymbol{\mu}_\chi,Q_\chi)|\dot{\nu}_2^*| \ d\Delta r \ d\nu_1^* \ dt \tag{4.23}$$

4.2.3 3D Analysis

For a number of collision scenarios it is necessary to do a 3D P_c analysis that takes into account the full state uncertainty. Several algorithms [72, 74, 98] have been developed, as an alternative to Monte Carlo, based on [96], which have this capability. The efficiency of these methods is highly dependent on the underlying distributions, in the frame which the P_c integral is to be evaluated, being Gaussian or a GMM with a moderate number of mixture components at the time of collision. This can be partially achieved by formulating the PDF in spherical coordinates as opposed to Cartesian.

Unfortunately spherical coordinates have singularity issues with the azimuth angle and rate, when objects are located along the $\hat{z}$ axis. To avoid this difficulty the x-y-z axes of the spherical coordinate system will be aligned with the nominal perifocal frame axes of satellite S1. This ensures that all collision events occur near the x-y plane. As usual θ measures the angle from the the $\hat{x}$ axis to the projection of the of the position vector onto the x-y plane and ϕ is the angle from the $\hat{z}$ axis. With this definition of coordinate axis, the spherical coordinates in terms of the orbital elements is.

$$r = \frac{a(1 - e^2)}{1 + e \cos \nu}$$

$$\theta = \arctan\left(\frac{R_{r_{2,1}} \cos \nu + R_{r_{2,2}} \sin \nu}{R_{r_{1,1}} \cos \nu + R_{r_{1,2}} \sin \nu}\right)$$

$$\phi = \arccos\left(R_{r_{3,1}} \cos \nu + R_{r_{3,2}} \sin \nu\right)$$

$$\dot{r} = \frac{\mu}{h} e \sin \nu \tag{4.24}$$

$$\dot{\theta} = \frac{h}{r^2} \frac{R_{r_{3,3}}}{\sin \phi^2}$$

$$\dot{\phi} = \frac{h}{r^2}(R_{r_{2,3}} \cos \theta - R_{r_{1,3}} \sin \theta)$$

where $R_r \in \mathcal{R}^{3\times3}$ is the rotation matrix from the S_2 perifocal frame to the S_1 perifocal frame. Since we are often concerned with collisions between objects in circular or nearly circular orbits, equation (4.24) is given in terms of the modified equinoctial elements in Appendix C.

A Taylor series expansion of equation (4.24) at the point where the Eigen fiber of the distribution crosses the line of relative nodes, will allow us to linearly map the distribution into the spherical coordinates. As was the case in [96] we are concerned with finding the probability of the relative position being on the surface of a sphere, of radius R_c with relative velocities entering the sphere, at discrete times $t_i \in (t_0, t_f]$ and then integrating over all t_i. The PDF of the relative state is formed in the same way it is in [96], such that the mean (μ_r) and covariance (Σ_r) of the relative state distribution (in spherical coordinates) are given by the relations below.

$$\mu_r = \mu_2 - \mu_1 \tag{4.25}$$

$$\Sigma_r = \Sigma_1 + \Sigma_2 \tag{4.26}$$

At this point in the discussion it is useful to summarize how all of the pieces come together to compute a P_c value (please see Algorithm 1).

A quick note on Algorithm 1 step 13, in going from the Cartesian integral to an earth centered

---
Algorithm 1: CRATER
---

1 <u>function CRATER</u> $(q_{S_1}, q_{S_2}, Q_{S_1}, Q_{S_2}, t_0, t_{c_0}, t_{c_f})$;

   Input : Initial means and covariances in orbital elements q_i and Q_i along with inial time t_0 start of screening window t_{c_0} and end of screening window t_{c_f}

   Output: P_c

2 Linearly Propagate the nominal trajectories q_{1n}, q_{2n} and covariances Q_{1n}, Q_{2n} from t_0 to t_{c_0}

3 Compute the non linearity index of the STM along the Eigen fiber, find $\Delta\sigma$ such that $\frac{||\Phi_i - \Phi_n||_2}{||\Phi_n||_2} \le \epsilon$, where Φ_i is the STM linearized about $q_i = q_n + \Delta\sigma \boldsymbol{E}_{\nu_n}$ (where $\boldsymbol{E}_{\nu_n}$ is the Eigenfiber computed at the mean)

4 Place $N = \frac{12\sigma}{\Delta\sigma}$ linearization points $\boldsymbol{q}_i$ along the axis of the initial distributions corresponding to uncertainty in the semi major axis of the orbit

5 Propagate each $\boldsymbol{q}_i$ and STM Φ_i linearized about $\boldsymbol{q}_i$ all the way through t_{c_f}

6 **for** *each time* $t_j \in [t_{c_0}, t_{c_f}]$ **do**

7 | Find the $\boldsymbol{q}_i$ that is closest to the relative line of nodes by computing ω_r, Ω_r, let this be called $\boldsymbol{q}_{ij}$

8 | Then find the states $\boldsymbol{q}_1^*, \boldsymbol{q}_2^*$ such that $\{\nu_1^*, \nu_2^*\} = 0$ *or* π where $\boldsymbol{q}_k^* = \boldsymbol{q}_{ij_k} + \Delta\sigma_k \boldsymbol{E}_{\nu_{i_k}}$ where $\boldsymbol{E}_{\nu_{i_k}}$ is the Eigen fiber of $\Phi_i Q_k \Phi_i^T$, $k = 1, 2$.

9 | Compute the linearized transformation from orbital elements to spherical coordinates M_1, M_2 about the vectors q_1^*, q_2^*. We can now express the displacement from the mean to a given state $\boldsymbol{s}$ (in spherical coordinates) in terms of the orbital elements at t_0 (in the neighborhood of our expansion point) as

$$\Delta\boldsymbol{q}_{0_k} = \boldsymbol{q}_{0_k} - \bar{\boldsymbol{q}}_{0_k} = \Phi_{i_k}^{-1} M_k^{-1}(\boldsymbol{s} - \boldsymbol{s}_k^*) + \Phi_{i_k}^{-1}(\boldsymbol{q}_k^* - \boldsymbol{q}_{ij_k}) + (\boldsymbol{q}_{i0_k} - \bar{\boldsymbol{q}}_{0k}) \qquad (4.27)$$

10 | Compute the mean of the relative distribution in spherical coordinates $\mu_r = \mu_2 - \mu_1$ where $\mu_k = \boldsymbol{s}_k^* - M_k(\boldsymbol{q}_k^* - \boldsymbol{q}_{ij_k}) - M_k \Phi_{i_k}(\boldsymbol{q}_{i0_k} - \bar{\boldsymbol{q}}_{0k})$

11 | Compute the covariance of the relative distribution $\Sigma_r = \Sigma_1 + \Sigma_2$ where $\Sigma_k = M_k \Phi_{i_k} Q_k \Phi_{i_k}^T M_k^T$, $k = 1, 2$

12 | Let $\Sigma_r = \begin{bmatrix} A_r & B_r \\ B_r^T & C_r \end{bmatrix}$

13 | And, as in [96], except now in terms of relative spherical coordinates, evaluate $P_{c_j} = \int_0^{2\pi} \int_{-\pi/2}^{+\pi/2} N(\boldsymbol{s}_r, \boldsymbol{\mu}_r, A_r)\nu(\hat{\boldsymbol{s}}, t) R_c^2 \cos\gamma \ d\gamma \ d\psi$

14 **end**

15 return $P_c = \int_{t_{c0}}^{t_{c_f}} P_{c_j} dt$

85

spherical coordinate system we pick up an $\frac{d\boldsymbol{X}}{d\boldsymbol{s}_E} = R^2 \sin\phi$. Then if we wish to evaluate the the integral in terms of a body centered spherical frame, as in [96], we pick up a factor of $\frac{d\boldsymbol{s}_E}{d\boldsymbol{s}_B} = \frac{R_c^2}{R^2}\cos\gamma$. Noting that $\sin\phi \approx 1$ we end up with the approximation $dv = R_c^2 \cos\gamma d\gamma \; d\psi$ where γ is the elevation angle.

The reader has likely noticed that many of these methods rely heavily on the line of relative nodes and may face some difficulty when the two colliding objects are in co-planar or nearly co-planar orbits. These methods however, are still valid over a large portion of practical collision scenarios. Instances where these techniques may break down are easily identified beforehand by computing i_r.

4.3 Results

The 2D and 3D formulations of the P_c from the Planar and 3D Analysis sections were incorporated into the CRATER collision risk assessment tool and then used to compute the P_c on select test cases from Chapter 3. These results are compared to the classical implementation of CRATER, which uses the P_c integral derived by Coppola [96] with local Gaussian and GMM enhancements. The only thing that changes between these two methods then is the coordinate system in which the P_c integral is evaluated, giving a comparison between the Cartesian and the relative orbital element formulations. We shall see two sets of comparison results; one for the classical linear analysis, where no local Gaussian or GMM are used to compensate for the nonlinearity in the problem, and the other set where local Gaussians are used.

Table 4.1: CRATER Results Cartesian Vs. Relative OE Linear Analysis. Reprinted with permission from [103].

Test Case II	Cart.	2D Rel. OE.	3D Spher.	MC
P_c	3.53E-5	4.06E-5	6.05E-5	5.892E-5
Test Case VI	Cart.	2D Rel. OE.	3D Spher.	MC
P_c	7.96E-9	8.77E-6	1.050E-5	1.200E-5
Test Case VII	Cart.	2D Rel. OE.	3D Spher.	MC
P_c	2.79E-5	2.08E-11	1.71E-11	0.0

86

Cases II, VI, and VII were designed to highlight the difference between linear and non-linear techniques for computing the P_c. This is evident by the difference seen in the results obtained using linear Cartesian analysis versus the fully nonlinear Monte Carlo analysis. Relative orbital based linear methods to compute P_c formulations developed in this chapter are seen to provide up to orders of magnitude accuracy improvement over the classical linear Cartesian method. To reiterate, the Cartesian, 2D Relative Orbital Element, and 3D Spherical results in Table 4.1 were obtained using only linear analysis, with no use of the GMM or Local Gaussian enhancements.

To better understand the results in Table 4.1, it is helpful to look at the linearly propagated distributions projected into Cartesian space compared to the true distribution.
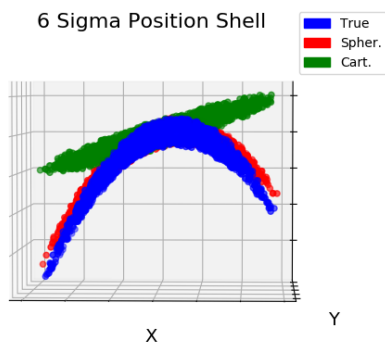
Figure 4.2: True Position Distribution Compared to Linearly Propagated Cartesian and Spherical Distributions Projected into $x - y - z$ Space. Reprinted with permission from [103].
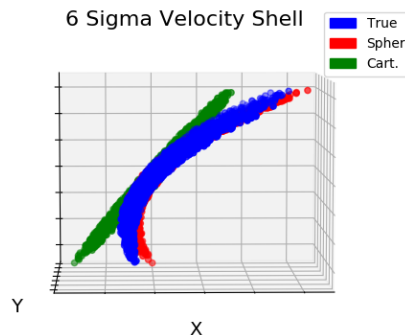
Figure 4.3: True Velocity Distribution Compared to Linearly Propagated Cartesian and Spherical Distributions Projected into $\dot{x} - \dot{y} - \dot{z}$ Space. Reprinted with permission from [103].

In Figures 4.2 and 4.3, an ensemble of states on the 6σ ellipsoid of a Normal distribution that was initially Gaussian in orbital element space were propagated through the nonlinear equations of orbital motion resulting in the true (blue) distribution. The approximate linear Cartesian (green) and Spherical (red) distributions were generated by linearly propagating the ensemble of initial

states about the nominal trajectory using the STM in orbital elements and the linearized mapping from the orbital elements into Cartesian and spherical coordinates respectively. The linearized Spherical distribution was then mapped into Cartesian coordinates using the algebraic relations between spherical and Cartesian coordinates. While the linearized Cartesian distribution is tangent to the true distribution at the point of expansion, it is unable to capture the banana shape of the true distribution. The linearized distribution in spherical coordinates is seen to do a much better job approximating the shape of the true distribution.

Matching the shape of the distribution, at least approximately, is important for avoiding false positives or negatives, but does not guarantee an accurate PDF or P_c computation. To compare the accuracy of the approximate distributions, the density of states at various sigma levels are computed and then compared to the Liouville solution [132, 31], which gives the true density of a state in the absence of process noise. These level set results are presented in Figures 4.4 and 4.5. To serve as a baseline for how well a linearized distribution can approximate the true distribution, results for the linearized distribution in Modified Equinoctial orbital elements are included.
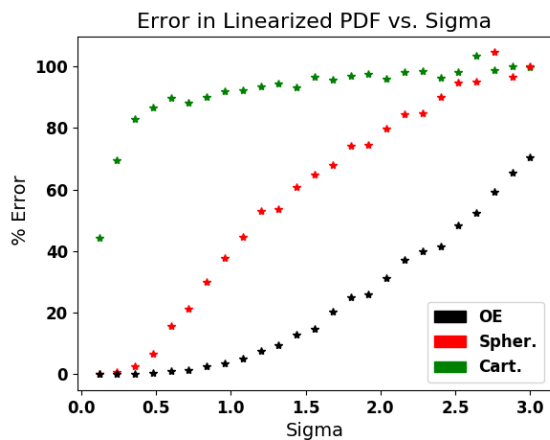
Figure 4.4: Average Error in the Linearly Propagated PDF vs the Liouville Solution as a Function of σ and Coordinate Choice. Reprinted with permission from [103].
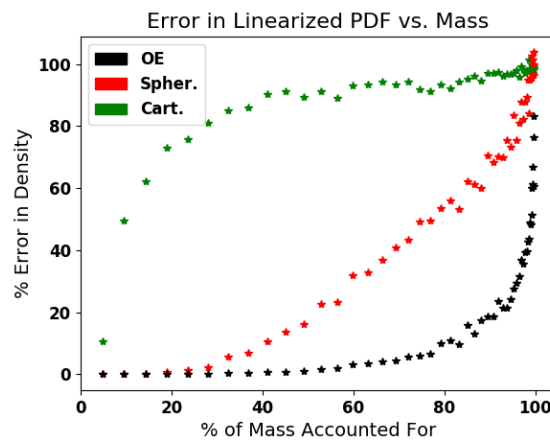
Figure 4.5: Average Error in the Linearly Propagated PDF vs How Much Mass Has Been Accounted For. Reprinted with permission from [103].

It is clear that while linearization in spherical coordinates is much more accurate than Cartesian for linearly approximating the propagated PDF, there is still considerable error in trying to linearly approximate the true PDF for this problem. However, if one is only approximating a portion of the PDF, as is the case with the Local Gaussian approximation, spherical coordinates are an excellent choice.

In cases where local approximations are insufficient to accurately construct the joint PDF, such as when the relative inclination between the orbits is low, it may be necessary to use a global approximation method. Currently, the most popular global approximation method that has been used by others on this problem [74, 72, 73], is the GMM. As was shown in Chapter 3, the use of a nonlinearity index [42] can play an important role in estimating the number of mixture components needed to model the propagated non-Gaussian PDF and greatly enhance GMM. In Figure 4.6, the nonlinearity (NL) index for the mapping from Modified Equinoctial orbital elements into either Cartesian or spherical coordinates is shown. The NL index was calculated at intervals along the Eigenfiber of the distribution in orbital elements.
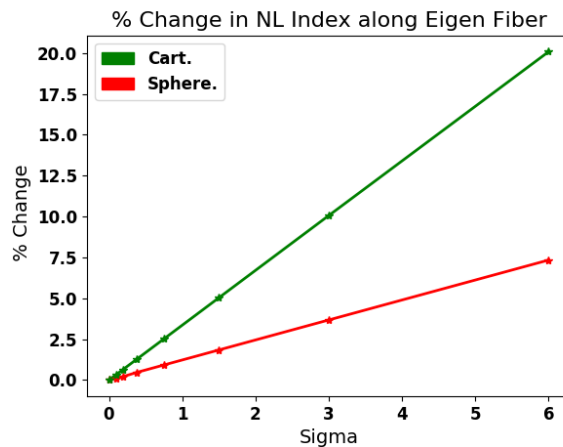
Figure 4.6: Percent Change in the NL Index Along the Eigenfiber. Reprinted with permission from [103].

From Figure 4.6 it is easy to see that the conversion to spherical coordinates is more linear than the transformation into Cartesian along the Eigenfiber. What this figure means in a practical sense can be communicated by the following short example. For example, if a linearity tolerance of 2.5 % is to be satisfied then mixture components would need to be placed at about 1σ intervals along the Eigenfiber if the PDF is to be mapped into Cartesian coordinates. If the PDF is to be mapped into Spherical coordinates then the tolerance is met with wider spacing of about 2.5σ. Or in other words, less than half the mixture components are needed at this tolerance.

Next, the new methods were tried on cases I - VII from Chapter 3. This time Cartesian and 3D Spherical methods made use of the Local Gaussian enhancement. The 2D method was run without enhancements. In Table 4.2 there are six columns of data. Column one has the results from the prefilter for the ascending/ descending node. Note that the prefilter was not run on cases with parametric force model uncertainty. Columns two through five contain the predicted P_cs for each method along with how long (CPU time) it took the algorithm to run. Column six contains the percent improvement in accuracy for the 3D spherical method over the Cartesian method as well as the percent reduction in run time goring from Cartesian to spherical. It should be noted that the P_c values presented in Tables 4.1 and 4.2 are for a single close approach, even though there are multiple close approaches possible for many of these test cases.

Looking at Table 4.2, the use of local Gaussians has allowed the Cartesian method to close most of the performance gaps seen from Table 4.1. The remaining differences however, are not negligible. The 3D spherical method resulted in an average of 52 % improvement in the accuracy of the solution over Cartesian and and average speed up of 55 %. The 3D spherical method was also more consistent in its run time across the different cases. This is because the 3D spherical method requires fewer Local Gaussian expansions to meet a given linearity tolerance. The 2D method was ballpark close when predicting the P_c, but lacked the consistent accuracy of either of the 3D methods when local Gaussians were used. However, the 2D method was more accurate than the 3D Cartesian method when doing linear analysis, as was seen in Table 4.1. Notably, in cases III and V, the 2D method was the most accurate. This is likely due to there being large errors

90

Table 4.2: CRATER Results Cartesian vs Relative OE. Reprinted with permission from [103].

TC I	PC*	Cart.	2D Rel. OE.	3D Spher.	MC	% Improvement
PC	2E-2/2E-3	2.809E-4	1.99E-04	2.464E-4	2.675E-4	-
Time	-	1.1 sec	0.09 sec	0.6 sec	26299 sec	43%
TC II	PC*	Cart.	2D Rel. OE.	3D Spher.	MC	% Improvement
PC	6E-3/6E-3	5.97E-5	4.06E-05	5.927E-5	5.89E-05	-
Time	-	7.8 sec	0.09 sec	1.0 sec	65250 sec	87%
TC III	PC*	Cart.	2D Rel. OE.	3D Spher.	MC	% Improvement
PC	3E-1/0	9.29E-4	9.29E-04	9.961E-4	9.74E-04	-
Time	-	1.5 sec	0.11 sec	0.61 sec	25038 sec	60%
TC IV	PC*	Cart.	2D Rel. OE.	3D Spher.	MC	% Improvement
PC	NA	6.149E-4	4.05E-04	6.1E-4	2.21E-04	-
Time	-	0.6 sec	0.1 sec	0.6 sec	26200 sec	0%
TC V	PC*	Cart.	2D Rel. OE.	3D Spher.	MC	% Improvement
PC	NA	12.1E-3	5.62E-03	6.386E-3	5E-3	-
Time	-	0.73 sec	0.1 sec	0.6 sec	28000 sec	18%
TC VI	PC*	Cart.	2D Rel. OE.	3D Spher.	MC	% Improvement
PC	1E-3/6E-4	1.235E-5	8.77E-06	1.201E-5	1.200E-5	-
Time	-	5.49 sec	0.09 sec	0.62 sec	32000 sec	89%
TC VII	PC*	Cart.	2D Rel. OE.	3D Spher.	MC	% Improvement
PC	1E-2/1E-2	2.187E-11	2.08E-11	2.29E-11	0.0	-
Time	-	5.78 sec	0.1 sec	0.69 sec	27800 sec	87%

in the velocity portion of the linearized PDF compared to the position portion.

The prefilter successfully flagged each test case for further analysis and P_c^* bounds the actual P_c each time. Test Case VII would be difficult to filter out without doing a nonlinear P_c analysis since a linear analysis results in a much higher P_c as seen in Table 4.1. Enhancements to this method are made in the next chapter to make these prefiltering bounds less conservative.

4.4 Conclusions

The relative orbital elements $\{\Omega_r, i_r, \omega_r\}$ provide important insights into the satellite collision problem that are not apparent when using Cartesian coordinates or even orbital elements computed with respect to an inertial frame. In particular they give the location of the relative line of nodes with respect to the $\hat{x}$ axis of the perifocal frame for both satellites. This information was used to predict the probability of a close approach (P_c^*) along this critical line in a prefiltering technique

which improved upon widely used geometric filters by incorporating the initial state uncertainties of the two satellites. This, combined with the phase information, allowed for the close approach to be defined in a probabilistic manner rather than by heuristic bounds on deterministic calculations. Furthermore they played an integral part in the formulation of the 2D P_c method. By projecting the uncertainty in the inertial orbital elements onto the relative elements, we defined a fixed plane of collision and obtained conditions for collisions on this plane in terms of the relative orbital elements. For the 3D method they were used to obtain a spherical coordinate frame that avoids the polar singularity issues associated with spherical coordinates for any collision by defining the x-y plane in terms of the orbital plane of one of the satellites. Useful insights established where to place local Gaussian expansion points to obtain a good local approximation of the joint PDF (see steps 8 and 9 from algorithm 1).

In the development of the new 2D and 3D methods we were able to avoid converting to Cartesian coordinates to carry out the P_c computation. The effect of this was to make the entire problem more linear as evidenced by the marked improvement in accuracy when using linear analysis (see Table 4.1), and by the NL index (see Fig. 4.6). Importantly the linearized PDFs in these curvilinear coordinates were more accurate when compared to the solution of the Liouville equation and preserved the shape of the true PDF better than their Cartesian counterpart (see Fig.s 4.2 - 4.5). When doing nonlinear P_c analysis, the new methods were comparable in accuracy to the nonlinear Cartesian method but with improvements in speed (see Table 4.2).

5. STEADY STATE ANALYSIS AND ORBITAL ELEMENT METHODS

5.1 Introduction

The developments of the previous chapters are largely focused on pushing the current state-of-the-art forward in terms of uncertainty propagation and P_c calculation in a computationally efficient and accurate manner for conjunction analysis. The present study hopes to compliment this body of work (as well as the wider literature) by contributing additional fundamental insights into the collision problem as well as new methods for achieving improved P_c algorithms.

One such insight has come from the investigation of the long term behavior of colliding objects subject to Kepler motion. This insight resulted from asking the question: What is the steady state probability of collision for two orbiting objects with known initial distributions? As will be shown, this question led to the discovery of the upper bound in the P_c between two classically orbiting objects. There are a number of ways of bounding the probability of collision that have been developed by various authors. These bounds, however, were developed to account for uncertainty in the colliding objects initial covariances, uncertainty in the dynamics or error due to some underlying assumption [145, 88]. The bound developed here is different and is a supremum on the P_c for two orbiting objects with known initial distributions subject to Keplerian motion. This steady state P_c is useful for quickly computing an upper bound on the risk of collision between two objects, even if the initial distributions are not Gaussian. The result and especially this line of thinking can also be useful in informing what the SSA requirements for a new mission should be in order to limit the long term risk of collision with other objects. This is because the steady state P_c is not concerned with the satellite's initial true anomaly, but only with how well the orbit is known.

To compute this steady state P_c we first consider letting time go to infinity while assuming Keplerian motion. As such this approach is clearly better suited and easily visualized for the case of nearly circular orbits, since the collision geometry is almost invariant as the two orbits precess

with respect to one another under the influence of the gravitational harmonics.

In order to relax some of the assumptions made in computing the steady state P_c, another bound is computed for a single close approach. This result is much more in holding with other bounds on the P_c previously discussed in the literature, but has the distinction of being easy to compute for non-Gaussian distributions. This is achieved by using the steady state P_c and then computing the probability of one of its major conditioning events. This conditioning event is shown to be well approximated by simple bound on the satellites time varying anomaly. Computing the probability that the time varying anomaly is within this bound, together with the steady state P_c, will yield a bounding probability for a given close approach. This upper bound for a single close approach is also easily computed for non Gaussian distributions, since the conditioning event is in a single dimension making function approximations and integration in this one dimensional space are trivial. This upper P_c bound for a single pass will be compared to both the steady state P_c and the transient solution on a number of test cases.

The final major focus of this chapter is to address a long standing difficulty in accurately computing the P_c over a given time interval. It has long been acknowledged that there are benefits to performing uncertainty propagation in orbital element space [129, 130]. Unfortunately, for the purposes of conjunction analysis, the state PDF is often mapped into Cartesian coordinates, or some other coordinate frame, where the relative distances are easily defined in order to compute P_c. Since the mapping from orbital elements into this new coordinate frame is nonlinear, special techniques must be employed to accurately approximate the "more non-Gaussian" PDF in this new coordinate frame. These techniques can range from efficient local approximations, demonstrated in Chapter 3, to less efficient (but more generally applicable) global approximation techniques like the Gaussian Mixture [73] or orthogonal basis functions [136]. In either case, great care must be taken to ensure that the mapped PDF and resulting P_c are accurate. These difficulties will be addressed, in this chapter, by deriving a formulation of the P_c integral that is evaluated in the orbital element space.

This new formulation of the P_c is made possible through the use of the relative orbital elements

developed in Chapter 4. Being able to compute the P_c in the orbital element space will eliminate the nonlinear transformation associated with mapping the propagated PDF from orbital element space to another coordinate system as is typically done to be able to compute P_c. While computing the P_c in element space makes the propagated PDF easier to accurately approximate, it complicates the formulation of the P_c integral. This increase in complexity will shift the computational burden away from approximating the propagated PDF to numerically evaluating the P_c integral. This new orbital element method for computing P_c will be derived for the general collision case and then demonstrated and compared to Monte Carlo for a number of reduced dimension cases.

5.2 Methods

5.2.1 Steady State Distribution

Let us consider two satellites S_1, S_2. Suppose that the satellites are distributed according to the PDF's D_1, D_2 respectively. These distributions are defined at some initial time t_0 and are allowed to evolve according to the Liouville equation [146]. In particular, this means that the probability mass associated with a given trajectory $X_1(t)$ is constant for all t. The support of these distributions is defined on $\mathbb{R}^6$ whose coordinate axes are given by the classical orbital elements $\{a, e, i, \omega, \Omega, M\}$. Where M is the mean anomaly.

For the present analysis, let us limit our discussion to objects undergoing idealized Keplerarian motion. Note that for the prescribed motion, the first five elements are constant with $M(t)$ varying linearly with time. Since the first five orbital elements are constant for the prescribed motion, the distribution over this five element subspace is also constant. Examining the behavior of $M(t)$ we hope to arrive at a steady state distribution. Recall that for Kepler dynamics $M(t)$ is given by

$$M(t) = M_0 + n(t - t_0) \tag{5.1}$$

where $n(a) = \sqrt{\frac{\mu}{a^3}}$. Suppose we choose two neighboring trajectories from X_1 with semi-major axes $a, a + \Delta a$ such that the difference in the probability density of the two trajectories is less than

some $\epsilon > 0$.

$$|D_1(a) - D_1(a + \Delta a)| < \epsilon \tag{5.2}$$

These two orbits have a relative period of

$$P_{rel} = \frac{2\pi}{|n(a) - n(a + \Delta a)|} \tag{5.3}$$

Notice that after one relative orbit, the density along the arc connecting the two neighboring trajectories does not vary by more than ϵ. Where epsilon can be chosen arbitrarily small for large enough t. Therefore, as $t \to \infty$ the probability density of M along the arc can be taken as constant (see Figure 5.1). Hence, in the limit as $t \to \infty$, M is uniformly distributed $M \sim U[0, 2\pi]$.
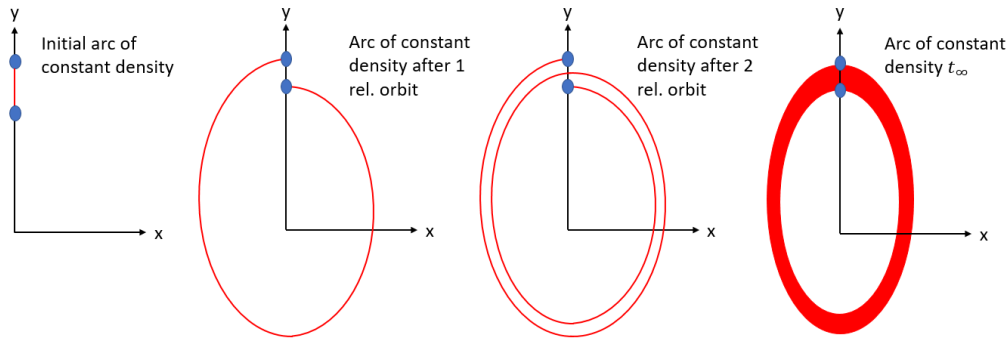
Figure 5.1: Evolution of Mean Anomaly Distribution.

Given that the distribution is uniform in M, a steady state distribution in terms of the true anomaly f can also be obtained. To obtain the distribution in terms of f, a differential probability mass dm is written in terms of density and a differential volume in both the true and mean anomaly spaces. Since M is uniformly distributed, its density is a constant $\frac{1}{2\pi}$. The density function over f is unknown and is written as $\rho(f)$. Since the differential probability mass is equal in these two spaces, we obtain the following.

$$dm = \frac{1}{2\pi}dM = \rho(f)df \tag{5.4}$$

Next, recalling that $\frac{dM}{dt} = n$ and $\frac{df}{dt} = \frac{h}{r^2}$, we obtain the steady state distribution of f for a given e as

$$\rho(f|e) = \frac{1}{2\pi}\frac{dM}{df} = \frac{1}{2\pi}\frac{dM}{dt}\frac{dt}{df} = \frac{n}{2\pi h}r^2 = \frac{(1-e^2)^{\frac{3}{2}}}{2\pi(1 + e\cos(f))^2} \tag{5.5}$$

.

Unlike the the steady state distribution for the mean anomaly, the distribution of the true anomaly in equation (5.5) is not uniform for $e > 0$, but reflects the truth that orbiting objects tend to spend most of their time near apoapsis. This result is qualitatively an expected consequence of Kepler's second law. Conversely, the distribution of f approaches the uniform distribution as $e \to 0$ since $f = M$ when $e = 0$. The distribution of f is plotted for different orbit eccentricities in Figure 5.2.
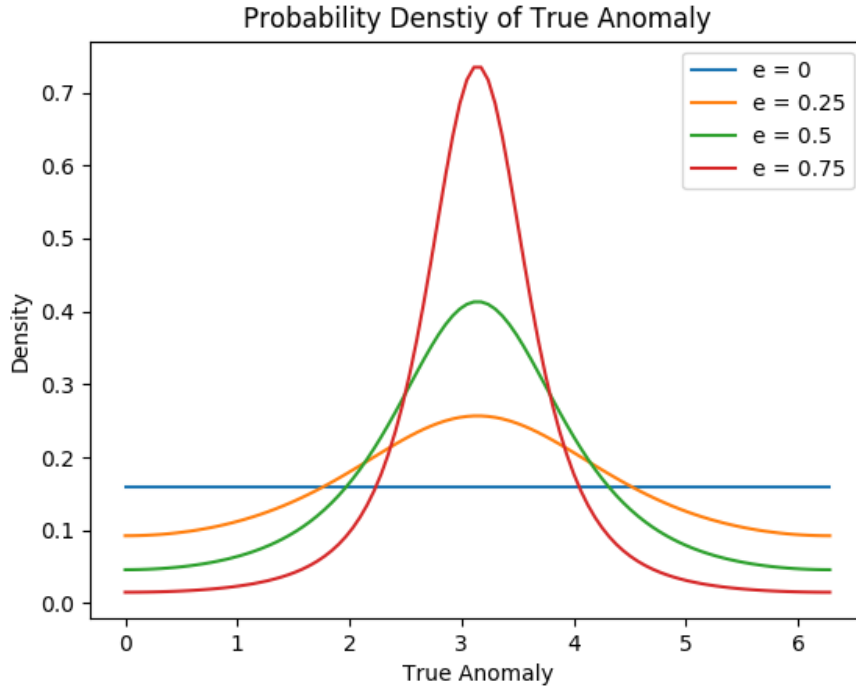
Figure 5.2: Steady State Distribution of True Anomaly.

At this point we have expressions for the steady state distributions of the mean and true anomalies and would like expressions for the entire state vector's distribution in the steady state. This is constructed using the law of total probability [131].

$$D_x(x) = \Sigma_{i=1}^{N} D(x|y_i) D_{y_i}(y_i) \tag{5.6}$$

Let us partition our state vector $X_\infty = [f, q_0]$, where $q_0 = \{a, e, i, \omega, \Omega\}$. Using the law of total probability the distribution of X_∞ is given by.

$$D_{X_\infty}(X_\infty) = \rho(f|e) D\big(q_0(t_0); t_0, t_0\big) \tag{5.7}$$

5.2.2 Steady State Probability of Collision

Now that an expression for the steady state distribution has been obtained, it is desired to compute the steady state probability of collision $P_{C\infty}$. The collision event shall be defined using the radius of collision R_c [76]. That is, a collision is said to occur between two trajectories, if at any point the distance between them is less than R_c. In the transient case, each close approach between satellites brings a subset of trajectories from the distributions D_1, D_2 within R_c of each other. For the steady state probability of collision $P_{C\infty}$, all infinity of close approaches will be considered simultaneously. This requires finding all of the state pairs from the initial orbital element distributions that will at some point result in a collision.

For a given sample from the joint PDF (q_{0_1}, q_{0_2}), we can compute the f_1^*, f_2^* that result in the minimum separation between the two satellites. If this distance is less than R_c, the trajectory pair results in a collision, otherwise they won't collide even as $t \to \infty$. The question then is what is the probability that $f_1 = f_1^*$ and $f_2 = f_2^*$ simultaneously as $t \to \infty$. To further illustrate, but without loss of generality, let us suppose that orbits from the two distributions are nearly circular, such that

$$f(t) \approx M(t) = M(t_0) + \sqrt{\left(\frac{\mu}{a^3}\right)}(t - t_0) \tag{5.8}$$

Now for some time between t_0 and one orbital period of S_1 it is evident that $f_1(t) = f_1^*$ for $t = t_1^*$ for any q_0 from D_1. At the time t_1^* we compute the true anomaly of S_2. We would now like to find if there is a future time such that $f_2(t) = f_2^*$ for any q_0 from D_2. This can be done by looking at the quantity $\Delta f(t) = f_2(t) - f_1(t)$ and seeing if there is a time such that $\Delta f(t) = \Delta f^* = f_2^* - f_1^*$.

$$\Delta f^* = \Delta f(t_1^*) + \left(\sqrt{\frac{\mu}{(a_1 + \Delta a)^3}} - \sqrt{\frac{\mu}{a_1^3}} \right)(t - t_1^*), \quad t \geq t_1^* \tag{5.9}$$

where $a_2 = a_1 + \Delta a$.

It is apparent looking at equation 5.9 that for any finite Δa, there is a finite t^* such that $\Delta f(t^*) = \Delta f^*$. Rearranging this equation to solve for Δa and taking the limit as $t \to \infty$ it can be seen that as time goes to infinity $\Delta a \to 0$. Therefore the probability that both $f_1 = f_1^*$ and $f_2 = f_2^*$ simultaneously as $t \to \infty$ is one for any (q_{0_1}, q_{0_2}).

Thus, finding the steady state probability of collision is the same as finding the probability that the minimum distance between two orbits sampled from distributions D_1, D_2 is less than R_c and is consequently the maximum P_c that can result from distributions D_1, D_2. This can be seen by looking at the formula for the steady state P_c.

$$P_c(t) = P_c(t_0) + \int_{t_0}^{t} \int_{\Lambda_\tau} D_1\big(X_1(\tau); \tau, t_0\big) D_2\big(X_2(\tau); \tau, t_0\big) d\Lambda_\tau d\tau \tag{5.10}$$

Where again, Λ_τ is the set of all states that uniquely satisfy the conditions for a collision at time $t = \tau$ and X_1, X_2 are the state vectors.

Since the integrand $D_1\big(X_1(t)\big) D_2\big(X_2(t)\big) \geq 0$ for all t and X_1, X_2, the function $P_c(t)$ must be monotonically increasing. That is $P_c(t) \leq P_c(t+\Delta t)$ for any t where $\Delta t > 0$. Also, by the property of distributions $P_c(t) \leq 1$ for any t. Since $P_c(t)$ is a monotonically increasing bounded function, there exists some upper limit on the probability of collision $\|P_c\|_\infty$. Therefore, the maximum probability of collision for any two objects is given by

$$\lim_{t \to \infty} P_c(t) = ||P_c||_\infty \leq 1 \tag{5.11}$$

For many orbits $\|P_c\|_\infty$ is well approximated by computing the probability that $\Delta r \leq R_c$ along the line of relative nodes as was done in chapter 4. The analysis presented here has extended that work to allow for general distributions and has shown that it is the minimum upper bound on the P_c as $t \to \infty$ for cases where the minimum miss distance between two orbits can approximately be said to lie on the line of relative nodes.

5.2.3 $\|P_c\|_\infty$ for a Single Pass

The result of Section 5.2.2 provides good insight into the bounding probability of collision between two orbits and the nodes of interest. However the assumption of Kepler motion while letting $t \to \infty$ may cause either over or under prediction of the bounding probability. We therefore seek a more practical bounding probability that is easily calculated for general distributions.

In this case we look at an upper bound on the probability of collision for a single close approach between two satellites S_1, S_2 with initial distributions $D_1(\boldsymbol{q}_1, t_0; t_0)$, $D_2(\boldsymbol{q}_2, t_0; t_0)$ and perturbed orbital motion. Suppose a close approach is predicted for $t \in [t_a, t_b]$. t_a is chosen such that no state from either distribution has come within R_c of each other yet. This is done using the eigenfiber. To facilitate the computation, the state uncertainty in $\boldsymbol{q}_1, \boldsymbol{q}_2$ at t_a will be mapped into the relative orbital elements. Furthermore the interval $[t_a, t_b]$ shall be assumed to be sufficiently small such that Kepler dynamics hold over the interval. Note that this last assumption is valid for almost all collision scenarios.

In the previous section, we derived an expression for P_{C_∞}. One way to think about this value, is that it gives the probability of collision given f_1, f_2 are chosen such that the relative distance between each point from the distributions of S_1, S_2 is at a minimum. The argument being, that as time goes to infinity the probability that f_1, f_2 assume these values simultaneously is one.

Suppose now that we propagate the distributions of $\boldsymbol{q}_1$ and $\boldsymbol{q}_2$ to obtain $D_1(\boldsymbol{q}_1; t_a, t_0)$ and $D_2(\boldsymbol{q}_2; t_a, t_0)$ respectively. We then use these distributions to compute $\|P_c\|_\infty$ as was prescribed in the previous section. Now suppose that the following sets are defined. Let

$$\mathbb{A} \equiv \{(\boldsymbol{q}_{a_1}, \boldsymbol{q}_{a_2}) | \min(r(t)) \leq R_c, \ \ t \in [t_a, \infty)\} \tag{5.12}$$

Where $\boldsymbol{q}_{a_k} = [a_k, e_k, i_k, \omega_k, \Omega_k]^T$, $k = 1, 2$ are the partial state vectors for satellites S_k sampled from their respective distributions at t_a. In this sense, $\mathbb{A}$ is the set of all orbit pairs with a minimum miss distance of less than R_c. For convenience let $\boldsymbol{q}_a \equiv (\boldsymbol{q}_{a_1}, \boldsymbol{q}_{a_2})$ denote a trajectory pair. Next the set $\mathbb{B}$ is defined as the set of all $f \equiv (f_1, f_2)$ pairs such that $f_1 = f_1^*$ and $f_2 = f_2^*$ simultaneously or $f = f^*$. Where, again f^* minimizes the distance of the trajectory pair $\boldsymbol{q}_a$. Recall Bayes rule which gives

$$P(A|B) = \frac{P(A \cap B)}{P(B)} \tag{5.13}$$

for any events A and B. If the event A is defined as $\boldsymbol{q}_a \in \mathbb{A}$ and the event B defined as $f \in \mathbb{B}$, equation 5.13 can be rearranged to solve for $P(A \cap B)$.

$$P(A \cap B) = P(\boldsymbol{q}_a \in \mathbb{A}|f \in \mathbb{B})P(f \in \mathbb{B}) \tag{5.14}$$

From the previous section it is clear that $P(\boldsymbol{q}_a \in \mathbb{A}|f \in \mathbb{B}) = \|P_c\|_\infty$ and that as time goes to infinity $P(f \in \mathbb{B}) = 1$. For the single pass, time shall not be allowed to go to infinity, but will instead be limited to the interval $[t_a, t_b]$. Over this time interval we shall attempt to find $P(f \in \mathbb{B})$. In general this is quite difficult, since f^* can usually only be found by root finding methods [77, 147]. Since an upper bound is being sought, the set $\mathbb{B}$ will be approximated as a box in f_1, f_2 space, such that all $f^* \in \mathbb{B}$ satisfy $f_1 \in [f_a, f_b]$ and $f_2 \in [f_c, f_d]$. Let this box be called $\mathbb{B}^*$. The $P(f \in \mathbb{B}^*)$ will depend greatly on the definition of $\mathbb{B}^*$. For all but nearly co-planar orbits, all f^* (that produce a miss distance of less than R_c) will be contained within a small box about the relative line of nodes. If we define this box as $\mathbb{B}^*$, then $\mathbb{B} \subseteq \mathbb{B}^*$ and

$$P(A \cap B) \leq P(\boldsymbol{q}_a \in \mathbb{A}|f \in \mathbb{B})P(f \in \mathbb{B}^*) \tag{5.15}$$

The bounds of this box are computed using the relative orbital elements of Chapter 4. Recall that when the uncertainty is projected onto the relative orbital elements, the orbital plane of S_1 can be considered fixed, such that collision are only possible for $|z_2| \leq R_c$ if z is parallel to the angular

101

momentum vector of S_1. If we then define $z_2 = r_2 \sin\left(f_2 + \omega_r\right)\sin\left(i_r\right)$, we can solve for the f_2 such that $z_2 = \pm R_c$ with ω_r, i_r taking their extreme values from the distribution. This yields the values of $[f_c, f_d]$. Next, let $y_2 = r_2 \sin\left(f_2 + \omega_r\right)\cos\left(i_r\right)$ and compute the extreme values of y_2 at the points were S_2 comes within R_c of S_1's orbital plane (i.e where $f_2 = f_c$ and $f_2 = f_d$). Now define $y_1 = r_1 \sin\left(f_1 - \Omega_r\right)$ and find the f_1 such that $y_1 = y_2$ for extreme values of Ω_r yielding the values $[f_a, f_b]$. With the bounds of $\mathbb{B}^*$ defined we move on to computing $P(f \in \mathbb{B}^*)$.

While it is easy, at any given fixed time $t_i \in [t_a, t_b]$, to compute $P\left(f_1(t_i) \in [f_a, f_b]\right)$ and $P\left(f_2(t_i) \in [f_c, f_d]\right)$, these instantaneous probabilities cannot simply be integrated over time to yield the probability of the event over the entire time interval. To derive the correct expression the following example is employed.

Consider two independent objects P_1, P_2. Suppose that P_1 has the distribution $\rho_1\left(x; t, t_0\right)$ and P_2 has the distribution $\rho_2\left(y; t, t_0\right)$. P_1 is located along the x-axis and moves in the positive x direction at $1u/s$, while P_2 is along the y-axis and moves in the positive y direction at $1u/s$. In this example we would like to find the probability that P_1 and P_2 are both within a unit box centered at the origin over the time interval $[t_0, t_f]$. To compute the probability of the event, the time interval shall be broken into two segments $[t_0]$ and $(t_0, t_f]$. At t_0 the probability of both objects being within the unit square (P_0) is simply given by the product of the probability of each object P_1, P_2 being within the region independently.

$$P_0 = \int_{-\frac{1}{2}}^{\frac{1}{2}} \rho_1\left(x; t_0, t_0\right) dx \int_{-\frac{1}{2}}^{\frac{1}{2}} \rho_2\left(y; t_0, t_0\right) dy \tag{5.16}$$

Next we wish to consider $t = t_0 + \Delta t$. During this time step new probability mass enters the region from both distributions $\rho_1\left(x = -\frac{1}{2}; t_0 + \Delta t, t_0\right) dx$, $\rho_2\left(y = -\frac{1}{2}; t_0 + \Delta t, t_0\right) dy$. This new probability mass is multiplied by the probability that the other object is within the region at time t.

$$\Delta P = \left\{\rho_1\left(x = -\frac{1}{2}; t_0 + \Delta t, t_0\right) dx * \int_{-\frac{1}{2}}^{\frac{1}{2}} \rho_2\left(y; t_0 + \Delta t, t_0\right) dy\right\} +$$
$$\left\{\rho_2\left(y = -\frac{1}{2}; t_0 + \Delta t, t_0\right) dy * \int_{-\frac{1}{2}}^{\frac{1}{2}} \rho_1\left(x; t_0 + \Delta t, t_0\right) dx\right\} \tag{5.17}$$

Taking the limit of (5.17) as $t \to 0$ and letting $dx = \frac{dx}{dt}dt$ and $dy = \frac{dy}{dt}dt$ yields an expression for the differential increase in probability of the event that can be integrated over time.

$$
dP = \left\{ \rho_1\left(x = -\frac{1}{2}; t, t_0\right)\frac{dx}{dt}dt * \int_{-\frac{1}{2}}^{\frac{1}{2}} \rho_2\left(y; t, t_0\right)dy \right\} + \\
\left\{ \rho_2\left(y = -\frac{1}{2}; t, t_0\right)\frac{dy}{dt}dt * \int_{-\frac{1}{2}}^{\frac{1}{2}} \rho_1\left(x; t, t_0\right)dx \right\}
$$
(5.18)

Performing this integration and recalling P_0 as defined in (5.16) yields

$$
P_I = P_0 + \int_{t_0}^{t_f} \left\{ \left(\rho_1\left(x = -\frac{1}{2}; t, t_0\right)\frac{dx}{dt} * \int_{-\frac{1}{2}}^{\frac{1}{2}} \rho_2\left(y; t, t_0\right)dy \right) + \\
\left(\rho_2\left(y = -\frac{1}{2}; t, t_0\right)\frac{dy}{dt} * \int_{-\frac{1}{2}}^{\frac{1}{2}} \rho_1\left(x; t, t_0\right)dx \right) \right\}dt
$$
(5.19)

This example is exactly analogous to finding the probability that the true anomalies are within the bounding box about the line of relative nodes. Substituting this result into the the expression for bounding probability for a single pass (5.15), replacing x and y with f_1 and f_2 gives us the final result.

$$
P_{C_\infty[a,b]} = P_{C_\infty} P_I, \quad t \in [t_a, t_b]
$$
(5.20)

This expression should yield a much tighter bound on the P_c and is easily compute for general distributions.

5.2.4 Transient Solution

The result in Section 5.2.2 motivates the search for a solution to the transient P_c problem in terms of the relative orbital elements. We shall employ the same assumptions as in Section 5.2.3. Let us consider the collision problem for satellites S_1, S_2 with initial distributions $D_1(\boldsymbol{q}_1, t_0; t_0)$, $D_2(\boldsymbol{q}_2, t_0; t_0)$ where $\boldsymbol{q}_1$, $\boldsymbol{q}_2$ are orbital elements. Suppose that a close approach is possible for time $t \in [t_a, t_b]$. Using any appropriate method, the distributions are propagated from t_0 to t_a allowing for perturbing accelerations and process noise to obtain the distributions $D_1(\boldsymbol{q}_1, t_a; t_0)$, $D_2(\boldsymbol{q}_2, t_a; t_0)$. For $t \in [t_a, t_b]$ we shall assume deterministic unperturbed Kepler dynamics. This

allows us to hold five of the orbital elements as constant and, without stochastic forcing, the distributions evolve according to the Liouville equations during the interval $[t_a, t_b]$. As before, a collision is said to occur if the Euclidean distance between any two states is less than or equal to R_c.

For the transient case we face the difficulty of defining a set such that all colliding trajectories belong to the set only once during the collision interval. One proposed definition for this set is

$$\Lambda_\tau = \{(\boldsymbol{q}_1, \boldsymbol{q}_r) | r = R_c \text{ and } \boldsymbol{r} \cdot \boldsymbol{V} \le 0 \text{ for } t = \tau\} \tag{5.21}$$

where $\boldsymbol{r}$ is the relative position vector $(\boldsymbol{r}_1 - \boldsymbol{r}_2)$ and $\boldsymbol{V} = (\boldsymbol{v}_1 - \boldsymbol{v}_2)$. This is analogous to the definition used in [96] except now the set Λ_τ will be defined in terms of orbital elements. If we define the differential volume of the set Λ_τ as $d\Lambda_\tau$ then the probability of collision can be written as

$$P_c = \int_{t_a}^{t_b} \int_{\boldsymbol{q}_1} \int_{\Lambda_\tau} D_1(\boldsymbol{q}_1, \tau; t_0) D_r(\boldsymbol{q}_r, \tau; t_0) d\boldsymbol{q}_1 d\boldsymbol{q}_r \tag{5.22}$$

Unfortunately to evaluate this expression in the orbital element space, we will not be able to apply convenient analytical integration. This will necessitate the construction of some form of quadrature grid. It is desired that this grid of points is dense where the joint probability density is high and sparse elsewhere. To accomplish the construction of the grid, we use an eigenvalue decomposition of the second statistical moment of D_r to generate an orthogonal grid of points in the relative orbital element space along the eigenvectors. Here only quadrature points for the portion of the PDF that approximately lies between $z = \pm R_c$ are placed. This is done by finding the corresponding locations along the eigenfiber (see Chapter 3 and 4) that intersect these two planes. Then a six dimensional grid is created along the eigenvectors of the distribution between these two points. The distribution D_r need not be Gaussian, as we are only using the covariance to construct the quadrature grid. Consequently, as the distribution D_r evolves with time, this grid will need to be re-created at each time step and D_r will need to be evaluated at each grid point.

We then map these grid points into Cartesian position and velocity coordinates. Each grid point has coordinates $X_i = [x_i, y_i, z_i, \dot{x}_i, \dot{y}_i, \dot{z}_i,]$. Since all points of S_1's distribution are constrained to the x-y plane, the points of S_1's distribution that satisfy the condition $r = R_c$ are solutions to the equation

$$R_c^2 - z_i^2 = x_1^2 + y_1^2; \quad z_i \leq R_c \tag{5.23}$$

as shown in Figure 5.3, where $x_1 = r_1 \cos(f_1)$ and $y_1 = r_1 \sin(f_1)$.
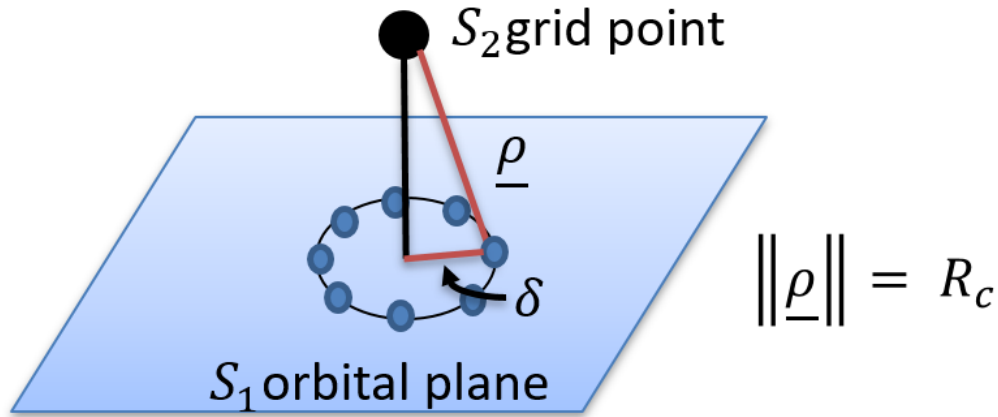
Figure 5.3: Grid of S_1 States Satisfying the $\rho = R_c$ Constraint.

For a given (x_1, y_1) along this circle we notice that f_1 and r_1 are constant, since the orbital plane of S_1 is fixed. Thus r_1 is simply

$$r_1 = \frac{a_1(1 - e_1^2)}{1 + e_1 \cos(f_1)}$$

Recalling that $x_1 = r_1 \cos f_1$, we solve for a_1 in terms of e_1 and the constant x_1 and find.

$$a_1 = \frac{(r_1 + e_1 x_1)}{(1 - e_1^2)} \tag{5.24}$$

This gives an explicit constraint on the (a_1, e_1) pairs that satisfy the constant r_1 constraint. Next we seek to find the subset of these pairs that generate relative velocities entering the radius of

collision. Recall that in this PQW reference frame the velocities $\dot{x}_1, \dot{y}_1$, are given by (reference)

$$\dot{x}_1 = -\sqrt{\frac{\mu}{a_1(1 - e_1^2)}} \sin\left(f_1\right) \tag{5.25a}$$

$$\dot{y}_1 = \sqrt{\frac{\mu}{a_1(1 - e_1^2)}} \left(e_1 + \cos\left(f_1\right)\right) \tag{5.25b}$$

Substituting equation (5.24) into equations (5.25a), (5.25b) and letting $c = \cos f$ and $s = \sin\left(f_1\right)$ we obtain.

$$\dot{x}_1 = -\sqrt{\frac{\mu}{(r_1 + e_1 x_1)}} s \tag{5.26a}$$

$$\dot{y}_1 = \sqrt{\frac{\mu}{(r_1 + e_1 x_1)}} \left(e_1 + c\right) \tag{5.26b}$$

At this point we would like to find all of the values for e_1 such that $\hat{r} \cdot \boldsymbol{V} \leq 0$. Recall that $\hat{r}$ was specified when we chose a point (x_1, y_1) on the circle specified in equation (5.23) and that $\boldsymbol{V} = \boldsymbol{V}_1 - \boldsymbol{V}_2$ where $\boldsymbol{V}_2$ is fixed for the given quadrature point. Therefore all e_1 resulting in a collision satisfy the equation

$$\hat{r} \cdot \boldsymbol{V}_1 \leq \hat{r} \cdot \boldsymbol{V}_2 \tag{5.27a}$$

$$\hat{r} \cdot \boldsymbol{V}_1 \leq k_0 \tag{5.27b}$$

$$-\hat{r}_x \sqrt{\frac{\mu}{(r_1 + e_1 x_1)}} s + \hat{r}_y \sqrt{\frac{\mu}{(r_1 + e_1 x_1)}} \left(e_1 + c\right) \leq k_0 \tag{5.27c}$$

Where the constant $k_0 = \hat{r} \cdot \boldsymbol{V}_2$. Next we multiply both sides by the denominator which is strictly positive for elliptical orbits.

$$-\hat{r}_x \sqrt{\mu} s + \hat{r}_y \sqrt{\mu} \left(e_1 + c\right) \leq k_0 \sqrt{(r_1 + e_1 x_1)} \tag{5.28}$$

$$-\hat{r}_x \sqrt{\mu} s + \hat{r}_y \sqrt{\mu} \left(e_1 + c\right) - k_0 \sqrt{(r_1 + e_1 x_1)} \leq 0 \tag{5.29}$$

If we define constants $k_1 = \hat{r}_x \sqrt{\mu}$ and $k_2 = \hat{r}_y \sqrt{\mu}$ the the equation becomes

$$k_2 e_1 - k_0 \sqrt{(r_1 + e_1 x_1)} + (k_2 c - k_1 s) \leq 0 \qquad (5.30)$$

The equation above has two roots

$$e_1 = \frac{k_0^2 x_1 - 2k_2(k_2 c - k_1 s) \pm k_0 \sqrt{4k_2^2 r_1 + k_0^2 x_1^2 - 4k_2 x_1(k_2 c - k_1 s)}}{2k_2^2} \qquad (5.31)$$

Unfortunately, without specific values for the coefficients we cannot say if this equation will give a real maximum or minimum value for e_1. However, once an integration node is selected, the coefficients will be determined and it will be easy to know if the valid root from (5.31) is a maximum or a minimum. This inequality on e_1 combined with equation (5.24) then gives the (a, e) pairs of all of the states with a given (x_1, y_1) with velocities entering the sphere of collision. One minor problem is presented by the nonlinear relationship between e_1 and a_1. This can be remedied however, if the planar uncertainty in S_1 is described in modified equinoctial orbital elements (MEq OE) (p_1, f_1, g_1, L_1) [126].

Recall that in terms of the MEq OE we have

$$r = \frac{p}{1.0 + f \cos(L) + g \sin(L)} \qquad (5.32a)$$

$$x = r \cos(L) \qquad (5.32b)$$

$$y = r \sin(L) \qquad (5.32c)$$

$$\dot{x} = \sqrt{\frac{\mu}{p}}(-g - \sin(L)) \qquad (5.32d)$$

$$\dot{y} = \sqrt{\frac{\mu}{p}}(f + \cos(L)) \qquad (5.32e)$$

such that rearranging (5.32a) and substituting in the constants (r_1, x_1, y_1) for a given grid point

107

we get

$$r_1 + f x_1 + g y_1 = p \qquad (5.33)$$

With unknowns f, g and p forming a plane in three dimensional space. If we also place fixed integration nodes along p, then for a given p_j we have

$$g = -\frac{x_1}{y_1} f + (p_j - r) \qquad (5.34)$$

This gives a linear relation between the remaining unknowns f and g. To find the f and g that result in relative velocities less than zero we again look at the dot product between the relative position and velocity vectors for satellites S_1 and S_2. Substituting equations (5.32d) and (5.32e) into (5.27b) we obtain the following.

$$\sqrt{\frac{\mu}{p_j}} \left(-\hat{r}_x(g + \sin(L)) + \hat{r}_y(f + \cos(L)) \right) \leq k_0 \qquad (5.35)$$

Collecting the constants and solving for g in terms of f yields

$$g \geq \frac{\hat{r}_y}{\hat{r}_x} f + \frac{C}{\hat{r}_x} \qquad (5.36)$$

where $C = (\hat{r}_y \cos(L) - \hat{r}_x \sin(L)) - \sqrt{\frac{p_j}{\mu}} k_0$. The inequality above flips of course if $\hat{r}_x < 0$ or reduces to a simple inequality on f if $\hat{r}_x = 0$.

Since g is also constrained by (5.34), we can substitute this into (5.36) to get an inequality on f.

$$f \geq \left((p_j - r) - \frac{C}{\hat{r}_x} \right) \Big/ \left(\frac{\hat{r}_y}{\hat{r}_x} - \frac{x_1}{y_1} \right) \qquad (5.37)$$

Here the denominator has been assumed to be positive, which yields a maximum bound on f. If the denominator is negative, this expression will yield a minimum bound on f.

At this point we have clearly defined the subset of all the orbital elements from S_1's distribution

that will be within a radius of collision and have a negative relative velocity with respect to a given grid point from S_2's distribution. To compute the probability of collision, we must now integrate the PDF of S_1 over this set of states Λ_t multiplied into the relative velocity along the relative position vector $|v_r \cdot \hat{r}_r|$ and then integrate over time as shown in equation (5.22). In the general case this must be done using numerical quadrature techniques. Some simplification is possible if the distribution of S_1 in orbital element space is Gaussian.

Suppose that the distribution of $\boldsymbol{q}_1 = [p, f, g, L]^T$ at time $t \in [t_a, t_b]$ is given by

$$N\big(\bar{q}_1(t), Q_1(t)\big) \tag{5.38}$$

Having chosen a given grid point from Figure 5.3, it is seen that

$$N\big(\bar{q}_1(t), Q_1(t)\big) = N\big(\bar{L}_1(t), C\big) N\big(\bar{q}_1^*(t), Q_1^*(t)\big) \tag{5.39}$$

where $\boldsymbol{q}_1' = [p, f, g]^T$ and

$$Q_1 = \begin{bmatrix} A & B \\ B^T & C \end{bmatrix}$$

therefore, $\bar{\boldsymbol{q}}_1^* = \boldsymbol{q}_1' - BC^{-1}$ and $Q_1^* = A - BC^{-1}B^T$. This shift in the mean and covariance of $\boldsymbol{q}_1^*$ for a fixed L is of course the conditional PDF of $\boldsymbol{q}_1'$ given L. The vector $\boldsymbol{q}_1^*$ and its conditional distribution are both in $\mathbb{R}^3$. However, when a S_1 grid point (x_1, y_1) is chosen from Figure 5.3 the vector $\boldsymbol{q}_1'$ is constrained to lie in a two dimensional plane according to equation (5.33). The problem is that the distribution for $\boldsymbol{q}_1^*$ is only conditioned on a fixed L, when in reality, when choosing a S_1 grid point, both r_1 and L_1 become fixed. Thus we must condition the PDF further for fixed r_1.

Notice from equation (5.33) that the the normal vector of the plane containing valid $\boldsymbol{q}_1'$ is given by $\boldsymbol{n} = [1, -x, -y]^T$, which is constant for a given r_1. If the distribution of $\boldsymbol{q}_1^*$ is resolved into normal and planar components, it is easy to see that all states that satisfy equation (5.33) will have a constant offset from the mean along the normal direction. Since the normal component is constant

for any point on the plane, it is convenient to compute the normal offset of $\boldsymbol{q}_1' = [r, 0, 0]^T$, which is where the plane intersects the p axis. We will then use this offset as an additional condition on the distribution.

Let $\boldsymbol{e}_1 \equiv \hat{\boldsymbol{n}}$. We then define a vector $\boldsymbol{e}_2 = \hat{p} \times \boldsymbol{e}_1$ where $\hat{p} = [1, 0, 0]^T$. Since $\boldsymbol{e}_2 \perp \boldsymbol{e}_1$ it is guaranteed to lie in the plane defined by constant r. Finally the orthogonal triad is completed by taking $\boldsymbol{e}_3 = \boldsymbol{e}_1 \times \boldsymbol{e}_2$. An orthogonal matrix is then defined that maps vectors from the $[p, f, g]$ axes into the $\boldsymbol{e}$ frame such that $R_i = \hat{\boldsymbol{e}}_i^T$.

$$
R = \begin{bmatrix} 1/m_1 & -x_1/m_1 & -y_1/m_1 \\ 0 & y_1/r_1 & -x_1/r_1 \\ r_1/m_1 & x_1/(r_1 m_1) & y_1/(r_1 m_1) \end{bmatrix} \tag{5.40}
$$

where $m_1 = \sqrt{(1 + r_1^2)}$. The normal offset from the mean to the plane of constant r can now be given as

$$
n_c - \bar{n} = \hat{\boldsymbol{e}}_1^T R^T R(r\hat{p} - \bar{\boldsymbol{q}}_1^*) = \hat{\boldsymbol{e}}_1^T (r\hat{p} - \bar{\boldsymbol{q}}_1^*) \tag{5.41}
$$

The relation between the $\boldsymbol{e}$ frame and the $[p, f, g]$ frame is visualized in Figure 5.4 where the components of the vector $\boldsymbol{\xi} = [n, s_1, s_2]^T$ lie along the $\boldsymbol{e}_1$, $\boldsymbol{e}_2$, and $\boldsymbol{e}_3$ axis respectively.

The mean and covariance of the distribution in this new coordinate frame is given by applying the R such that $\bar{\boldsymbol{\xi}} = R\bar{\boldsymbol{q}}_1^*$ and $Q_\xi = RQ_1^* R^T$. In the same manner as before, this Gaussian distribution in $\mathbb{R}^3$ is conditioned on the event that $n = n_c$ to yield a conditional distribution on (s_1, s_2) in $\mathbb{R}^2$.

$$
N(\boldsymbol{\xi}, \bar{\boldsymbol{\xi}}, Q_\xi) = N(n_c, \bar{n}, Q_n) N(\boldsymbol{s}, \bar{\boldsymbol{s}}, Q_s) \tag{5.42}
$$

where $\bar{n} = \hat{\boldsymbol{e}}_1^T \bar{\boldsymbol{\xi}}$.

Any $\boldsymbol{s}$ from this distribution will automatically satisfy the constraint that (r_1, L_1) have been fixed. To see which $\boldsymbol{s}$ satisfy the velocity constraint in (5.27b) we express the result in (5.35) in
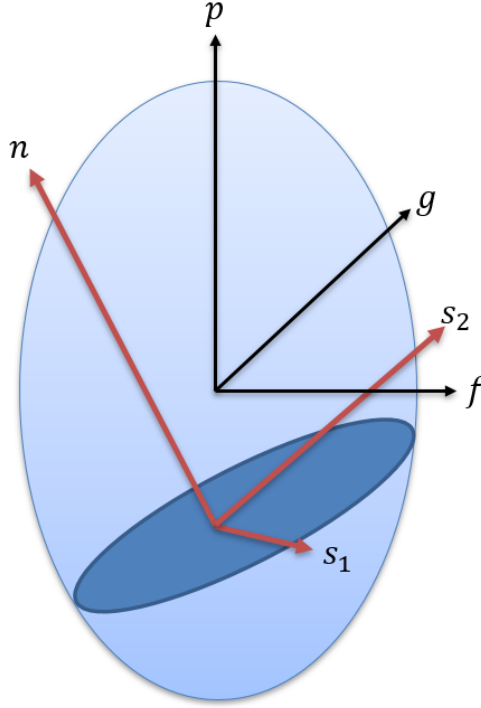
Figure 5.4: New Coordinate System Defined with Respect to Plane of Constant r_1 in $[p, f, g]$ Space.

terms of s_1, s_2 and the constant n_c using the following relations.

$$p = R_{11}n_c + R_{21}s_1 + R_{31}s_2 \tag{5.43a}$$

$$f = R_{12}n_c + R_{22}s_1 + R_{32}s_2 \tag{5.43b}$$

$$g = R_{13}n_c + R_{23}s_1 + R_{33}s_2 \tag{5.43c}$$

Note that the first term on the right hand side of each expression above is constant with respect to s_1, s_2 and that $R_{21} = 0$ from the definition of R in (5.40). Plugging these substitutions into equation (5.35) yields

$$s_1 \leq \cfrac{\left(-s_2(\hat{r}_y R_{32} - \hat{r}_x R_{33}) - \hat{r}_y\big(R_{13}n_c + \cos(L)\big) - \hat{r}_x\big(R_{13}n_c + \sin(L)\big)\right)}{(\hat{r}_y R_{22} - \hat{r}_x R_{23})}$$
$$+ \cfrac{k_0}{\sqrt{\frac{\mu}{(R_{11}n_c + R_{31}s_2)}}(\hat{r}_y R_{22} - \hat{r}_x R_{23})} \qquad (5.44)$$

where the inequality flips if $(\hat{r}_y R_{22} - \hat{r}_x R_{23}) < 0$. In this expression $\hat{r}_x, \hat{r}_y$ are the x and y components of the vector $\boldsymbol{\rho}$ from Figure 5.3. The distribution of s_1, s_2 is then integrated over the region bounded by the curve given in equation (5.44).

It is important to note that this derivation in MEq orbital elements did not assume that the argument of perigee was fixed, as it would have been if all of the uncertainty from S_1's argument of perigee had been projected onto the relative right ascension of the ascending node. As such this method for computing P_c is also capable of analysing general conjunctions between two satellites in the same plane.

Once the PDF has been integrated over s_1, s_2 for each grid point in Figure 5.3, it still needs to be integrated over L and n. While one could do this directly, it will be easier to use a polar coordinate system centered at $(x_2, y_2, z = 0)$ as illustrated in Figure 5.5.
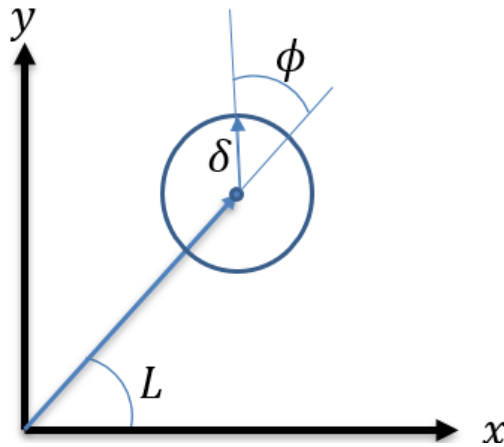
Figure 5.5: Polar Coordinates for Integration Over L, n.

Where again $\delta^2 = R_c^2 - z_2^2$. Integrating over δ, ϕ will require us to include the determinant of the Jacobian to account for the change in volume where $n_c = \frac{r_1}{\sqrt{(1+r_1^2)}}$ and $L = \arctan\left(\frac{y_2}{x_2}\right) + \arctan\left(\frac{\delta \sin(\phi)}{R+\delta \cos(\phi)}\right)$ and $r = \sqrt{(\delta \sin(\phi))^2 + (R + \delta \cos(\phi))^2}$.

5.2.5 Example using Transient Solution

It will be helpful now to put all the theory from the previous section to work on a simple example. Let $\boldsymbol{q}_r = [p_2, f_2, g_2, L_2, h_r, k_r]$ be distributed according to the dirac delta distribution [148] and $\boldsymbol{q}_1$ be distributed normally $\boldsymbol{q}_1 \sim N\big(\boldsymbol{q}_1(t), \bar{\boldsymbol{q}}_1(t), Q_1(t)\big)$. If $\boldsymbol{q}_r$ is not distributed according the dirac delta function, then apply the results of this example at each quadrature point from the integration over $\boldsymbol{q}_r$. Plugging these distributions into equations (5.22) we obtain

$$P_c = \int_{t_a}^{t_b} \int_{\Lambda_\tau} N\big(\boldsymbol{q}_1(\tau), \bar{\boldsymbol{q}}_1(\tau), Q_1(\tau)\big) d\boldsymbol{q}_1 \tag{5.45}$$

For convenience let $\boldsymbol{q}_1 = [L_1, p_1, f_1, g_1]^T$, now we apply the linear transformation from equation (5.40) to obtain $\boldsymbol{\eta} = [L_1, n, s_1, s_2]^T$ and we have.

$$P_c = \int_{t_a}^{t_b} \int_{\Lambda_\tau} N\big(\boldsymbol{\eta}_1(\tau), \bar{\boldsymbol{\eta}}_1(\tau), Q_{\eta_1}(\tau)\big) dp\, df\, dg\, dL \tag{5.46}$$

Now instead of integrating over p, f, g, L we desire to integrate over ρ, s_1, s_2, ϕ as previously discussed where $dp\, df\, dg\, dL = \det(J)\, ds_1\, ds_2\, d\rho\, d\phi$ and the Jacobian is given in Einstein notation as

$$J_{ij} = R_{im,j}^T \boldsymbol{\eta}_m + R_{im}^T \boldsymbol{\eta}_{m,j} \tag{5.47}$$

where the $,j$ means take a derivative with respect to the jth component of the vector $\boldsymbol{X}$ where $\boldsymbol{X} = [\rho, \phi, s_1, s_2]^T$. In general this Jacobian is a function of s_1 and s_2 which can impede the analytical integral over s_1. However, the determinant of the Jacobian is well approximated if evaluated at $\bar{s}_1$. The Jacobian can simplify even further for low eccentricity orbits. For orbits of

low eccentricity the determinate of J is approximately

$$\det(J) \approx \frac{\rho}{r\sqrt{(1+r^2)}} \tag{5.48}$$

From (5.44) let the numerator be called $-\beta(n, s_2)$ and the denominator be called $\omega(n, s_2)$ such that $\Delta \boldsymbol{r} \cdot \Delta \boldsymbol{v} = s_1 \omega(n, s_2) + \beta(n, s_2)$. These expressions are then plugged into the P_c integral to obtain

$$P_c = \int_{t_a}^{t_b} \int_{\Lambda_\tau} N\big(\boldsymbol{\eta}_1(\tau), \bar{\boldsymbol{\eta}}_1(\tau), Q_{\eta_1}(\tau)\big) \frac{\rho}{r\sqrt{(1+r^2)}} \big(s_1 m(n, s_2) + b(n, s_2)\big) ds_1 ds_2 d\phi dt \tag{5.49}$$

where n, r are functions of ρ, ϕ and t.

Next, we wish to resolve the distribution into the product of conditional distributions

$$N\big(\boldsymbol{\eta}_1(\tau), \bar{\boldsymbol{\eta}}_1(\tau), Q_{\eta_1}(\tau)\big) = N\big(\boldsymbol{p}(\tau), \bar{\boldsymbol{p}}(\tau), Q_p(\tau)\big) N\big(s_2'(\tau_i), \bar{s}_2'(\tau_i), \sigma_{s_2'}(\tau_i)\big) * \\ N\big(s_1''(\tau_i), \bar{s}_1''(\tau_i), \sigma_{s_1''}(\tau_i)\big) \tag{5.50}$$

where $\boldsymbol{p} = [L_1(\delta, \phi), n_c(\delta, \phi)]^T$, $\bar{\boldsymbol{p}} = [\bar{L}_1, \bar{n}]$ and $Q_\eta = \begin{bmatrix} Q_p & B^T \\ B & Q_s \end{bmatrix}$. These are used to find

$\begin{bmatrix} s_1' \\ s_2' \end{bmatrix} = \begin{bmatrix} s_1 \\ s_2 \end{bmatrix} - BQ_p^{-1}\boldsymbol{p}$ and $\bar{\boldsymbol{s}}' = \boldsymbol{s} - BQ_p^{-1}\bar{\boldsymbol{p}}$. Hence, $\begin{bmatrix} \sigma_{s_1'} & b \\ b & \sigma_{s_2'} \end{bmatrix} = \begin{bmatrix} Q_s - BQ_p^{-1}B^T \end{bmatrix}$ and

$\sigma_{s_1''} = \sigma_{s_1'} - \frac{b^2}{\sigma_{s_2'}}\sigma_{s_2'}$ with $s_1'' = s_1' - \frac{b}{\sigma_{s_2'}}s_2'$ and $\bar{s}_1'' = \bar{s}_1' - \frac{b}{\sigma_{s_2'}}\bar{s}_2'$. The details behind splitting the normal distribution this way are presented in appendix B.

With each term in equation (5.50) defined we are ready to integrate to find P_c. The quadrature over t, ϕ and s_2' are handled using numerical quadrature while the integration over s_1'' can be computed analytically.

$$P_{s_1} = \int_{-\infty}^{s^*} -N\big(s_1''(\tau_i), \bar{s}_1''(\tau_i), \sigma_{s_1''}(\tau_i)\big) \big(s_1'' \omega(n, s_2) + \beta''(n, s_2)\big) ds_1'' \tag{5.51}$$

where $s^* = -\beta/\omega$ is the limit of integration, $\beta'' = \beta + \omega(\frac{b}{\sigma_{s_2'}}s_2' + \mathbf{1}^T BQ_p^{-1}\mathbf{p})$ and $\mathbf{1}^T = [1, 0]$. The negative sign is because $\Delta\mathbf{v} \cdot \Delta\mathbf{r} \leq 0$ over this range. Evaluating this integral yields

$$P_{s_1} = \frac{1}{2}(\omega\bar{s}_1'' + \beta'')\left[1 + \lambda\operatorname{erf}\left(\frac{(s^* - \bar{s}_1'')}{\sqrt{(2\sigma_{s_1''})}}\right)\right] + \lambda\omega\frac{\sqrt{\sigma_{s_1''}}}{2\pi}\exp\left(-\frac{(s^* - \bar{s}_1'')^2}{2\sigma_{s_1''}}\right) \qquad (5.52)$$

In the expression above $\lambda = sign(\omega)$ and accounts for the flip of the inequality in equation (5.44) if $\omega < 0$. The integration over the remaining three dimensions is fairly standard. Using Gaussian quadrature we integrate over $t \in [t_a, t_b]$, $\phi \in [0, 2\pi]$ and $s_2' \in [\bar{s}_2' - 6\sqrt{\sigma_{s_2'}}, \bar{s}_2' + 6\sqrt{\sigma_{s_2'}}]$ to obtain P_c. This is done for a number of test cases in the results section.

5.3   Results

The steady state P_c for the special case when the point of closest approach is assumed to occur along the line of relative nodes and the distributions are normal in orbital element space was already demonstrated as a prefiltering technique in Chapter 4. This bound on the P_c was then tightened by considering the angular displacement from the relative line of nodes. This upper bound for a single pass is demonstrated on test cases (I - III, VI,VII) from Chapter 3 and is compared to the steady state P_c and the actual P_c for that single pass in Table 5.1.

Table 5.1: $\|P_c\|_\infty$ vs The Single Pass Method vs The Transient Solution.

	P_{c_∞}	P_{c_∞} (single pass)	CRATER P_c
TCI	2E-2	4.6E-4	2.76E-4
TCII	6E-3	6.3E-5	5.97E-5
TCIII	3E-1	1.5E-3	9.89E-4
TCVI	1E-3	1.7E-4	1.21E-5
TCVIII	1E-2	6.6E-6	2.18E-11

Next we look at what happens to the P_c over time. For this result we took the collision from CRATER test case I with the initial covariances for both satellites scaled by $(1/160)$ and computed the P_c at each close approach, which occur every half orbit. The P_c for each close approach is

computed independently using the CRATER algorithm. This method will eventually over estimate the bound since is does not account for correlation between subsequent close approaches. This is shown in Figures 5.6 and 5.7.
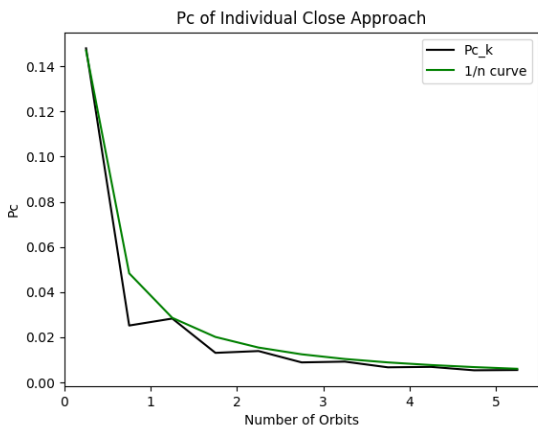
Figure 5.6: Close Approach P_c Decaying as 1/n as Distribution Becomes Stretched in Along Track Direction.
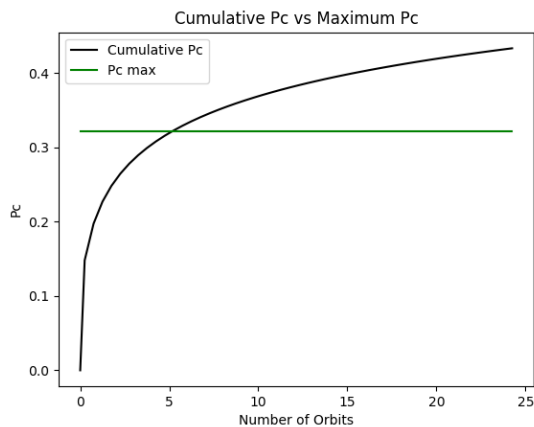
Figure 5.7: Cumulative P_c Soon Exceeds the Predicted Maximum P_c Due to Correlation Between Subsequent Passes.

The final set of results demonstrates the method of computing the transient P_c in terms of the orbital elements. The orbital element method was used to compute the P_c for five different test cases and is compared to a Monte Carlo solution. To facilitate comparison only unperturbed Keplerian dynamics are considered.

The results for each test case include P_c as computed by the orbital element method as well as the Monte Carlo solution and the percent error between the solutions. The bounding epsilon as predicted by the Chernoff Hoeffding bound [104] is also included and shows the 95% confidence bound as a percentage of the reported MC result. A more extensive discussion on Monte Carlo bounds can be found in Chapter 2. Both algorithms were run in serial on a single thread. It should be noted however that both of these algorithms can be implemented with a parallel architecture. The Monte Carlo solution will be referred to as the MC result while the orbital element solution will be called the ROE result. Since the interest was in validating the P_c integral portion of the

algorithm, the MC samples were propagated using the state transition matrix (STM) in orbital element space, so that both the MC and ROE results would use the same method for propagating the distribution forward in time.

The first test case considered was a variant of test case I from Chapter 3. The initial covariance for satellite 1 was scaled by $\frac{1}{160}$ and the distribution for satellite 2 was taken to be the Dirac delta distribution centered at the mean. Next, the uncertainty in satellite 1's orbit was limited to planar uncertainty in the p, f, g, L orbital elements. This was accomplished by mapping the propagated covariance matrix in orbital element space with R_p. Where R_p is a 4×6 matrix such that $[p, f, g, L]^T = R_p[p, f, g, h, k, L]^T$.

Table 5.2: Results Test Case I (OE Method).

	ROE	MC	% Error	C-H ϵ
PC	4.28E-2	4.31E-2	0.60 %	4.1 %
Time	11.4 sec	95.3 sec		

While the ROE result is nearly an order of magnitude faster for this test case (see Table 5.2). It must be remembered that one of the distributions was taken as the Dirac delta and the MC samples were linearly propagated using the STM.

The next four test cases are different from the first test case in that both satellites are in the same orbital plane. The initial conditions are given in terms of Kepler orbital elements [134] and the uncertainty is given in Cartesian with SI units (km,s). The tabulated initial condition in Table 5.3 were mapped into MEq OE for use in the ROE algorithm. The mean was mapped using the exact algebraic relation while the covariance was linearly mapped.

The conjunction window under consideration for test cases Ip, IIp, IVp is $0.5T_2$ after epoch, where T_2 is the orbital period for satellite 2. For test case IIIp the screening period is about $1.0T_2$ after epoch.

Again the results for these test cases agree closely with the Monte Carlo results (see Table 5.4).

Table 5.3: Initial Conditions Planar Test Case.

Tc Ip	a (km)	e	ω (deg)	ν (deg)	(σ_x^2, σ_y^2)	$(\sigma_{v_x}^2, \sigma_{v_y}^2)$	$R_c = 0.04$ (km)
Sat1	7000	0.001	0	53.1164	6.25E-5	6.25E-8	
Sat2	1000	0.3	0	180	0	0	
Tc IIp	a (km)	e	ω (deg)	ν (deg)	(σ_x^2, σ_y^2)	$(\sigma_{v_x}^2, \sigma_{v_y}^2)$	$R_c = 0.1$ (km)
Sat1	7000	0.001	0.3	53.1164	6.25E-5	6.25E-8	
Sat2	1000	0.3	0	180	0	0	
Tc IIIp	a (km)	e	ω (deg)	ν (deg)	(σ_x^2, σ_y^2)	$(\sigma_{v_x}^2, \sigma_{v_y}^2)$	$R_c = 0.5$ (km)
Sat1	7000	1.0E-7	0	-197.224	1.0E-6	1.0E-7	
Sat2	24500	0.7142857	0	0	0	0	
Tc IVp	a (km)	e	ω (deg)	ν (deg)	(σ_x^2, σ_y^2)	$(\sigma_{v_x}^2, \sigma_{v_y}^2)$	$R_c = 1.0$ (km)
Sat1	28000	0.001	0	53.1164	6.25E-5	6.25E-8	
Sat2	40000	0.3	0	180	0	0	

This is because both methods are using the the STM to propagate the initial distribution. Because both satellites are coplanar in these test cases the length of the close approach was greater than in test case I. The Monte Carlo algorithm for these cases does not use a polynomial approximation to find the point of closest approach, but decreases the time step such that the relative velocity multiplied into the time step results in a distance less than R_c. This feature combined with the longer collision window is responsible for the longer Monte Carlo run times compared to test case I. Based on the run times in Table 5.4, it is anticipated that the ROE method would have about the same run time for these test cases as the MC and would be faster than MC at lower P_c values.

5.4 Conclusions

An investigation into the idealized long term behaviour of the state uncertainty lead to an expression of the steady state distribution in orbital element space. This distribution was seen to reflect the truths predicted by Keplers Law that orbiting objects spend most of their time at apoapsis.

Looking at the probability of collision as time goes to infinity revealed that the maximum achievable P_c between two satellites is equivalent to finding the probability that the minimum close approach miss distance between any two trajectories is less than R_c. This yields a P_c that

Table 5.4: Results Planar Test Cases.

Tc Ip	ROE	MC	% Error	C-H ϵ
PC	11.63E-2	11.63E-2	0.0 %	1.5 %
Time	3.5 sec	397 sec		
Tc IIp	ROE	MC	% Error	C-H ϵ
PC	5.128E-2	5.13E-2	0.25 %	1.7 %
Time	3.5 sec	396 sec		
Tc IIIp	ROE	MC	% Error	C-H ϵ
PC	54.78E-2	54.76E-2	0.03 %	1.1 %
Time	3.6 sec	395 sec		
Tc IVp	ROE	MC	% Error	C-H ϵ
PC	40.28E-2	40.28E-2	0.0 %	1.5 %
Time	3.5 sec	396 sec		

is conservative by about two orders of magnitude when trying to bound the P_c for a single close approach in the cases studied. By also considering the probability that the true anomaly satisfies conservative conditions for for a collision this bound can be reduced to give a ball park estimate of the P_c for a given close approach. This approach lacks the accuracy of formal P_c analysis but is easily computed for general distributions and may be useful as a filtering technique.

Finally, the transient solution was reformulated in terms or the Kepler and MEq orbital elements. This formulation solves a long standing difficulty of needing to map PDF's from the relatively well behaved orbital element space to the Cartesian space for conjunction analysis. This approach was then verified against test cases in three and two dimensions and was seen to have a high level of agreement with the Monte Carlo P_c solution. This was in part due to the Monte Carlo using the same uncertainty propagation method. The run times indicate that the cost of the high dimension numerical quadrature is significant and that the new ROE method will likely be similar in run time for high probability P_c, but may be significantly faster for lower P_c collision scenarios due to the high number of MC samples needed to verify these cases.

6. SUMMARY AND CONCLUSIONS

6.1 Research Objectives

Recall that the scope of this research is to build upon and contribute to the existing 28+ years of literature on conjunction analysis in novel and meaningful ways. This has been achieved through a successful pursuit of the following objectives.

1. Identify and exploit quasi linear sub-spaces in algebraic and differential equation mappings of the probability density function associated with the orbital state uncertainty to improve algorithm performance

   The NL index was used to identify a quasi linear subspace of the propagated orbital element PDF along 5 of its 6 eigenvectors. This stressed the importance of identifying the eignefiber for improving algorithm performance.

2. Take into account collision geometry and demonstrate its importance

   Collision geometry was shown to be vital in selecting between the local Gaussian and Gaussian mixture approximation schemes.

3. Use the eigenvectors of the distribution in orbital element space to build efficient PDF approximations in Cartesian space

   Use of the NL index along the eigenvectors of the covariance matrix in orbital element space showed that non linearity was greatest along the eigenfiber resulting in a PDF approximation scheme that place local linearizations along this direction. This mitigated the problem of high dimensional PDF approximations while capturing to great fidelity the nonGaussian PDF in Cartesian space.

4. Allow for parametric model uncertainty

   Model uncertainty was seen to have large effects on the computed PC and was incoporated into CRATER by appending the uncertain parameters onto the state vector.

5. Use the Liouville equation to quantify the error in approximations

   The Liouville equation was used to quatify the pointwise error in assuming the orbital element pdf was Gaussian. This error was computed alonge each eigen vector of the covaraince matrix revealing that the error is siginifcantly higher along the eigenfiber.

6. Combine these techniques and insights into single software tool

   The CRATER collision risk assessment tool was developed and compared against contemporary and traditional conjunction analysis algorithms. It was seen to provide an order of magnitude speed up while maintaining accuracy on highly nonlinear problems.

7. Explore the consequences of coordinate choice

   The formulation of the P_c integral in spherical coordinates in either 2D or 3D proved to provide significant accuracy benefits when compared to Cartesian algorithms using linear analysis.

8. Explore collisions in the orbital element space

   The introduction of the relative orbital elements helped identify where collisions take place in orbital element space and led to new risk quantification and prefiltering techniques.

9. Develop new formulations for computing the probability of collision that can be evaluated in orbital element space

   Using the relative orbital elements we were able to derive an expression for the probability of collision in terms of the modified equinoctial orbital elements; constituting a major contribution to the understanding of colliding objects in space.

10. Explore the validity, accuracy, and computational merit of the algorithms and compare to the best available pre-existing approaches

    The approaches outlined in this dissertation were compared against both short and long encounter P_c methods, adaptive GMM methods and two different Monte Carlo methods. These

121

comparison revealed that no single method was superlative across all collision scenarios. This insight motivated the adaptive strategy of the CRATER algorithm to use collision geometry and quantification of the nonlinear of mappings to ensure each P_c method was only when appropriate. This led to an algorithm that was about an order of magnitude faster than the next best semi analytical method over a large number of nonlinear collision scenarios.

6.2 Challenges

The work presented in this dissertation demonstrated several key advancements in the area of conjunction analysis; nevertheless, there are several remaining challenges. Recall that the scope of the P_c problem extends beyond the work of this dissertation and includes the areas of measurements, catalog maintenance, as well as processes for communicating satellite state uncertainty and P_c to operators. Most of these are processes that go into providing the initial conditions for P_c algorithms. It is important that these initial conditions are highly accurate with uncertainties that account for the model error in the measurements and the propagation, since any further conjunction analysis will only be as accurate as these initial conditions. The accuracy of these initial condition may come into question if standard propagation techniques such as sgp-4 [16] have been used in updating the mean and covariance .

Another area of challenge is in implementing these algorithms as part of flight software. Many satellites are concerned with computing P_c as part of their on board guidance, navigation, and control, but are limited by size, weight, and power constraints. This has resulted in many flight algorithms resorting to pseudo risk measures such as the Mahalonobis distance. While the linearization techniques presented in Chapter 3 greatly simplify non-linear P_c analysis. It is yet to be seen how well these perform, especially in missions featuring close proximity relative motion and in cases where the conops may require the conjunction analysis to model the spacecraft with more fidelity than a simple sphere.

Furthermore, many satellites in constellations undergo relative oscillatory motion with respect to one another. This stresses the assumption made in traditional long encounter P_c analysis, which assumes that trajectories shall only have a single close approach within the analysis window.

6.3   Further Study

The orbital element method for computing P_c significantly reduces the burden on uncertainty propagation by keeping the P_c analysis in the orbital element space. This technique is limited in usefulness however by the need to numerically integrate over many dimensions. Further study into the improved numerical methods for this algorithm and possible simplifying assumptions that could be made could greatly expand this techniques potential.

The CRATER algorithm presented a method for obtaining a point wise check against the Liouville solution. While this is likely good enough, further efforts to expand this technique to obtain an estimate of the global convergence could be much more assertive in negating the need for a redundant Monte Carlo validation. After the methodology is fully validated against Monte Carlo, it is expected that all subsequent applications that satisfy a Liouville error metric will provide a much better way to ensure P_c accuracy. This issue is also relevant in cases where stochastic model noise is deemed necessary to the analysis. In such cases, the governing Fokker-Planck-Kolmogorov equation would need to be satisfied by the propagated PDF and the process noise would need to be included in the PDF propagation.

Finally the P_c formulation that results from long encounter analysis is such that it could be directly implemented into feedback laws or trajectory optimization. This would allow trajectory planners and guidance algorithms to build risk mitigation directly into the trajectories.

REFERENCES

[1] ESA Space Debris Office, "ESA's Annual Space Environment Report," Tech. Rep. GEN-DB-LOG-00271-OPS-SD, European Space Operations Centre, Robert-Bosch-Strasse 5, D-64293 Darmstadt, Germany, 2019. Revision 3.2.

[2] M. Yakovlev, "The IADC Space Debris Mitigation Guidelines and Supporting Documents," in *4th European Conference on Space Debris*, vol. 587, p. 591, 2005.

[3] N. L. Johnson, E. Stansbery, J. C. Liou, M. Horstman, C. Stokely, and D. Whitlock, "The Characteristics and Consequences of the Break-Up of the Fengyun-1C Spacecraft," *Acta Astronautica*, vol. 63, no. 1-4, pp. 128–135, 2008.

[4] T. Wang, "Analysis of Debris from the Collision of the Cosmos 2251 and the Iridium 33 Satellites," *Science & Global Security*, vol. 18, no. 2, pp. 87–118, 2010.

[5] D. J. Kessler and B. G. Cour-Palais, "Collision Frequency of Artificial Satellites: The Creation of a Debris Belt," *Journal of Geophysical Research: Space Physics*, vol. 83, no. A6, pp. 2637–2646, 1978.

[6] A. Guidotti, M. Caus, J. Bas, G. Colavolpe, T. Foggi, S. Cioni, A. Modenini, and D. Tarchi, "Satellite-enabled LTE systems in LEO Constellations," *2017 IEEE International Conference on Communications Workshops (ICC Workshops)*, pp. 876–881, 2017.

[7] O. Kodheli, A. Guidotti, and A. Vanelli-Coralli, "Integration of Satellites in 5G through LEO Constellations," in *GLOBECOM 2017-2017 IEEE Global Communications Conference*, pp. 1–6, IEEE, 2017.

[8] D. N. Baker and S. P. Worden, "The Large Benefits of Small-satellite Missions," *EOS, Transactions American Geophysical Union*, vol. 89, no. 33, pp. 301–302, 2008.

[9] M. Shan, J. Guo, and E. Gill, "Review and Comparison of Active Space Debris Capturing and Removal Methods," *Progress in Aerospace Sciences*, vol. 80, pp. 18–32, 2016.

[10] H. Schaub and Z. Sternovsky, "Active Space Debris Charging for Contactless Electrostatic Disposal Maneuvers," *Advances in Space Research*, vol. 53, no. 1, pp. 110–118, 2014.

[11] K. A. Cavalieri, B. Macomber, C. Moody, A. Probe, and J. L. Junkins, "Laboratory Experiments Supporting Autonomous Space Debris Mitigation," in *Proceedings of the 36th annual AAS rocky mountain section guidance and control conference*, vol. 149, pp. 3–16, 2013.

[12] C. K. Moody, A. B. Probe, A. Masher, T. Woodbury, M. Saman, J. Davis, and J. E. Hurtado, "Laboratory Experiments for Orbital Debris Removal," in *AAS Guidance, Navigation, and Control Conference. Breckenridge, CO*, vol. 12, 2016.

[13] K. Lee, C. Park, and S.-Y. Park, "Near-Optimal Continuous Control for Spacecraft Collision Avoidance Maneuvers via Generating Functions," *Aerospace Science and Technology*, vol. 62, pp. 65–74, 2017.

[14] L. Gremyachikh, D. Dubov, N. Kazeev, A. Kulibaba, A. Skuratov, A. Tereshkin, A. Ustyuzhanin, L. Shiryaeva, and S. Shishkin, "Space Navigator: A Tool for the Optimization of Collision Avoidance Maneuvers," *arXiv preprint arXiv:1902.02095*, 2019.

[15] R. W. Sturdevant, "From Satellite Tracking to Space Situational Awareness: The USAF and Space Surveillance, 1957-2007," *Air Power History*, vol. 55, no. 4, pp. 4–23, 2008.

[16] F. R. Hoots and R. L. Roehrich, "Models for Propagation of NORAD Element Sets," tech. rep., Aerospace Defense Command Peterson AFB CO Office Of Astrodynamics, 1980.

[17] H. L. Neal, S. L. Coffey, and S. Knowles, "Maintaining the Space Object Catalog with Special Perturbations," *Astrodynamics 1997*, pp. 1349–1360, 1997.

[18] K. Hill, K. Alfriend, and C. Sabol, "Covariance-Based Uncorrelated Track Association," in *AIAA/AAS Astrodynamics Specialist Conference and Exhibit*, p. 7211, 2008.

[19] J.-C. Liou, "Risk from Orbital Debris," in *RAS Specialist Discussion Meeting on Space Dust and Debris in the Vicinity of the Earth; London, UK*, 2018.

[20] J. A. Haimerl and G. P. Fonder, "Space Fence System Overview," in *Proceedings of the Advanced Maui Optical and Space Surveillance Technology Conference*, Curran Associates, Inc. Redhook, NY, 2015.

[21] G. Fonder, M. Hughes, M. Dickson, M. Schoenfeld, and J. Gardner, "Space Fence Radar Overview," in *2019 International Applied Computational Electromagnetics Society Symposium (ACES)*, pp. 1–2, IEEE, 2019.

[22] L. K. Newman and M. D. Hejduk, "NASA Conjunction Assessment Organizational Approach and the Associated Determination of Screening Volume Sizes," in *17th Annual Small Payload Rideshare Symposium; Laurel, MD*, 2015.

[23] A. J. Rosengren and D. J. Scheeres, "Long-Term Dynamics of High Area-to-Mass Ratio Objects in High-Earth Orbit," *Advances in Space Research*, vol. 52, no. 8, pp. 1545–1560, 2013.

[24] C. Früh and T. Schildknecht, "Variation of the Area-to-Mass Ratio of High Area-to-Mass Ratio Space Debris Objects," *Monthly Notices of the Royal Astronomical Society*, vol. 419, no. 4, pp. 3521–3528, 2012.

[25] C. Früh and M. K. Jah, "Coupled Orbit–Attitude Motion of High Area-to-Mass Ratio (HAMR) Objects Including Efficient Self-Shadowing," *Acta Astronautica*, vol. 95, pp. 227–241, 2014.

[26] G. Cook, "Satellite Drag Coefficients," *Planetary and Space Science*, vol. 13, no. 10, pp. 929–946, 1965.

[27] D. A. Vallado and D. Finkleman, "A Critical Assessment of Satellite Drag and Atmospheric Density Modeling," *Acta Astronautica*, vol. 95, pp. 141–165, 2014.

[28] J. Dolado-Perez, C. Pardini, and L. Anselmo, "Review of Uncertainty Sources Affecting the Long-Term Predictions of Space Debris Evolutionary Models," *Acta Astronautica*, vol. 113, pp. 51–65, 2015.

[29] A. Kolmogoroff, "Über die Analytischen Methoden in der Wahrscheinlichkeitsrechnung," *Mathematische Annalen*, vol. 104, no. 1, pp. 415–458, 1931.

[30] V. I. Bogachev, N. V. Krylov, M. Röckner, and S. V. Shaposhnikov, *Fokker-Planck-Kolmogorov Equations*, vol. 207 of *Mathematical Surveys and Monographs*. American Mathematical Soc., 2015.

[31] J. W. Gibbs, *Elementary principles in statistical mechanics*. Courier Corporation, 2014.

[32] M. Kumar, S. Chakravortyt, and J. L. Junkins, "On the Curse of Dimensionality in the Fokker-Planck Equation," *Advances in the Astronautical Sciences*, vol. 135, no. 3, pp. 1781–1800, 2009.

[33] H. Schaub and J. Junkins, *Analytical Mechanics of Aerospace Systems*. AIAA Education Series, 4th ed., 2018.

[34] R. E. Kalman, "A New Approach to Linear Filtering and Prediction Problems," *Transactions of the ASME–Journal of Basic Engineering*, vol. 82, no. Series D, pp. 35–45, 1960.

[35] R. E. Kalman and R. S. Bucy, "New Results in Linear Filtering and Prediction Theory," *Journal of basic engineering*, vol. 83, no. 1, pp. 95–108, 1961.

[36] G. L. Smith, S. F. Schmidt, and L. A. McGee, "Application of Statistical Filter Theory to the Optimal Estimation of Position and Velocity on Board a Circumlunar Vehicle," Tech. Rep. R-135, NASA, 1962.

[37] B. A. McElhoe, "An Assessment of the Navigation and Course Corrections for a Manned Flyby of Mars or Venus," *IEEE Transactions on Aerospace and Electronic Systems*, no. 4, pp. 613–623, 1966.

[38] D. G. Hoag, *Apollo Navigation, Guidance, and Control Systems: A Progress Report*. MIT Instrumentation Laboratory, 1969.

[39] R. Battin, *An Introduction to the Mathematics and Methods of Astrodynamics*. AIAA Education Series, 2014.

[40] D. K. Geller, "Linear Covariance Techniques for Orbital Rendezvous Analysis and Autonomous Onboard Mission Planning," *Journal of Guidance, Control, and Dynamics*, vol. 29, no. 6, pp. 1404–1414, 2006.

[41] N. B. Stastny and D. K. Geller, "Autonomous Optical Navigation at Jupiter: A Linear Covariance Analysis," *Journal of Spacecraft and Rockets*, vol. 45, no. 2, pp. 290–298, 2008.

[42] J. L. Junkins and P. Singla, "How Nonlinear Is It? A Tutorial on Nonlinearity of Orbit and Attitude Dynamics," *Journal of the Astronautical Sciences*, vol. 52, pp. 7–60, 2004.

[43] K. T. Alfriend and I. Park, "When Does the Uncertainty Become Non-Gaussian," in *Advanced Maui Optical and Space Surveillance Technologies Conference*, p. 46, 2016.

[44] J. L. Junkins, M. R. Akella, and K. T. Alfriend, "Non-Gaussian Error Propagation in Orbital Mechanics," *Advances in the Astronautical Sciences*, vol. 92, pp. 283–298, 1996.

[45] V. T. Coppola and S. Tanygin, "Using Bent Ellipsoids to Represent Large Position Covariance in Orbit Propagation," *Journal of Guidance, Control, and Dynamics*, vol. 38, no. 9, pp. 1775–1784, 2015.

[46] R. Weisman, M. Majji, and K. Alfriend, "Application of the Transformation of Variables Technique for Uncertainty Mapping in Nonlinear Filtering," *Celestial Mechanics and Dynamical Astronomy*, vol. 118, no. 2, pp. 129–164, 2014.

[47] C. Sabol, T. Sukut, K. Hill, K. T. Alfriend, B. Wright, Y. Li, and P. Schumacher, "Linearized Orbit Covariance Generation and Propagation Analysis via Simple Monte Carlo Simulations," in *Paper AAS 10-134 presented at the AAS/AIAA Space Flight Mechanics Conference, February*, pp. 14–17, 2010.

[48] Z. Zhang, "Parameter Estimation Techniques: A Tutorial with Application to Conic Fitting," *Image and vision Computing*, vol. 15, no. 1, pp. 59–76, 1997.

[49] R. S. Park and D. J. Scheeres, "Nonlinear Mapping of Gaussian Statistics: Theory and Applications to Spacecraft Trajectory Design," *Journal of guidance, Control, and Dynamics*, vol. 29, no. 6, pp. 1367–1375, 2006.

[50] K. Fujimoto, D. Scheeres, and K. Alfriend, "Analytical Nonlinear Propagation of Uncertainty in the Two-Body Problem," *Journal of Guidance, Control, and Dynamics*, vol. 35, no. 2, pp. 497–509, 2012.

[51] M. Majji, J. L. Junkins, and J. D. Turner, "A High Order Method for Estimation of Dynamic Systems," *The Journal of the Astronautical Sciences*, vol. 56, no. 3, pp. 401–440, 2008.

[52] M. Berz, "Modern Map Methods in Particle Beam Physics," *Adv. Imaging Electron Phys.*, vol. 108, pp. 1–318, 1999.

[53] M. Valli, R. Armellin, P. Di Lizia, and M. Lavagna, "Nonlinear Mapping of Uncertainties in Celestial Mechanics," *Journal of Guidance, Control, and Dynamics*, vol. 36, no. 1, pp. 48–63, 2012.

[54] A. Morselli, R. Armellin, P. D. Lizia, and F. B. Zazzera, "A High Order Method for Orbital Conjunctions Analysis : Sensitivity to Initial Uncertainties," *Advances in Space Research*, vol. 53, no. 3, pp. 490–508, 2014.

[55] S. J. Julier, J. K. Uhlmann, and H. F. Durrant-Whyte, "A New Approach for Filtering Nonlinear Systems," in *Proceedings of 1995 American Control Conference-ACC'95*, vol. 3, pp. 1628–1632, IEEE, 1995.

[56] S. J. Julier and J. K. Uhlmann, "Reduced Sigma Point Filters for the Propagation of Means and Covariances through Nonlinear Transformations," in *Proceedings of the 2002 American Control Conference (IEEE Cat. No. CH37301)*, vol. 2, pp. 887–892, IEEE, 2002.

[57] S. J. Julier and J. K. Uhlmann, "Unscented Filtering and Nonlinear Estimation," *Proceedings of the IEEE*, vol. 92, no. 3, pp. 401–422, 2004.

[58] N. Adurthi, P. Singla, and T. Singh, "The Conjugate Unscented Transform an Approach to Evaluate Multi-Dimensional Expectation Integrals," in *American Control Conference (ACC), 2012*, pp. 5556–5561, IEEE, 2012.

[59] N. Adurthi and P. Singla, "Conjugate Unscented Transformation-Based Approach for Accurate Conjunction Analysis," *Journal of Guidance, Control, and Dynamics*, vol. 38, no. 9, pp. 1642–1658, 2015.

[60] N. Wiener, "The Homogeneous Chaos," *American Journal of Mathematics*, vol. 60, no. 4, pp. 897–936, 1938.

[61] P. Dutta and R. Bhattacharya, "Nonlinear Estimation with Polynomial Chaos and Higher Order Moment Updates," in *Proceedings of the 2010 American Control Conference*, pp. 3142–3147, IEEE, 2010.

[62] S. Chakravorty, "A Homotopic Galerkin Approach to the Solution of the Fokker-Planck-Kolmogorov Equation," in *2006 American Control Conference*, pp. 1613–1618, IEEE, 2006.

[63] B. A. Jones, A. Doostan, and G. H. Born, "Nonlinear Propagation of Orbit Uncertainty using Non-intrusive Polynomial Chaos," *Journal of Guidance, Control, and Dynamics*, vol. 36, no. 2, pp. 430–444, 2013.

[64] B. A. Jones, N. Parrish, and A. Doostan, "Postmaneuver Collision Probability Estimation using Sparse Polynomial Chaos Expansions," *Journal of Guidance, Control, and Dynamics*, vol. 38, no. 8, pp. 1425–1437, 2015.

[65] R. O. Duda, P. E. Hart, and D. G. Stork, *Pattern Classification*. John Wiley & Sons, 2012.

[66] D. Raihan and S. Chakravorty, "Particle Gaussian Mixture (PGM) Filters," in *2016 19th International Conference on Information Fusion (FUSION)*, pp. 1369–1376, IEEE, 2016.

[67] J. A. Suykens and J. Vandewalle, "Least Squares Support Vector Machine Classifiers," *Neural processing letters*, vol. 9, no. 3, pp. 293–300, 1999.

[68] C. Lin and S. Wang, "Fuzzy Support Vector Machines," *IEEE transactions on neural networks*, vol. 13, no. 2, pp. 464–471, 2002.

[69] B. Scholkopf and A. J. Smola, *Learning with Kernels: Support Vector Machines, Regularization, Optimization, and Beyond*. MIT press, 2001.

[70] G. Terejanu, P. Singla, T. Singh, and P. D. Scott, "Uncertainty Propagation for Nonlinear Dynamic Systems Using Gaussian Mixture Models," *Journal of Guidance, Control, and Dynamics*, vol. 31, no. 6, pp. 1623–1633, 2008.

[71] K. J. DeMars, R. H. Bishop, and M. K. Jah, "Entropy-Based Approach for Uncertainty Propagation of Nonlinear Dynamical Systems," *Journal of Guidance, Control, and Dynamics*, vol. 36, no. 4, pp. 1047–1057, 2013.

[72] K. J. DeMars, Y. Cheng, and M. K. Jah, "Collision Probability with Gaussian Mixture Orbit Uncertainty," *Journal of Guidance, Control, and Dynamics*, vol. 37, no. 3, pp. 979–985, 2014.

[73] V. Vittaldev and R. P. Russell, "Space Object Collision Probability using Multidirectional Gaussian Mixture Models," *Journal of Guidance, Control, and Dynamics*, pp. 2163–2169, 2016.

[74] J. T. Horwood, N. Singh, J. M. Aristoff, and A. Bhopale, "KRATOS: Kollision Risk Assessment Tool in Orbital Element Spaces," in *Proceedings of the 2016 Advanced Maui Optical and Space Surveillance Technologies Conference (Wailea, HI)*, September 2016.

[75] Y.-z. Luo and Z. Yang, "A Review of Uncertainty Propagation in Orbital Mechanics," *Progress in Aerospace Sciences*, vol. 89, pp. 23–39, 2017.

[76] J. Foster and H. S. Estes, "A Parametric Analysis of Orbital Debris Collision Probability and Maneuver Rate for Space Vehicles," tech. rep., JSC-25898, NASA, 1992.

[77] F. R. Hoots, L. L. Crawford, and R. L. Roehrich, "An Analytic Method to Determine Future Close Approaches between Satellites," *Celestial Mechanics*, vol. 33, no. 2, pp. 143–158, 1984.

[78] S. Alfano, "Determining Satellite Close Approaches, Part 2," *Journal of the Astronautical Sciences*, vol. 42, pp. 143–152, 1994.

[79] J. R. Alarcón-Rodríguez, F. M. Martínez-Fadrique, and H. Klinkrad, "Development of a Collision Risk Assessment Tool," *Advances in Space Research*, vol. 34, no. 5, pp. 1120–1124, 2004.

[80] R. Carlson and J. Lee, "Detecting Near Collisions for Satellites," *IEEE Transactions on Aerospace and Electronic Systems*, vol. 33, no. 3, pp. 921–929, 1997.

[81] E. Denenberg and P. Gurfil, "Improvements to Time of Closest Approach Calculation," *Journal of Guidance, Control, and Dynamics*, vol. 39, no. 9, pp. 1967–1979, 2016.

[82] G. F. Gronchi, "An Algebraic Method to Compute the Critical Points of the Distance Function Between Two Keplerian Orbits," *Celestial Mechanics and Dynamical Astronomy*, vol. 93, no. 1-4, pp. 295–329, 2005.

[83] M. X. J. Raj and M. Mutyalarao, "Analytical Methods for Prefiltering of Close Approaches Between Space Objects," *International Journal of Engineering, Science and Technology*, vol. 5, no. 3, pp. 36–44, 2013.

[84] M. R. Akella and K. T. Alfriend, "Probability of Collision Between Space Objects," *Journal of Guidance, Control, and Dynamics*, vol. 23, no. 5, pp. 769–772, 2000.

[85] R. P. Patera, "General Method for Calculating Satellite Collision Probability," *Journal of Guidance, Control, and Dynamics*, vol. 24, no. 4, pp. 716–722, 2001.

[86] S. Alfano, "A Numerical Implementation of Spherical Object Collision Probability," *Journal of Astronautical Sciences*, vol. 53, no. 1, pp. 103–109, 2005.

[87] S. Alfano, "Review of Conjunction Probability Methods for Short-Term Encounters," *AAS paper*, no. 07-148, 2007.

[88] F. K. Chan, *Spacecraft Collision Probability*. Aerospace Press El Segundo, CA, 2008.

[89] S. Alfano, "Satellite Conjunction Monte Carlo Analysis," *AAS Spaceflight Mechanics Mtg, Pittsburgh, PA., Paper*, pp. 09–233, 2009.

[90] V. Coppola *et al.*, "Evaluating the Short Encounter Assumption of the Probability of Collision Formula," in *Proceedings of the 22nd AAS/AIAA Space Flight Mechanics Meeting*, vol. 143 of *Advances in the Astronautical Sciences*, (San Diego, CA), pp. 2179–2190, Univelt, 2012.

[91] R. P. Patera, "Satellite Collision Probability for Nonlinear Relative Motion," *Journal of Guidance, Control, and Dynamics*, vol. 26, no. 5, pp. 728–733, 2003.

[92] S. Alfano, "Addressing Nonlinear Relative Motion for Spacecraft Collision Probability," in *AIAA/AAS Astrodynamics Specialist Conference and Exhibit*, p. 6760, 2006.

[93] S. Alfano, "Eliminating Assumptions Regarding Satellite Conjunction Analysis," *The Journal of the Astronautical Sciences*, vol. 59, no. 4, pp. 676–705, 2012.

[94] R. P. Patera, "Calculating Collision Probability for Arbitrary Space Vehicle Shapes via Numerical Quadrature," *Journal of guidance, control, and dynamics*, vol. 28, no. 6, pp. 1326–1328, 2005.

[95] K. Chan, "Non-Gaussian Collision Probability," in *Paper AAS 13-908 In AAS/AIAA Astrodynamics Specialist Converence, Aug. 11 -15 , Hilton Head, South carolina*, p. 20, 2013.

[96] V. Coppola *et al.*, "Including Velocity Uncertainty in the Probability of Collision between Space Objects," *American Astronautical Society*, vol. 247, 2012.

[97] M. D. Hejduk and L. C. Johnson, "Approaches to Evaluating Probability of Collision Uncertainty," *AAS Conference 2016*, 2016.

[98] C. T. Shelton and J. L. Junkins, "Probability of Collision Between Space Objects Including Model Uncertainty," *Acta Astronautica*, vol. 155, pp. 462–471, 2019.

[99] C. Sabol, C. Binz, A. Segerman, K. Roe, and P. W. Schumacher Jr, "Probability of Collision with Special Perturbations Dynamics using the Monte Carlo Method," in *AAS/AIAA Astrodynamics Specialist Conference, Girdwood, AK*, 2011.

[100] V. Vittaldev and R. P. Russell, "Space Object Collision Probability via Monte Carlo on the Graphics Processing Unit," *The Journal of the Astronautical Sciences*, vol. 64, no. 3, pp. 285–309, 2017.

[101] L. Baars, D. Hall, and S. Casali, "Assessing GEO and LEO Repeating Conjunctions Using High Fidelity Brute Force Monte Carlo Simulations," in *2019 AAS/AIAA Astrodynamics Specialist Conference*, p. 15, 2019.

[102] M. Losacco, M. Romano, P. Di Lizia, C. Colombo, R. Armellin, A. Morselli, and J. S. Pérez, "Advanced Monte Carlo Sampling Techniques for Orbital Conjunctions Analysis and Near Earth Objects Impact Probability Computation," in *1st NEO and Debris Detection Conference, ESA/ESOC*, pp. 1–12, 2019.

[103] C. T. Shelton and J. L. Junkins, "Conjunction Analysis and Probability of Collision Using Relative Orbital Elements AAS18-446," in *Proceedings of the 2018 AAS Astrodynamics Specialist Conference*, vol. 167 of *Advances in Astronautical Sciences*, (Snowbird, UT), pp. 2387 – 2402, Univelt Inc., 2018.

[104] H. Chernoff *et al.*, "A Measure of Asymptotic Efficiency for Tests of a Hypothesis Based on the Sum of Observations," *The Annals of Mathematical Statistics*, vol. 23, no. 4, pp. 493–507, 1952.

[105] W. Hoeffding, "Probability Inequalities for Sums of Bounded Random Variables," in *The Collected Works of Wassily Hoeffding*, pp. 409–426, Springer, 1994.

[106] P. Dagum, R. Karp, M. Luby, and S. Ross, "An Optimal Algorithm for Monte Carlo Estimation," *SIAM Journal on computing*, vol. 29, no. 5, pp. 1484–1496, 2000.

[107] W. de Vries and D. Phillion, "Monte Carlo Method for Collision Probability Calculations using 3D Satellite Models," tech. rep., 454474 Lawrence Livermore National Lab.(LLNL), Livermore, CA (United States), 2010.

[108] N. Arora, R. P. Russell, and V. Vittaldev, "Parallel Computation of Multiple Space Trajectories using GPUs and Interpolated Gravity Models," *Adv. Astronaut. Sci*, vol. 150, pp. 2881–2897, 2014.

[109] X. Bai, "Modified Chebyshev-Picard Iteration Methods for Solution of Initial Value and Boundary Value Problems," *PhD. Dissertation, Texas A&M University, College Station, Texas, USA*, 2010.

[110] X. Bai and J. Junkins, "Modified Chebyshev-Picard Iteration Methods for Solution of Initial Value Problems," *Advances in the Astronautical Sciences*, vol. 139, pp. 345–362, 2011.

[111] X. Bai and J. Junkins, "Modified Chebyshev-Picard Iteration Methods for Solution of Boundary Value Problems," *Advances in the Astronautical Sciences*, vol. 140, pp. 381–400, 2011.

[112] B. Macomber, A. Probe, R. Woollands, and J. L. Junkins, "Parallel Modified-Chebyshev Picard Iteration for Orbit Catalog Propagation and Monte Carlo Analysis," in *38th Annual AAS/AIAA Guidance and Control Conference, Breckenridge, CO. Jan*, 2015.

[113] B. Macomber, "Enhancements of Chebyshev-Picard Iteration Efficiency for Generally Perturbed Orbits and Constrained Dynamical Systems," *PhD. Dissertation, Texas A&M University, College Station, Texas, USA*, 2015.

[114] J. Read, A. B. Younes, and J. Junkins, "Efficient Orbit Propagation of Orbital Elements using Modified Chebyshev Picard Iteration Method," *Computer Modeling and Engineering Sciences*, vol. 111, no. 1, pp. 65 – 81, 2016.

[115] G. Szego, *Orthogonal Polynomials*, vol. 23 of *Colloquium Publications*. American Mathematical Soc., 1939.

[116] J. C. Mason and D. C. Handscomb, *Chebyshev Polynomials*. CRC Press, 2002.

[117] V. Berinde and F. Takens, *Iterative Approximation of Fixed Points*, vol. 1912. Springer, 2007.

[118] T. Swenson, R. Woollands, J. Junkins, and M. Lo, "Application of Modified Chebyshev Picard Iteration to Differential Correction for Improved Robustness and Computation Time," *The Journal of the Astronautical Sciences*, vol. 64, no. 3, pp. 267–284, 2017.

[119] M. R. Jerrum, L. G. Valiant, and V. V. Vazirani, "Random Generation of Combinatorial Structures from a Uniform Distribution," *Theoretical Computer Science*, vol. 43, pp. 169–188, 1986.

[120] R. M. Karp and M. Luby, "Monte-Carlo Algorithms for the Planar Multiterminal Network Reliability Problem," *Journal of Complexity*, vol. 1, no. 1, pp. 45–64, 1985.

[121] R. M. Karp, M. Luby, and N. Madras, "Monte-Carlo Approximation Algorithms for Enumeration Problems," *Journal of algorithms*, vol. 10, no. 3, pp. 429–448, 1989.

[122] K. T. Alfriend, M. R. Akella, J. Frisbee, J. L. Foster, D.-J. Lee, and M. Wilkins, "Probability of Collision Error Analysis," *Space Debris*, vol. 1, no. 1, pp. 21–35, 1999.

[123] A. B. Probe, C. T. Shelton, T. A. Elgohary, and J. L. Junkins, "Orbital Probability of Collision using Orthogonal Polynomial Approximations IAA-ICSSA-17-06-34," in *Proceedings of the 1st IAA Conference on Space Situational Awareness (ICSSA)*, (Miami, FL), 2017.

[124] D.-J. Lee and K. T. Alfriend, "Effect of Atmospheric Density Uncertainty on Collision Probability," *Spaceflight mechanics 2000*, pp. 1255–1273, 2000.

[125] C. T. Shelton, J. L. Junkins, and M. Majji, "Optical Space Based Observers for Space Situational Awareness," tech. rep., Texas A&M University, January 2020.

[126] M. Walker, B. Ireland, and J. Owens, "A Set Modified Equinoctial Orbit Elements," *Celestial Mechanics and Dynamical Astronomy*, vol. 36, no. 4, pp. 409–419, 1985.

[127] C. Shelton and R. Weisman, "Analysis of Astrodynamic State Variable Formulations," in *Proceedings of the 38th Annual AAS Rocky Mountain Section Guidance and Control Conference*, (Breckenridge, CO), 2015.

[128] J. T. Horwood, J. M. Aristoff, N. Singh, A. B. Poore, and M. D. Hejduk, "Beyond Covariance Realism: A New Metric for Uncertainty Realism," in *SPIE Proceedings: Signal and Data Processing of Small Targets*, vol. 9092, 2014.

[129] J. T. Horwood, J. M. Aristoff, N. Singh, and A. B. Poore, "A Comparative Study of New Non-linear Uncertainty Propagation Methods for Space Surveillance," in *SPIE Proceedings: Signal and Data Processing of Small Targets*, vol. 9092, 2014.

[130] J. M. Aristoff, J. T. Horwood, N. Singh, and A. B. Poore, "Nonlinear Uncertainty Propagation in Orbital Elements and Transformation to Cartesian Space without Loss of Realism," in *AIAA/AAS Astrodynamics Specialist Conference*, 2014. Paper AIAA-2014-4167.

[131] D. P. Bertsekas and J. N. Tsitsiklis, *Introduction to Probability*, vol. 1. Athena Scientific Belmont, MA, 2002.

[132] J. W. Gibbs, "On the Fundamental Formula of Statistical Mechanics, with Applications to Astronomy and Thermodynamicss," *Proceedings of the American Association for the Advancement of Science*, vol. 33, pp. 57–58, 1884.

[133] V. I. Lebedev and D. Laikov, "A Quadrature Formula for the Sphere of the 131st Algebraic Order of Accuracy," in *Doklady Mathematics*, vol. 59-3, pp. 477–481, Pleiades Publishing, Ltd., 1999.

[134] D. Vallado, *Fundamentals of Astrodynamics and Applications*. Space Technology Library, 4th ed., 2013.

[135] A. B. Poore, J. M. Aristoff, and J. T. Horwood, "Covariance and Uncertainty Realism in Space Surveillance," Tech. Rep. 0704-0188, Astrodynamics Innovation Committee, 2015.

[136] B. A. Jones, A. Doostan, and G. H. Born, "Nonlinear Propagation of Orbit Uncertainty Using Non-Intrusive Polynomial Chaos," *Journal of Guidance, Control, and Dynamics*, vol. 36, no. 2, pp. 430–444, 2013.

[137] D. Vallado, *Fundamentals of Astrodynamics and Applications*, pp. 130–140. Space Technology Library, 4th ed., 2013.

[138] H. Schaub, "Relative Orbit Geometry Through Classical Orbit Element Differences," *Journal of Guidance, Control, and Dynamics*, vol. 27, no. 5, pp. 839–848, 2004.

[139] S. D'Amico and O. Montenbruck, "Proximity Operations of Formation-Flying Spacecraft Using an Eccentricity/Inclination Vector Separation," *Journal of Guidance, Control, and Dynamics*, vol. 29, no. 3, pp. 554–563, 2006.

[140] A. W. Koenig, T. Guffanti, and S. D'Amico, "New State Transition Matrices for Spacecraft Relative Motion in Perturbed Orbits," *Journal of Guidance, Control, and Dynamics*, vol. 40, no. 7, pp. 1749–1768, 2017.

[141] D. Brouwer, "The Motion of a Particle with Negligible Mass under the Gravitational Attraction of a Spheroid," *The Astronomical Journal*, vol. 51, p. 223, 1946.

[142] D. Brouwer, "Solution of the Problem of Artificial Satellite Theory without Drag," *The Astronomical Journal*, vol. 64, p. 378, 1959.

[143] R. Greenberg, "Apsidal Precession of Orbits about an Oblate Planet," *The Astronomical Journal*, vol. 86, pp. 912–914, 1981.

[144] P. C. Mahalanobis, "On the Generalised Distance in Statistics," in *Proceedings of the National Institute of Science of India*, vol. 12, pp. 49–55, 1936.

[145] K. T. Alfriend, M. R. Akella, J. Frisbee, J. L. Foster, D.-J. Lee, and M. Wilkins, "Probability of Collision Error Analysis," *Space Debris*, vol. 1, no. 1, pp. 21–35, 1999.

[146] J. Liouville, "Note Sur la Théorie de la Variation des Constantes Arbitraires," *Journal de mathématiques pures et appliquées*, pp. 342–349, 1838.

[147] J. M. Hedo, M. Ruíz, and J. Peláez, "On the Minimum Orbital Intersection Distance Computation: A New Effective Method," *Monthly Notices of the Royal Astronomical Society*, vol. 479, no. 3, pp. 3288–3299, 2018.

[148] P. A. M. Dirac, *The Principles of Quantum Mechanics*. No. 27 in The International Series on Monographs on Physics, Oxford university press, 1981.

[149] J. Crassidis and J. L. Junkins, *Optimal Estimation of Dynamic Systems*. Boca Raton, FL: Chapman & Hall/CRC, 2004.

MCPI OPERATORS AND PROPERTIES OF CHEBYSHEV POLYNOMIALS

A.1 Basic Properties of Chebyshev Polynomials

This section will briefly cover the properties of Chebyshev polynomials that are relevant in the derivation of MCPI. A more complete discussion can be found in [115, 116].

1. Domain: Chebyshev Polynomials $T(x)$ are defined on the domain $x \in [-1, 1]$

2. Recursive: $T_0(x) = 1$, $T_1(x) = x$, and $T_{n+1}(x) = 2xT_n(x) - T_{n-1}$

$$T_0(x) = 1$$

$$T_1(x) = x$$

$$T_2(x) = 2x^2 - 1$$

$$T_3(x) = 4x^3 - 3x$$

$$T_4(x) = 8x^4 - 8x^2 + 1$$

$$T_5(x) = 16x^5 - 20x^3 + 5x$$

3. Trigonometric Definition: $T_n(x) = \cos(n \arccos x) = \cosh(n \operatorname{arcosh} x)$, $n = 0, 1, 2, \ldots, N$

4. Orthogonal:

$$\int_{-1}^{1} T_n(x)T_m(x) \frac{dx}{\sqrt{1-x^2}} = \begin{cases} 0 & : n \neq m \\ \pi & : n = m = 0 \\ \pi/2 & : n = m \neq 0 \end{cases}$$

5. Discrete Orthogonality:

$$\sum_{k=0}^{M-1} T_i(x_k)T_j(x_k)\frac{1}{\sqrt{1-x_k}} = \begin{cases} 0 & : i \neq j \\[2mm] M & : i = j = 0 \\[2mm] M/2 & : i = j \neq 0 \end{cases}$$

where $x_k = \cos\left(\pi\frac{2k+1}{2M}\right)$, $k = 0, 1, 2, \ldots, M$

6. Recursive Integration Relation:

$$\int T_n \, dx = \frac{1}{2}\left(\frac{T_{n+1}}{n+1} - \frac{T_{n-1}}{n-1}\right)$$

A.2 MCPI Integration Matrix

The integration matrix is the linear operation that relates the coefficients of the Chebyshev series of the integrand to the coefficients of the integrated series. That is

$$\boldsymbol{\beta} = [S]\boldsymbol{\alpha} \tag{A.1}$$

where

$$\sum_{i=0}^{N} \beta_i T_i(\tau) = \boldsymbol{x}_0 + \int_{-1}^{\tau} \sum_{i=0}^{N} \alpha_i T_i(t) \, dt \tag{A.2}$$

. $[S]$ arises as a result of the recursive integration relation of Chebyshev polynomials and is given as

$$[S] = \begin{bmatrix} 0 & \frac{1}{4} & 0 & \cdots & \cdots & \cdots & 0 \\ 1 & 0 & -\frac{1}{2} & 0 & \cdots & \cdots & 0 \\ 0 & \frac{1}{4} & 0 & -\frac{1}{4} & 0 & \cdots & 0 \\ \vdots & 0 & \frac{1}{2k} & 0 & -\frac{1}{2k} & \cdots & 0 \\ \vdots & \vdots & 0 & \ddots & \ddots & \ddots & 0 \\ \vdots & \vdots & \vdots & \ddots & \frac{1}{2(N-1)} & 0 & -\frac{1}{2(N-1)} \\ \vdots & \vdots & \vdots & \vdots & 0 & \frac{1}{2N} & 0 \\ 0 & \cdots & \cdots & \cdots & \cdots & 0 & \frac{1}{2(N+1)} \end{bmatrix} \tag{A.3}$$

$k = 3, 4, 5, \ldots, N + 1$. Where $[S] \in \mathbb{R}^{N+1 \times N}$ is a non square matrix. This is because whenever a polynomial of degree N is integrated you get back a polynomial of degree $N + 1$. However, one can neglect the last row of $[S]$ if N is chosen large enough. That is, if the series $\epsilon_k = \|\boldsymbol{x}(\tau) - \sum_{i=0}^{k} \beta_i T_i(\tau)\|$ converges to an acceptable degree within the first N terms, the inclusion of additional terms is not necessary.

APPENDIX B

PROPERTIES OF NORMAL DISTRIBUTIONS

B.1 Normal Distribution as a Conditional PDF

Let us consider a normally distributed random variable $\boldsymbol{q} \in \mathbb{R}^m$ supposes $\boldsymbol{q}^T = [\boldsymbol{r}^T, \boldsymbol{v}^T]$ where $\boldsymbol{r} \in \mathbb{R}^n,\ \ n < m$ and $\boldsymbol{v} \in \mathbb{R}^w,\ \ w = m - n$. The covariance matrix of $\boldsymbol{q}$ is written as

$$Q = \begin{bmatrix} A & B^T \\ B & C \end{bmatrix} \tag{B.1}$$

We would now like to show

$$\mathcal{N}(\boldsymbol{q}, \bar{\boldsymbol{q}}, Q) = \mathcal{N}(\boldsymbol{r}, \bar{\boldsymbol{r}}, A)\mathcal{N}(\boldsymbol{v} - P\boldsymbol{r}, \bar{\boldsymbol{v}} - P\bar{\boldsymbol{r}}, C') \tag{B.2}$$

where $P = BA^{-1}$ and $C' = C - BA^{-1}B^T$. To do this let us introduce a linear mapping

$$T = \begin{bmatrix} I_{n \times n} & 0_{n \times w} \\ P_{w \times n} & I_{w \times w} \end{bmatrix} \tag{B.3}$$

Note that in terms of the linear transformation T we have the following relationship

$$\boldsymbol{q} = T^{-1}\boldsymbol{q}' \tag{B.4}$$

where $\boldsymbol{q}'^T = [\boldsymbol{r}^T, \boldsymbol{v}'^T]$ and $T^{-1} = \begin{bmatrix} I_{n \times n} & 0_{n \times w} \\ -P_{w \times n} & I_{w \times w} \end{bmatrix}$ and $\det(T) = 1$.

Substituting the relationship in equation (B.4) into the normal distribution we obtain.

$$\mathcal{N}(\boldsymbol{q}, \bar{\boldsymbol{q}}, Q) = \frac{1}{\sqrt{\det(2\pi TQT^T)}} \exp -\frac{1}{2}[T(\boldsymbol{q} - \bar{\boldsymbol{q}})]^T T^{-T} Q^{-1} T^{-1} [T(\boldsymbol{q} - \bar{\boldsymbol{q}})] \tag{B.5}$$

By direct computation we see that the above equation reduces to the desired expression

$$\mathcal{N}(\boldsymbol{q}, \bar{\boldsymbol{q}}, Q) = \mathcal{N}(\boldsymbol{r}, \bar{\boldsymbol{r}}, A)\mathcal{N}(\boldsymbol{v} - P\boldsymbol{r}, \bar{\boldsymbol{v}} - P\bar{\boldsymbol{r}}, C') \tag{B.6}$$

B.2   Product of Two Normal Distributions

In this section we will show that the product of two normal distributions returns again a normal distribution. Let us consider the product of the distributions for two random vectors x_a and $x_b = x_a + x_r$.

$$p = \mathcal{N}(\boldsymbol{x}_a, \bar{\boldsymbol{x}}_a, Q_a)\mathcal{N}(\boldsymbol{x}_a + \boldsymbol{x}_r, \bar{\boldsymbol{x}}_b, Q_b) \tag{B.7}$$

Now let us make the following substitutions $\boldsymbol{\lambda} = \boldsymbol{x}_r - \boldsymbol{\mu}$, $\boldsymbol{\mu} = \bar{\boldsymbol{x}}_b - \bar{\boldsymbol{x}}_a$ and $\boldsymbol{\eta} = \boldsymbol{x}_a - \bar{\boldsymbol{x}}_a$. With respect to these variables the original expression becomes

$$p = \mathcal{N}(\boldsymbol{\eta}, 0, Q_a)\mathcal{N}(\boldsymbol{\eta} + \boldsymbol{\lambda}, 0, Q_b) \tag{B.8}$$

Looking at just the exponent from the above product we see

$$
\begin{aligned}
&\exp -\frac{1}{2}\left[\boldsymbol{\eta}^T Q_a^{-1}\boldsymbol{\eta} + (\boldsymbol{\eta} + \boldsymbol{\lambda})^T Q_b^{-1}(\boldsymbol{\eta} + \boldsymbol{\lambda})\right] \\
&= \exp -\frac{1}{2}\left[\boldsymbol{\eta}^T (Q_a^{-1} + Q_b^{-1})\boldsymbol{\eta} + (\boldsymbol{\lambda})^T Q_b^{-1}(\boldsymbol{\lambda}) + 2\boldsymbol{\eta}^T Q_b^{-1}\boldsymbol{\lambda}\right]
\end{aligned}
\tag{B.9}
$$

Let $P^{-1} = Q_a^{-1} + Q_b^{-1}$ then the above expression can be rewritten as

$$\exp -\frac{1}{2}\left[(\boldsymbol{\eta} + S\boldsymbol{\lambda})^T P^{-1}(\boldsymbol{\eta} + S\boldsymbol{\lambda}) + \boldsymbol{\lambda}^T Q_b^{-1}(I - S)\boldsymbol{\lambda}\right] \tag{B.10}$$

where $S = PQ_b^{-1}$. Note that the second term in the exponent expands to $Q_b^{-1} - Q_b^{-1}PQ_b^{-1}$. There are several references on how to invert this expressions such as [149]. These show that in general

$$(A + BCD)^{-1} = A^{-1}B(DA^{-1}B + C^{-1})^{-1}DA^{-1} \tag{B.11}$$

Applying this to our expressions yields the following.

$$(Q_b^{-1} - Q_b^{-1}PQ_b^{-1})^{-1} = Q_q + (P^{-1} - Q_b^{-1})^{-1} = Q_b + Q_a \tag{B.12}$$

Letting $R = Q_a + Q_b$ and substituting back into the exponential term we obtain

$$\exp{-\frac{1}{2}\left[(\boldsymbol{\eta} + S\boldsymbol{\lambda})^T P^{-1}(\boldsymbol{\eta} + S\boldsymbol{\lambda}) + \boldsymbol{\lambda}^T R^{-1}\boldsymbol{\lambda}\right]} \tag{B.13}$$

Therefore,

$$p = \mathcal{N}(\boldsymbol{\eta} + S\boldsymbol{\lambda}, 0, P)\mathcal{N}(\boldsymbol{\lambda}, 0, R)$$
$$= \mathcal{N}(\boldsymbol{x}_a + Sx_r, \bar{\boldsymbol{x}}_a + S\boldsymbol{\mu}, P)\mathcal{N}(\boldsymbol{x}_r, \boldsymbol{\mu}, R) \tag{B.14}$$

APPENDIX C

ORBITAL ELEMENT TRANSFORMATIONS

C.1 MEq Orbital Elements to Relative Orbital Elements

The rotation sequence from the inertial frame to the Modified Equinoctial PQW frame is again a 3-1-3 rotation, this time through the angles $\Omega, i_r, -\Omega$ where Ω is the right ascension of the ascending node.

Battin [39] gives the inverse rotation from the MEq frame to an inertial reference frame in terms of the MEq orbital elements.

$$R = \frac{1}{1+h^2+k^2} \begin{Bmatrix} 1+h^2-k^2 & 2hk & 2k \\ 2hk & 1-h^2+k^2 & -2h \\ -2k & 2h & 1-h^2-k^2 \end{Bmatrix} \tag{C.1}$$

The composite rotation from the S_2 perifocal frame to the S_1 perifocal frame is then

$$R_r = R_1^T R_2 \tag{C.2}$$

If R_r is a 3-1-3 rotation itself from the S_2 to the S_1 frame through the angles $\Omega_{rel}, i_r, -\Omega_{ref}$ then again we have

$$\cos i_r = R_{r_{3,3}}$$
$$\tan \Omega_{ref} = \frac{-R_{r_{1,3}}}{R_{r_{2,3}}} \tag{C.3}$$
$$\tan \Omega_{rel} = \frac{R_{r_{3,1}}}{-R_{r_{3,2}}}$$

In this case Ω_{rel} is the angle between the $\hat{x}$ axis of the MEq perifocal frame and the line of relative nodes, i_r is the relative inclination between the two orbital planes, and Ω_{ref} is the angle between

the line of relative nodes and the $\hat{x}$ axis of the reference orbit.

C.2   MEq Orbital Elements to Spherical Coordinates

If the x-y-z axis of the spherical reference frame are chosen such that they are aligned with the x-y-z axis of the MEq perifocal frame, then the the spherical coordinates of an object with respect to the reference frame are

$$
r = \frac{p}{w}
$$

$$
\theta = \arctan\left(\frac{R_{21}\cos L + R_{22}\sin L}{R_{11}\cos L + R_{12}\sin L}\right)
$$

$$
\phi = \arccos\left(R_{31}\cos L + R_{32}\sin L\right)
$$

$$
\dot{r} = \frac{H}{p}(f\sin L - g\cos L)
$$

$$
\dot{\theta} = \frac{h}{r^2}\frac{R_{33}}{\sin\phi^2}
$$

$$
\dot{\phi} = \frac{h}{r^2}(R_{23}\cos L - R_{13}\sin L)
$$

(C.4)

where $w = 1 + f\cos L + g\sin L$.

APPENDIX D

THE CRATER ALGORITHM

D.1 Assumptions

These assumptions were used for the current implementation of the CRATER algorithm

- A1. Trajectories only enter the hardball radius once

- A2. Trajectories do not satisfy $r(t) = R_c$ (where $r(t)$ is the relative distance between the satellites) for a finite amount of time, such that each trajectory belongs to a unique Λ_t.

- A3. The dynamics and PDF of each object are independent

- A4. The PDF at time T can be modeled as a Gaussian Mixture or is locally Gaussian

- A5. Motion is deterministic or subject to parametric force model uncertainty

- A6. Initial state uncertainty is available in terms of orbital elements

- A7. The state PDF can be well approximated as a single Gaussian in orbital element space